Dark Energy and the Inhomogeneous Universe

Philip Bull

Wadham College

University of Oxford

A thesis submitted for the degree of

Doctor of Philosophy

To Mum and Dad

Doubt wisely; in strange way
To stand inquiring right, is not to stray;
To sleep, or run wrong, is.

— John Donne, *Satire III*

Acknowledgements

A number of people have greatly influenced my research, ideas, and general approach to physics, and I would like to acknowledge their support. In particular, I would like to thank my supervisors, Pedro Ferreira and Tim Clifton, for their sage advice and keen eye for interesting problems. I am also grateful to my collaborators – Chris Clarkson, Hans Kristian Eriksen, Marc Kamionkowski, and Ingunn Wehus – for sharing their expertise and insight, and for their kind hospitality. Special thanks are due to Joe Zuntz, for his expert assistance in computational matters, and to Alan Coley, for sharing his hospitality and rigorous outlook on the field. I am also grateful to the STFC, Oxford Physics, and Wadham College for financial support.

I would like to thank the following people for numerous enlightening discussions during the course of my research: Graeme Addison, Tessa Baker, John Barrow, Richard Battye, Krzystof Bolejko, Rich Booth, Roger Blandford, Thomas Buchert, Clive Dickinson, Jo Dunkley, Ruth Durrer, Sean February, Renée Hložek, Shaun Hotchkiss, Arthur Kosowsky, Thibaut Louis, Roy Maartens, Edward Macaulay, John Magorrian, Valerio Marra, Doddy Marsh, Niko Meures, Sesh Nadathur, Sigurd Næss, Jim Peebles, Andrew Pontzen, Will Potter, Syksy Räsänen, Subir Sarkar, Dominik Schwarz, Dag Sverre Seljebotn, Joe Silk, Obinna Umeh, Jean-Philippe Uzan, Wessel Valkenburg, and Jim Zibin. I am also grateful to Tessa Baker, Tim Clifton, Ruth Durrer, Pedro Ferreira, Johannes Noller, and Subir Sarkar for their corrections and comments on this manuscript.

Finally, I would like to thank my family and friends in Stoke, Manchester, Oxford, London and elsewhere, for all of their love and support. I don't know where I'd be without them!

Abstract

Dark Energy and the Inhomogeneous Universe

Philip Bull

Wadham College, University of Oxford

Submitted for the degree of Doctor of Philosophy

Hilary Term, 2013

In this thesis, I study the relativistic effects of matter inhomogeneities on the accelerating expansion of the Universe. The acceleration is often taken to be caused by the presence of an exotic fluid called Dark Energy, or else a non-zero ‘cosmological constant’ term in the field equations of General Relativity. I consider whether this result could instead be an artefact caused by using an incorrect model to interpret observations. The standard ‘concordance’ cosmological model assumes the Cosmological Principle, which states that the matter distribution on large scales is homogeneous. One possibility is that correction terms appear in the field equations when small-scale inhomogeneities are smoothed over to produce this homogeneous model. These ‘backreaction’ effects could affect the dynamics of the spacetime, causing an apparent acceleration. I clarify the relationship between acceleration of the averaged spacetime and acceleration inferred from observable quantities, and show that they are closely related in statistically-homogeneous spacetimes.

Another possibility is that the Universe could be inhomogeneous on large scales. If there was a large ‘void’, with us at the centre, the lensing of light by the void could reproduce the observations that imply cosmic acceleration. I show that a popular class of void models, based on spherically-symmetric Lemaître-Tolman-Bondi spacetimes, are unable to simultaneously fit a selection of observational data, thus effectively ruling-out this possibility. These data include the Kinematic Sunyaev-Zel’dovich (KSZ) effect, which is a distortion/shift of the Cosmic Microwave Background (CMB) frequency spectrum caused by the Compton scattering of photons by hot gas in galaxy clusters. This, and other distortions of the CMB frequency spectrum, are sensitive to the degree of anisotropy in the CMB about a scattering cluster. I suggest tests involving these observables that exploit the strong link between isotropy and homogeneity to (a) distinguish between different causes of a deviation from spatial flatness on the horizon scale, and (b) potentially confirm the Cosmological Principle using observations. Finally, I describe a novel Bayesian CMB component separation method for extracting the Sunyaev-Zel’dovich signal of clusters from CMB sky maps.

Conventions

The following notation conventions are used in this thesis:

- The spacetime metric signature is $\{-,+,+,+\}$.

- Spacetime indices are given by letters early in the latin alphabet, e.g. a, b, c, d. The indices run from 0 to 3, e.g. $T^a = \{T^0, T^1, T^2, T^3\}$, where 0 is the time coordinate. Spatial indices are given by letters in the middle of the latin alphabet, e.g. i, j, k, and run from 1 to 3. The Einstein summation convention will often be used, where repeated indices are summed over.

- Square brackets denote anti-symmetrisation of the enclosed spacetime indices, e.g. $U_{[a}V_{b]} = \frac{1}{2}(U_a V_b - U_b V_a)$. Round brackets denote symmetrisation.

- The symbol δ will often be taken to mean the fractional deviation of some quantity from its mean, e.g. $\delta_x = (x - \bar{x})/\bar{x}$.

- The speed of light, c, is set to unity in much of what follows. Some expressions explicitly include factors of c to make their dimensionality clear.

Publication Statement

The work in this thesis is based on material presented in the following papers:

1. P. Bull and T. Clifton, *Phys. Rev. D* **85**, 103512 (2012).
2. P. Bull, T. Clifton and P. G. Ferreira, *Phys. Rev. D* **85**, 024002 (2012).
3. T. Clifton, C. Clarkson and P. Bull, *Phys. Rev. Lett.* **109**, 051303 (2012).
4. P. Bull and M. Kamionkowski, *Phys. Rev. D* **87**, 081301(R) (2013).
5. I. K. Wehus, P. Bull, H. K. Eriksen, P. G. Ferreira, U. Fuskeland, K. M. Górski and J. B. Jewell, *in prep.* (2013).

I certify that the work presented here is my own, with the following exceptions/clarifications:

Chapter 1 Some of the material in Sections 1.2 and 1.3 is based on passages of Papers 1 and 2, and a small amount of Section 1.1.4 is based on Paper 3.

Chapter 2 Based on Paper 1. The original draft of the paper was written by me, except for Sections 2.2.2 and 2.3.2, which were written by TC. The results for the Kasner-EdS model were calculated by TC. Final editing of the paper was shared between myself and TC.

Chapter 3 Based on Paper 2. The original draft of the paper was written by me, with editing by TC and PGF.

Chapter 4 Based on Papers 3 and 4. The bulk of this chapter is based on Paper 4, which was originally written by me. MK and myself edited the paper. Section 4.4 is partially based on material from Paper 4, which was primarily written by TC and CC. Edits were made by TC, CC and myself.

Chapter 5 Based on Paper 5. All text in this chapter is my own work. The modifications to the Commander code described in 5.3 were performed by IKW, myself, and HKE.

Contents

Contents vi

1 Introduction **1**

1.1 Concordance model of cosmology 3
  1.1.1 General Relativity 6
  1.1.2 Friedmann-Lemaître-Robertson-Walker spacetime 8
  1.1.3 Perturbations to FLRW 9
  1.1.4 The Cosmological Principle 12
1.2 Inhomogeneous cosmological spacetimes 16
  1.2.1 Relativistic models of inhomogeneity 17
  1.2.2 1+3 decomposition 19
  1.2.3 An example inhomogeneous spacetime: LTB 20
  1.2.4 Backreaction, fitting, and averaging 21
  1.2.5 The Buchert scalar averaging formalism 26
1.3 Light propagation and the Sachs Equations 27
  1.3.1 The Sachs formalism and optical scalars 28
  1.3.2 Observable quantities 29
  1.3.3 The Sachs equations 30
  1.3.4 Light propagation in an FLRW spacetime 31
  1.3.5 Compton scattering and the SZ effect 33
1.4 Statistical methods 37

1.4.1 Likelihood estimation 37
1.4.2 Metropolis-Hastings algorithm 39
1.4.3 Gibbs sampling 43

2 Measures of cosmic acceleration 44

2.1 Measures of acceleration 44
2.1.1 Local volume acceleration 45
2.1.2 Observed acceleration (from Hubble diagram) 46
2.1.3 Acceleration from local observations (using the Kristian-Sachs formalism) 48
2.1.4 Acceleration of the average (Buchert's formalism) 50
2.2 Inhomogeneous cosmological models 51
2.2.1 Spherical collapse model 52
2.2.2 Kasner-EdS model 55
2.2.3 Lemaître-Tolman-Bondi model 59
2.3 Results 62
2.3.1 Spherical collapse 62
2.3.2 Kasner-EdS 67
2.3.3 LTB 70
2.4 Discussion 75

3 The KSZ effect as a test of radial inhomogeneity 79

3.1 Physical properties of LTB spacetimes 82
3.1.1 Inhomogeneous late universe 84
3.1.2 Inhomogeneous big bang 85
3.2 Results with constant bang time 88
3.2.1 Supernovae 89
3.2.2 The CMB and H_0 89
3.2.3 The KSZ Effect 90

3.2.4 Other Observables . . . 93

3.3 Results with varying bang time . . . 94

3.3.1 Supernovae . . . 95

3.3.2 The CMB and H_0 . . . 96

3.3.3 The KSZ Effect . . . 100

3.3.4 Combined Constraints (SN+CMB+H_0+KSZ) . . . 103

3.3.5 More Complicated Profiles . . . 105

3.4 Discussion . . . 108

4 Large-scale inhomogeneity and deviations from flatness 113

4.1 Bias in Ω_K due to a local inhomogeneity . . . 116

4.2 Distortions caused by the inhomogeneity . . . 118

4.2.1 Kinematic SZ signal of galaxy clusters . . . 119

4.2.2 Kinematic SZ angular power spectrum . . . 120

4.2.3 Compton y-distortion . . . 122

4.3 Constraints on deviations from flatness . . . 122

4.4 Testing the Cosmological Principle . . . 124

5 Extracting Sunyaev-Zel'dovich signals from CMB sky maps 128

5.1 Cosmology with the SZ effect . . . 130

5.1.1 Thermal SZ effect . . . 131

5.1.2 Extracting the KSZ effect signal . . . 133

5.1.3 Peculiar velocity statistics . . . 136

5.1.4 Effective KSZ extraction . . . 140

5.2 SZ extraction with a CMB Gibbs sampler . . . 142

5.2.1 The sky model . . . 143

5.2.2 Sampling scheme . . . 145

5.2.3 Adding an SZ component . . . 147

5.3 Applications to simulated data . . . 152

5.4 Generalization to other localized signals 159
    5.4.1 Integrated Sachs-Wolfe effect 159
    5.4.2 Topological defects 160
    5.4.3 Signatures of pre-inflationary physics 161

6 Conclusions 162

6.1 Summary of key findings 162
6.2 Future directions 166

References 169

Chapter 1

Introduction

Before the advent of general relativity (GR), cosmology fell mostly outside the domain of scientific investigation. Although important advances were made in understanding our place in the Universe from the 16th Century onwards – beginning with Copernicus' publication of *De revolutionibus orbium coelestium* [Copernicus, 1543] – there were few serious attempts to study the structure of the Universe from a physical perspective until the early 20th Century [Harrison, 2000; Hetherington & McCray, 2013]. Even the introduction of Newton's theory of gravity, which proved so powerful in explaining the motions of Solar System bodies, failed to stimulate more than just a handful of (mostly speculative) investigations into the large scale structure.

Instead, much of the development in cosmology was philosophical: Copernicus demoted the Earth from its privileged position at the centre of the cosmos, Newton introduced the notion that the world ran like a deterministic 'clockwork' mechanism, and the development of physical science throughout the 18th and 19th Centuries supplanted theological descriptions of the natural world. Our view of our place in the cosmos certainly changed during this period, but nothing that could be recognised as a consensus scientific model of its overall structure was forthcoming.

This would all change with Einstein's introduction of GR in 1915. Suddenly, physicists had a way of constructing mathematically-consistent, global descriptions of space and time. Initial attempts at constructing cosmological models by Einstein [1917], de Sitter [1917], Friedmann [1922], and Lemaître [1931], in concert with key observations by Hubble, Slipher, and others [Hubble, 1929; Raifeartaigh, 2012], put cosmology on a firmly scientific footing. Since then, physical cosmology has gone from strength to strength, leading to such revolutionary discoveries as the expansion of space, the Big Bang and nucleosynthesis, the formation of structure from quantum fluctuations and, most recently, the apparent acceleration of the cosmos.

It is the latter – cosmic acceleration – that forms the focus of the work presented in this thesis. The question of if, and why, the expansion of the Universe is accelerating is one of the foremost problems in fundamental physics today. Observations of distant Type Ia supernovae are well-fit by homogeneous and isotropic Friedmann-Lemaître-Robertson-Walker (FLRW) solutions of general relativity, but only if a substantial fraction of the energy density in the Universe is in the form of a *cosmological constant*, Λ. For this constant to take the value required by observations requires an extraordinary degree of fine-tuning, with the observed Λ being more than 60 orders of magnitude smaller than the value expected from elementary particle physics [Weinberg, 1989]. Many authors have attempted to remedy this situation by proposing modifications to gravity, the existence of negative-pressure components of the cosmological 'fluid', new scalar fields, and a host of other exotic mechanisms. Others have sought to explain it by modifying the basic assumptions of cosmology itself, such as the Cosmological Principle.

In this thesis, my main focus will be on the relationship between matter inhomogeneities and cosmic acceleration. In particular, I will be tackling the following questions:

- Can matter inhomogeneities affect our observations in such a way that they would cause us to erroneously infer cosmic acceleration where there is none?
- Is it possible to observationally confirm the Cosmological Principle, or at least constrain the degree of inhomogeneity on large scales?
- How can we use long-range observations of the inhomogeneous matter distribution (e.g. using galaxy clusters) to infer how the Universe behaves on large scales?

These questions are dealt with in detail in subsequent chapters. For the remainder of this chapter, I will briefly review a number of key results and concepts that will be important for later chapters.

1.1 Concordance model of cosmology

In recent decades, cosmology has acquired a "standard model", of sorts. It is based on a homogeneous and isotropic Friedmann-Lemaître-Robertson-Walker (FLRW) spacetime that had an early hot, dense phase, beginning with an apparently singular state, the "Big Bang". The Universe has subsequently expanded and cooled, and structures such as galaxies have formed. These structures are described by small perturbations of the FLRW metric that were seeded by *inflation*, a process that happened a mere fraction ($\sim 10^{-33}$) of a second after the Big Bang, and which caused a superluminal expansion of space that left it very close to being homogeneous and spatially-flat.

Inflation ended with *reheating*, when the *inflaton field* that was driving the superluminal expansion decayed into a range of high-energy Standard Model particles, heating-up the Universe. Relativistic species such as photons and neutrinos initially dominated the cosmic energy density, and the cosmos was filled with a strongly-coupled photon-baryon fluid. During this period of radiation domination, *nucleosynthesis* occurred, creating elements heavier than Hydrogen. As the

Universe continued to expand, its energy density became dominated by matter, and the temperature dropped sufficiently that the photons and baryons *decoupled* and electrons and ions combined into neutral atoms, leaving space transparent. The last photons to be scattered before decoupling remain as a thermal radiation field that pervades space, with a temperature that has now been redshifted into the microwave part of the spectrum.

The small perturbations left in the cosmological fluid by inflation grew with time, forming the first stars (which *reionised* the newly-neutral Universe), and then larger structures like galaxies, which then clumped together to form clusters, filaments, and voids. The matter which comprises these structures is dominated not by baryons, but by a cold, pressureless 'dark matter' that appears to interact only through gravity. Similarly, the net energy density of the Universe at late times is dominated not by matter, but by a smooth (unclustered) component with negative pressure dubbed 'dark energy'. This appears to be making the expansion of space accelerate, a property that is consistent with the effects of a cosmological constant, Λ, in Einstein's field equations.

This picture is commonly referred to as ΛCDM, or the "concordance model" of cosmology [Ostriker & Steinhardt, 1995]. It is tremendously successful, in that its theoretical predictions appear to match a wide range of observations to a high degree of precision[1], including:

- The distance-redshift relation reconstructed using Type Ia supernova explosions as standard candles [Colgate, 1979; Riess *et al.*, 1998; Perlmutter *et al.*, 1999; Sullivan *et al.*, 2011].
- The angular power spectrum of the Cosmic Microwave Background radiation [Hinshaw *et al.*, 2012].

---

[1] Note, however, that these observations do not necessarily support ΛCDM to the full extent that is sometimes claimed [Peebles, 2002; Sarkar, 2008; Durrer, 2011], and that a number of other observations are claimed to be in tension with the model (e.g. Peebles & Nusser [2010]; Perivolaropoulos [2011]; Kashlinsky *et al.* [2012]; Flender *et al.* [2013]).

- Galaxy number counts, acoustic oscillations in the large-scale matter distribution, and the growth rate of structure from galaxy redshift surveys [Peacock *et al.*, 2001; Parkinson *et al.*, 2012; Dawson *et al.*, 2013].

Unfortunately, the ΛCDM paradigm suffers from serious problems. The dark matter and dark energy components that it requires have been detected only indirectly, through their gravitational effects on 'normal' (baryonic) matter and light, and their nature and origin are unknown. Although dark matter has strong indirect observational support, it has yet to be detected directly [Sellwood & Kosowsky, 2000; Bertone *et al.*, 2005; Fornengo, 2008]. Dark energy in particular suffers from theoretical maladies; if it really is a cosmological constant, its value would appear to be extremely fine-tuned, being at an energy scale radically different from all other known physics [Weinberg, 1989; Carroll, 2001; Bousso, 2008]. It also seems coincidental that we should find ourselves living at a time when the energy densities in matter and dark energy should be comparable, since this will not be the case for most of the Universe's history [Dicke & Peebles, 1979; Arkani-Hamed *et al.*, 2000]. Furthermore, large segments of the theory lack substantial empirical grounding; the use of a FLRW spacetime, for example, has received only limited observational validation, despite sitting at the very foundations of the model [Maartens, 2011]. It is the existence of these problems that have motivated a multitude of wide-ranging theoretical and observational programmes within the cosmological community to refine, understand, or even replace aspects of ΛCDM with something 'better' [Peebles, 2002; Peebles & Ratra, 2003; Albrecht *et al.*, 2006; Durrer & Maartens, 2008; Clifton *et al.*, 2012b].

In the rest of this section, I give a brief overview of some aspects of the mathematical framework underlying ΛCDM that will be useful in later chapters, and discuss some of the key assumptions that occupy the foundations of this model.

1.1.1 General Relativity

General Relativity (GR) is the currently-favoured theory of gravitation. It supplanted Newtonian gravity soon after its introduction by Einstein in 1915, following a highly-publicised measurement of the bending of light by the Sun during a solar eclipse in 1919. Gravity is the dominant force on Solar System scales and above, and so GR is the natural choice of theoretical framework for cosmology. In this section, I will briefly review a handful of mathematical results from GR that are required to understand some later material. Comprehensive introductions to GR may be found in a number of well-known textbooks, including Wald [1984] and Plebański & Krasiński [2006].

In GR, space and time are bundled together into one overarching entity, spacetime. The curvature of the spacetime geometry is related to its energy content, as determined by the Einstein field equations,

$$R_{ab} - \frac{1}{2} g_{ab} R + g_{ab} \Lambda = \frac{8\pi G}{c^4} T_{ab}. \tag{1.1}$$

Here, g_{ab}, R_{ab} and $R = R^a_a$ are geometric quantities called the metric tensor, Ricci tensor, and Ricci scalar, and T_{ab} is the stress-energy tensor. These are functions of spacetime location, x^a, in general. Λ is the cosmological constant, and has no spacetime dependence. The metric tensor in a given coordinate system is often specified by the line element, $ds^2 = g_{ab} dx^a dx^b$.

An important principle in GR is that of *covariance* – that physical laws should remain unchanged regardless of reference frame. All relations in GR can be written in a manifestly covariant form that remains unchanged when transforming to a different reference frame or coordinate system. Normal partial derivatives of the form $\partial / \partial x^a$ are not covariant, and so one defines the covariant derivative,

$$\nabla_b A^a = \frac{\partial A^a}{\partial x^b} + \Gamma^a_{bc} A^c \tag{1.2}$$

$$\nabla_b A_a = \frac{\partial A_a}{\partial x^b} - \Gamma^c_{ab} A_c, \tag{1.3}$$

where Γ^a_{bc} are the Christoffel symbols for the Levi-Civita connection. The covariant derivative is defined such that the metric is parallel-transported onto itself along a given curve, so that $\nabla_a g_{bc} = 0$. The Christoffel symbols may be written in terms of first derivatives of the metric,

$$\Gamma^a_{bc} = \frac{1}{2} g^{ad} \left[\frac{\partial g_{db}}{\partial x^c} + \frac{\partial g_{dc}}{\partial x^b} - \frac{\partial g_{bc}}{\partial x^d} \right]. \tag{1.4}$$

The Riemann curvature tensor, R_{abcd}, encodes full information on the curvature of spacetime, and can be obtained by further differentiating the Christoffel symbols. The Riemann tensor is often decomposed into Ricci and Weyl parts,

$$R_{abcd} = C_{abcd} + R_{a[c} R_{d]b} - \frac{1}{3} R g_{a[c}\, g_{d]b}, \tag{1.5}$$

where C_{abcd} is the Weyl tensor, and $R_{ab} = R^c_{acb}$ is the Ricci tensor.

The stress-energy tensor contains information on energy/matter fields that exist in the spacetime. Stress-energy is locally conserved, $\nabla_b\, T^{ab} = 0$. For cosmological applications, the stress-energy is generally taken to be of perfect fluid form,

$$T^a_b = \mathrm{diag}(-\rho, p, p, p), \tag{1.6}$$

where ρ is the energy density of the fluid, and $p = w\rho$ is its pressure. The equation of state parameter, w, depends on the properties of the fluid; for example, $w = 0$ for pressureless matter (dust), $w = 1/3$ for radiation, and $w = -1$ for a cosmological constant.

In the absence of any external forces, matter and light follow *geodesics* – extremal curves in spacetime, which trace out the ‘shortest path’ between two spacetime points. A geodesic curve $x^a(\lambda)$ satisfies

$$\frac{d^2x^a}{d\lambda^2} + \Gamma^a{}_{bc}\frac{dx^b}{d\lambda}\frac{dx^c}{d\lambda} = 0, \tag{1.7}$$

where λ is an affine parameter along the curve. The tangent to the curve is often written as $dx^a/d\lambda = \dot{x}^a$, where $\dot{x}^a$ may be replaced by u^a or k^a depending on whether the geodesic curve is timelike ($u^a u_a = -1$) or null ($k^a k_a = 0$) respectively. In the timelike case, the affine parameter along the curve is the proper time, $\lambda = \tau$.

1.1.2 Friedmann-Lemaître-Robertson-Walker spacetime

In this section, I briefly review some properties of the Friedmann-Lemaître-Robertson-Walker (FLRW) spacetime on which the standard cosmological model is based. A more comprehensive introduction is given in Plebański & Krasiński [2006].

The FLRW spacetime is the only solution to the field equations with a perfect fluid stress-energy tensor that is globally homogeneous and isotropic. In comoving spherical polar coordinates, its metric is given by the line element

$$ds^2 = -dt^2 + \frac{a^2(t)dr^2}{1 - kr^2} + a^2(t)(d\theta^2 + \sin^2\theta d\phi^2), \tag{1.8}$$

where k denotes the (constant) curvature of spatial sections, and $a(t)$ is the scale factor of the universe, normalised to unity at $t = t_0$. There exists a global spacelike singularity at $a = 0$. The metric may be written in explicitly conformal coordinates by substituting $dt = a\ d\eta$, and the redshift between comoving observers is directly related to the scale factor, $a = (1 + z)^{-1}$. The cosmic time coordinate t is the proper time of observers who are comoving with the cosmological fluid.

The G_{ij} components of the field equations give the Friedmann equation ($\dot{} \equiv \frac{d}{dt}$),

$$\left(\frac{\dot{a}}{a}\right)^2 = \frac{8\pi G}{3}\rho(a) - \frac{kc^2}{a^2} + \frac{\Lambda}{3}, \tag{1.9}$$

which is given here for a Universe with matter, curvature and a cosmological constant only. This can be solved to give the scale factor, $a(t)$, the evolution of which depends on the energy content of the Universe. The terms on the right-hand side of the Friedmann equation can be rewritten as (effective) fractions of the energy density in the Universe today,

$$H^2 = H_0^2 \left(\Omega_m a^{-3} + \Omega_K a^{-2} + \Omega_\Lambda\right) \tag{1.10}$$

$$H_0^2 \Omega_m = \tfrac{8\pi G}{3}\rho_0; \quad H_0^2 \Omega_K = -kc^2; \quad H_0^2 \Omega_\Lambda = \tfrac{\Lambda}{3}, \tag{1.11}$$

where $H(a) \equiv \dot{a}/a$ is the expansion (Hubble) rate. The Hubble rate today is conventionally given in the units $H_0 = 100h$ km s^{-1} Mpc^{-1}, where h is dimensionless.

The G_{00} component of the field equations and the stress-energy conservation equation give, respectively, the Raychaudhuri and energy conservation equations,

$$\begin{aligned} \frac{\ddot{a}}{a} + \frac{4\pi G}{3}(\rho + 3p) &= 0 && (1.12) \\ \dot{\rho} + 3H(\rho + p) &= 0. && (1.13) \end{aligned}$$

1.1.3 Perturbations to FLRW

A perfectly homogeneous and isotropic FLRW solution cannot, on its own, provide a realistic description of the Universe – some way must be found to describe matter inhomogeneities such as galaxies, clusters, and voids. In the standard cosmological model, this has been achieved through the development of *cosmological perturbation theory* [Lifshitz, 1946; Peebles, 1980; Bardeen, 1980; Kodama & Sasaki, 1984]. This takes FLRW as a *background model* and introduces small metric perturbations on top of it to describe inhomogeneities.

In this section, I briefly summarise some useful results from cosmological perturbation theory on an FLRW background that will be required in later chapters.

For a more detailed pedagogical treatment, see Dodelson [2003] (from which the results in this section are mostly taken). For more technical discussions, see (for example) Peebles [1980]; Bardeen [1980]; Mukhanov *et al.* [1992]; Durrer [1994]; Ma & Bertschinger [1995].

The perturbed FLRW metric in Newtonian gauge is given by the line element (for scalar perturbations only)

$$ds^2 = -(1+2\Psi)dt^2 + (1+2\Phi)\left[\frac{a^2dr^2}{1-kr^2} + a^2 d\Omega^2\right]. \tag{1.14}$$

When the anisotropic stress is negligible (i.e. at late times), $\Phi = \Psi$, and Φ is analogous to the gravitational potential in Newtonian theory on small scales. This metric can be used to derive the perturbed Einstein field equations. When combined with the Boltzmann equations, these give a hierarchy of equations which describe the evolution of perturbations to the stress-energy for a fluid made up of multiple interacting components. It is useful to separate out the perturbations from the background by writing $\rho(\vec{x}) = \bar{\rho}(1+\delta(\vec{x},t))$, where $\bar{\rho}$ is the background energy density, and δ the *density contrast*. There are also perturbations to the fluid velocity, given by v (in the comoving frame).

For the most part, it is advantageous to work in Fourier space,

$$\delta(\vec{k}) = \int d^3x\delta(\vec{x})e^{-i\vec{k}\cdot\vec{x}}. \tag{1.15}$$

The wavenumber, k, should not be confused with the background spatial curvature. At late times (when radiation can be neglected), to linear order, the cold dark matter perturbations in the Conformal Newtonian gauge evolve according to the Poisson, continuity, and momentum conservation equations ($' \equiv \frac{d}{d\eta}$),

$$\begin{aligned} 4\pi G\bar{\rho}_m a^2(\delta + 3aHiv/k) &= k^2\Phi && (1.16)\\ \delta' + ikv &= -3\Phi' && (1.17)\end{aligned}$$

$$v' + (a'/a)v = -ik\Psi. \tag{1.18}$$

The space and time dependence of the perturbations are separable at linear order, so one can write $\delta(k, a) = D(a)\delta(k, a = 1)$, where the linear growth factor is

$$\frac{D(a)}{D(a=1)} = H(a) \int \frac{d\tilde{a}}{(\tilde{a}H(\tilde{a}))^3}, \tag{1.19}$$

at late times, in the matter-dominated case. The linear growth rate is defined as

$$f(a) = \frac{d \log D}{d \log a}. \tag{1.20}$$

The solution of the full system of perturbation equations requires an appropriate set of initial conditions. These are provided by inflation, which produces Gaussian random initial perturbations Φ_i of mean zero, with an almost scale-invariant power spectrum. The subsequent growth of the perturbations has a scale dependence given by the transfer function, $T(k)$, which depends on the matter and radiation content of the Universe.

Since the initial conditions are random in nature, it is useful to work with statistical quantities related to the probability distribution from which they are drawn. This allows us to make theoretical predictions that require only a model of the underlying probability distribution, rather than a detailed representation of any given realisation. For density perturbations, the matter power spectrum is defined by

$$\langle \delta(\vec{k})\delta^*(\vec{k'}) \rangle = (2\pi)^3 P(\vec{k'})\delta(\vec{k} - \vec{k'}), \tag{1.21}$$

where angle brackets denote averaging over the ensemble of all possible realisations[1]. The matter power spectrum gives the variance of density perturbations as a function of scale, and is a key cosmological quantity. Its real-space counterpart

---

[1] The ergodic theorem allows us to reinterpret ensemble averages as spatial averages if the probability distribution from which the realisations are drawn is homogeneous [Weinberg, 2008], and the spatial average is taken over a sufficiently large domain.

is the correlation function,

$$\begin{aligned} \xi(\vec{x}-\vec{x}') &\equiv \langle\delta(\vec{x})\delta(\vec{x}')\rangle && (1.22)\\ &= \int \frac{d^3k}{(2\pi)^3} P(k) e^{i\vec{k}\cdot(\vec{x}-\vec{x}')}. && (1.23) \end{aligned}$$

Neither the power spectrum nor the correlation function are directly observable, because they are defined on spacelike hypersurfaces. Since we are always restricted to making observations down our past lightcone (i.e. a null hypersurface), it is necessary to disentangle these functions from time-evolution effects when trying to estimate them observationally.

Many astronomical observations lack distance information, and so only an angular distribution is observed. A 2D field $F(\theta,\phi)$ can be decomposed into spherical harmonics,

$$F(\theta,\phi) = \sum_{\ell=1}^{\infty} \sum_{m=-\ell}^{\ell} a_{\ell m} Y_{\ell m}(\theta,\phi). \quad (1.24)$$

The 2D (angular) power spectrum is

$$C_\ell = \frac{1}{2\ell+1} \sum_{m=-\ell}^{\ell} a_{\ell m} a^*_{\ell m}. \quad (1.25)$$

This can be related to theoretical quantities by calculating the projected 3D power spectrum, for example.

1.1.4 The Cosmological Principle

In this section, I review one of the fundamental assumptions on which the concordance cosmological model is based: that of the homogeneity and isotropy of space. This assumption can be expressed in terms of two related principles, which I will now define.

1.1.4.1 Copernican Principle

The Copernican Principle states that the Earth does not occupy a special, central place in the Universe. Although non-geocentric models had been proposed in antiquity (notably by Aristarchus of Samos), and featured in some Hindu and Islamic cosmologies from the Middle Ages [van der Waerden, 1987], it wasn't until the introduction of the heliocentric model of Copernicus [1543] that this idea gained wide acceptance. By removing the notion that we inhabit a privileged location in the cosmos (which was theologically suggestive of the action of a 'creator'), the Copernican model fomented the Scientific Revolution which has today resulted in a wholly naturalistic description of the world.

More broadly, the Copernican Principle may be taken to mean that conditions in the vicinity of the Earth are in some sense *typical* of those elsewhere in the Universe – for example, that the laws of physics discovered here are representative of those in other locations. Without some form of Copernican Principle, cosmology would become extremely difficult, since it would not be possible to extrapolate results found locally and apply them to remote objects. It is implicitly assumed, for example, that the laws governing the scattering of photons from electrons are the same now as the ones that applied at last scattering, over 10 Gpc away (and 13 billion years ago).

In what follows, the term 'Copernican Principle' will be taken to refer to the statement that *our spatial position is not special or central.* As in (almost) all work in this field, the broader meaning – that the laws of physics are the same everywhere – is implicitly assumed.

1.1.4.2 Cosmological Principle

The Cosmological Principle (CP) is an extension of the Copernican Principle. First stated by Milne [1935], the CP holds that there are *no* privileged locations in the Universe – i.e. space is homogeneous and isotropic, the same at all locations, and in all directions. This implies that *all* observers are in some sense typical, and see a qualitatively similar view of the cosmos. As currently applied in cosmology, the CP refers only to homogeneity and isotropy on average, over large scales; at smaller scales, the matter distribution is inhomogeneous. It must also be distinguished from the *perfect cosmological principle*, which would require homogeneity in space *and time*; this has been ruled-out by the observation that the Universe was much hotter and denser in the past.

It is important to clarify here that the CP is generally taken to refer to spacetimes that are both homogeneous and isotropic – i.e. the FLRW spacetime, or special cases of it. There are a number of classes of solutions to the field equations that are homogeneous (in the sense that they can be foliated so that their spacelike hypersurfaces admit at least three Killing vectors [Pontzen & Challinor, 2007]), without being isotropic – these are the Bianchi models [Ellis, 2006].

1.1.4.3 Testing the Cosmological Principle

Milne called the Cosmological Principle “the grandest rule of extrapolation that can be imagined” [Milne, 1935]. In applying it, we are taking observations about a single point, taken over a timespan of mere decades, and using them to make inferences about the whole Universe. To place such a principle at the very foundations of cosmology without any empirical support would put us in a very precarious position indeed, and so I will now discuss the evidence that justifies cosmology’s continued reliance on the CP.

One of the most convincing lines of evidence for the CP is indirect. As noted earlier in this section, the concordance model is based on the exactly homogeneous and isotropic FLRW spacetime, which explicitly satisfies the CP. Also noted was the tremendous success of the model in matching observations – an FLRW model, albeit one with troubling additions in the form of the ‘dark sector’, appears capable of fitting the vast majority of cosmological observations that have been made to date. The implication, then, is that because the FLRW spacetime is consistent with observations on large scales, so too is the Cosmological Principle.

This, on its own, is not enough to confirm the CP. The high degree of symmetry assumed in the FLRW solution makes it *sufficient* to explain the near-perfect isotropy of the Cosmic Microwave Background (CMB) and other astrophysical observables, but it remains to be demonstrated whether it is the *only* spacetime geometry that is compatible with the data. One must then ask, what observables are required in order to prove beyond reasonable doubt that the Universe is FLRW on large scales?

An important step toward answering this question was provided by Ehlers, Geren and Sachs (EGS) [Ehlers *et al.*, 1968], and later fleshed out by others [Ferrando *et al.*, 1992; Clarkson & Barrett, 1999] (see Clarkson & Maartens [2010] for a review). These authors showed that isotropy of the CMB about every point in a region of spacetime is only possible if the geometry of spacetime in that region is spatially homogeneous and isotropic. This result is perturbatively stable in the sense that *near* isotropy of the CMB implies *near* homogeneity and isotropy of spacetime, although this requires extra assumptions to be made about unobservable quantities (such as that spatial derivatives of the CMB temperature are small) [Maartens *et al.*, 1995b,a; Stoeger *et al.*, 1995; Räsänen, 2009b]. An alternative proof of spatial homogeneity using luminosity distances was found by Hasse & Perlick [1999].

While compelling, these theorems all require observations to be made at *all* points in a region of spacetime to make definite conclusions. Since such observations are not available (i.e. we are restricted to making observations from a single point), one must instead turn to the Copernican Principle. By arguing that observations such as the (almost-) isotropy of the CMB on our own sky are typical of all observers, the CP can be proved. But this simply replaces the assumption of the CP with the assumption of the Copernican Principle, which also lacks direct observational confirmation. Furthermore, isotropy of the CMB is technically not even sufficient to determine that our local region of space is isotropic around us [Maartens, 2011].

Maartens & Matravers [1999] have shown that in order to determine whether the Universe is isotropic around us it is necessary and sufficient to have isotropic observations of luminosity distances, number counts, lensing, and angular peculiar velocities at every redshift, and in every direction. To then determine spatial homogeneity requires an extra independent observable beyond these four, unless one is prepared to specify the value of Λ *a priori* [Mustapha *et al.*, 1997] (assuming dark energy is due to the cosmological constant; if dark energy is dynamical then there is an extra functional degree of freedom to determine observationally, complicating the situation even more). While this prescription for determining spatial homogeneity and isotropy has the important quality of relying solely on directly observable quantities, rather than the Copernican Principle, it also requires large amounts of information from a number of different observables.

In Chapter 3, I consider a spherically-symmetric cosmological model that violates the Copernican Principle. Such models are capable of satisfying observational constraints such as the isotropy of the CMB without being homogeneous on large scales. In Chapter 4, I briefly discuss a method for proving the CP that depends only on observations of scattered CMB radiation. As with the method of Maartens & Matravers [1999] this does not rely on the Copernican Principle, but the number of observations required is much smaller.

1.2 Inhomogeneous cosmological spacetimes

Spacetime is inhomogeneous, at least on small scales. While the concordance model is based on an exactly homogeneous and isotropic FLRW solution, a number of inhomogeneous, exact relativistic solutions exist that could also form the basis of an observationally-viable cosmological model [Stephani *et al.*, 2003; Bolejko *et al.*, 2009, 2011a]. General relativistic descriptions of inhomogeneous matter distributions suggest that a number of effects may have been left unaccounted for in the concordance model, due to its high degree of symmetry or its perturbative (non-exact) approach. These could potentially cause drastic misinterpretations of cosmological observations, and may even offer an alternative explanation to the dark energy problem [Ellis, 2009, 2011; Clarkson *et al.*, 2011; Andersson & Coley, 2011].

In this section, I begin by discussing the various ways of modelling matter inhomogeneities that have been discussed in the literature. I then outline how general inhomogeneities can be dealt with mathematically within GR, and give an example of a potentially viable inhomogeneous spacetime. Finally, I discuss a number of issues surrounding the relativistic treatment of matter inhomogeneities, including the averaging and backreaction problems.

1.2.1 Relativistic models of inhomogeneity

Constructing relativistic models of the real, inhomogeneous Universe is difficult, but a number of attempts have met partial success in addressing the problem. Realistic density fields can be described using perturbations to exact FLRW solutions, as discussed in Section 1.1.3. However, at least to second order in perturbations, the effect of inhomogeneities on the overall behaviour of the spacetime often turns out to be small, with the average evolution and optical properties of the model remaining close to the unperturbed background values [Ishibashi & Wald, 2006; Green & Wald, 2011; Kolb *et al.*, 2005; Paranjape, 2009; Kasai *et al.*, 2006; Räsänen, 2010; Flanagan, 2005; Hirata & Seljak, 2005; Geshnizjani *et al.*, 2005; Weinberg, 1976; Bonvin *et al.*, 2006; Baumann *et al.*, 2012]. There have been suggestions that effects at higher orders in perturbations could be important [Clarkson & Umeh, 2011; Räsänen, 2010], and recent studies of non-linear collapse that make use of a ‘gradient expansion’ also find potentially significant effects [Enqvist *et al.*, 2012; Rigopoulos & Valkenburg, 2012]. These claims require further analysis if they are to be confirmed, however. The main drawback of the perturbative approach is that the solutions obtained are not exact, and so it is unclear if we are neglecting or incorrectly estimating aspects of the fully-relativistic behaviour of the spacetime.

An alternative approach involves studying exact, inhomogeneous solutions to Einstein's equations. As the geometry of spacetime is known from the outset, the exact non-linear evolution of space, and light rays within it, can be calculated in a fully consistent manner, without recourse to perturbative analyses. Usable exact solutions tend to have a high degree of symmetry, however, placing strong restrictions on what it is possible to model [Ellis & Jaklitsch, 1989]. For example, Swiss Cheese models constructed by joining together spherically-symmetric inhomogeneous regions with a FLRW solution retain a high degree of symmetry if the junction conditions between the background and spherical regions are satisfied exactly. These are known to have only small backreaction effects [Mattsson & Mattsson, 2010], a fact that is confirmed by ray-tracing studies through a variety of similar exact solutions [Mattsson & Mattsson, 2010; Meures & Bruni, 2012; Di Dio *et al.*, 2012; Szybka, 2011; Brouzakis *et al.*, 2007; Vanderveld *et al.*, 2008; Bolejko & Célérier, 2010; Clifton & Zuntz, 2009]. Additionally, inhomogeneous models with general fluid content are difficult to work with [Bolejko & Lasky, 2008; Clarkson & Regis, 2011; Marra & Pääkkönen, 2012], and so most modelling attempts make do with a dust-only stress-energy tensor. This is also problematic, as high-density regions tend to rapidly collapse in inhomogeneous pressureless fluids, forming singularities and resulting in unrealistic, pathological behaviour.

Finally, more heuristic analyses have been attempted [Lindquist & Wheeler, 1957; Kantowski *et al.*, 1995; Räsänen, 2006a,b, 2009c; Clifton & Ferreira, 2009; Mattsson & Mattsson, 2010; Räsänen, 2010b]. These often employ disjoint regions of different exact solutions. The dynamical evolution within each region is therefore well-defined, but the ensemble as a whole does not satisfy Einstein's equations at the boundaries between regions. This approach relaxes the restrictive symmetry requirements that are often necessary when using exact solutions, but introduces its own ambiguities. Indeed, the chosen boundary conditions can sometimes dominate the behaviour of the model [Clifton & Ferreira, 2009], and it is not clear whether the resulting spacetime approximates any actual solution of Einstein's equations or not.

1.2.2 1+3 decomposition

In this section, I discuss a formalism for describing relativistic inhomogeneities in a general spacetime. A congruence of time-like geodesics, u^a, describing the world-lines of a set of observers comoving within a cosmological fluid can be decomposed such that [Ellis, 1971; Ellis & van Elst, 1998]

$$\nabla_b u_a = \frac{1}{3}\Theta h_{ab} + \sigma_{ab} + \omega_{ab}, \tag{1.26}$$

where $h_{ab} = g_{ab} + u_a u_b$ is the projection tensor. The kinematic quantities in this equation are the expansion scalar, Θ, the shear, σ_{ab}, and the vorticity, ω_{ab}, which correspond to the trace, symmetric trace-free, and antisymmetric parts of $\nabla_b u_a$, respectively. This decomposition is a fully covariant procedure, valid for any spacetime.

For irrotational flows ($\omega_{ab} = 0$), the fluid flow becomes hypersurface orthogonal, with the projection tensor becoming the induced metric of the orthogonal 3-spaces. The field equations then give (with $8\pi G = 1$)

$$\dot{\Theta} = -\frac{1}{3}\Theta^2 - \frac{1}{2}(\rho + 3p) + \Lambda - 2\sigma^2, \tag{1.27}$$

where the over-dot denotes a derivative with respect to proper time along u^a, and where $\sigma^2 = \frac{1}{2}\sigma_{ab}\sigma^{ab}$, and ρ, p and Λ are the energy density, pressure and cosmological constant, respectively. The Gauss embedding equation for these hypersurfaces is

$$\frac{1}{3}\Theta^2 = \rho + \Lambda + \sigma^2 - \frac{1}{2}{}^{(3)}\mathcal{R}, \tag{1.28}$$

where ${}^{(3)}\mathcal{R}$ is the Ricci scalar constructed from h_{ab}.

1.2.3 An example inhomogeneous spacetime: LTB

In order to model general radial inhomogeneity, I will use the Lemaître-Tolman-Bondi (LTB) solutions of general relativity. These are given by the line-element [Lemaître, 1933; Tolman, 1934; Bondi, 1947]

$$ds^2 = dt^2 - \frac{a_2^2(t,r)}{1-k(r)r^2}dr^2 - a_1^2(t,r)r^2 d\Omega^2, \tag{1.29}$$

where $a_2 = (a_1 r)'$, and a_1 must satisfy

$$\left(\frac{\dot{a}_1}{a_1}\right)^2 = \frac{8\pi G}{3}\frac{m(r)}{a_1^3} - \frac{k(r)}{a_1^2}. \tag{1.30}$$

The scale factor is not directly related to redshift as it is in FLRW models (i.e. $a_1 \neq (1+z)^{-1}$). The functions $k(r)$ and $m(r)$ are arbitrary functions of the radial coordinate, and primes and over-dots denote partial derivatives with respect to r and t, respectively. These solutions are exact, and are the general spherically symmetric dust-only solutions to Einstein's equations. They admit a three dimensional group of Killing vectors that act transitively on the surfaces of constant r and t, and are spatially isotropic about the origin only.

Solutions to Eq. (1.30) are of the form $a_1 = a_1(r, t - t_B(r))$, which introduces a third arbitrary function of r. This gives a total of three free functions: $k(r)$, $m(r)$ and $t_B(r)$. I will refer to these quantities as the spatial curvature, gravitational mass density (distinct from the local energy density) and bang time, respectively.

In the limit of homogeneity they are all constant. One can perform a coordinate transformation $r \mapsto f(r)$ that preserves the form of the metric in Eq. (1.29). This freedom can be used to set $m =$ constant without loss of generality (as long as $(mr^3)'$ does not change sign, so that the corresponding coordinate transformation remains single-valued [Plebański & Krasiński, 2006]). This leaves us with the general solution in terms of the spatial curvature, $k(r)$, and bang time function, $t_B(r)$, only. Analytic parametric solutions to Eq. (1.30) are known, and can be found in Zecca [1991].

One can define two different Hubble rates: a transverse one, $H_1 \equiv \dot{a}_1/a_1$, and a radial one, $H_2 \equiv \dot{a}_2/a_2$. In the limit of homogeneity these two quantities are identical, but differ in general in inhomogeneous spacetimes. The local energy density, expansion, and shear scalars in LTB are given by

$$\rho = \frac{(mr^3)'}{3a_2a_1^2r^2} \tag{1.31}$$

$$\Theta = 2H_1 + H_2 \tag{1.32}$$

$$\sigma^2 = \frac{1}{3}(H_1 - H_2)^2. \tag{1.33}$$

1.2.4 Backreaction, fitting, and averaging

The concordance model described in Section 1.1 is founded on the Cosmological Principle, which specifies that space is homogeneous and isotropic on large scales. This must be reconciled with our observations, which reveal a lumpy, inhomogeneous distribution of matter on small scales. It is often assumed that the two regimes are automatically bridged by the perturbed FLRW framework described in Section 1.1.3: the background FLRW model describes the behaviour of the homogeneous matter distribution on large scales, and metric perturbations – which average away to nothing on sufficiently large scales – describe small-scale inhomogeneity.

There are indications that the connection between these regimes is considerably more subtle, however [Ellis & Buchert, 2005; Räsänen, 2010a; Clarkson *et al.*, 2011; Andersson & Coley, 2011]. Note that the perturbed FLRW models are only approximate solutions to the field equations. The validity of this approximation has been called into question in some situations (e.g. Clarkson & Umeh [2011]), giving rise to suggestions that the standard perturbative framework may be neglecting potentially important relativistic effects that link large and small scales [Buchert *et al.*, 2000; Schwarz, 2002; Kolb *et al.*, 2005, 2008; Kolb, 2011; Buchert & Räsänen, 2012]. There are, however, claims to the contrary, which state that the standard perturbed FLRW solution is sufficient for modelling the matter distribution up to a density contrast potentially as large as that of a neutron star [D'Eath, 1976; Ishibashi & Wald, 2006; Green & Wald, 2011].

If we sidestep these concerns and instead consider exact, inhomogeneous relativistic solutions to the field equations, the connection between large and small scales becomes even less clear. For example: defining a consistent procedure for averaging an inhomogeneous spacetime to produce a homogeneous model on large scales is difficult [Shirokov & Fisher, 1963; Ellis, 1984; van den Hoogen, 2011]; the nonlinearity of the GR field equations allows small-scale dynamics to affect behaviour on large scales [Futamase, 1988; Buchert *et al.*, 2000; Schwarz, 2002; Räsänen, 2004b; Kolb *et al.*, 2005]; and the FLRW model that best fits observations may not be the same as the one that best describes its dynamical evolution [Ellis & Stoeger, 1987]. These are the *averaging*, *backreaction*, and *fitting* problems, respectively, which I will now discuss in more detail.

1.2.4.1 Averaging problem

By smoothing an inhomogeneous spacetime over large enough scales, one can imagine producing a spatially homogeneous 'average' representation that faithfully describes its large-scale dynamics. The question is, what is the most consistent, meaningful way of doing the smoothing? This is the *averaging problem*.

Unfortunately, it is not easy to define a consistent spatial averaging procedure within the context of general relativity [van den Hoogen, 2011; Wiltshire, 2011; Andersson & Coley, 2011]. Much of the mathematics of GR concerns tensor fields defined over a manifold. Averaging a tensor over a given hypersurface (i.e. integrating the tensor field) requires some way of adding together tensors defined at different points in spacetime, but defining this addition in a covariant manner can be very complicated in a non-Euclidean space [van den Hoogen, 2011]. One could imagine parallel-transporting a tensor from one point to another along some curve, for example, and then performing the addition [Isaacson, 1968], but this would require a system of curves linking every point on the manifold to every other point, and there would be considerable freedom in how to define the curves. Other proposed methods for averaging tensors run into similar difficulties [Zalaletdinov, 1992; van den Hoogen, 2011].

An alternative is to define an averaging method that relies only on scalar quantities, as these can be readily averaged. Some geometrical quantities can be partially decomposed into scalars, as shown in Section 1.2.2. By averaging these, one can hope to construct an average model that captures at least some information from the full spacetime geometry. One such method is outlined in Section 1.2.5, but its physical interpretation is not clear; it is possible to have an inhomogeneous spacetime with an expansion rate that is locally decelerating everywhere, but which has an accelerating average. This issue is addressed in detail in Chapter 2.

1.2.4.2 Backreaction

Whichever averaging procedure is applied, the aim is generally to produce a model of the Universe on large scales with a geometry described by a FLRW metric and a matter distribution described by a homogeneous FLRW stress-energy tensor. The GR field equations are nonlinear, however, so the averaged field equations are in general different from the field equations derived from the averaged metric,

$$\begin{aligned} \langle G(g) \rangle &= 8\pi G \, \langle T \rangle \qquad (1.34) \\ &\neq G(\langle g \rangle). \qquad (1.35) \end{aligned}$$

The difference is given by the *correlation tensor*,

$$C_{ab} = G_{ab}(\langle g \rangle) - 8\pi G \, \langle T_{ab} \rangle, \qquad (1.36)$$

which is taken to parametrise the *backreaction* effects of small-scale structure on the large-scale behaviour of the spacetime.

If the correlation tensor vanishes, then the averaged metric also gives the averaged field equations, and so a FLRW solution on its own gives a fully-consistent description of the Universe. If it doesn't vanish, on the other hand, the correlation tensor could be interpreted as an additional contribution to the stress-energy, $T^{\rm eff}_{ab} = T_{ab} + C_{ab}$. It has been argued that backreaction effects could in fact be responsible for the apparent cosmic acceleration [Buchert *et al.*, 2000; Schwarz, 2002; Räsänen, 2004b; Kolb *et al.*, 2005; Räsänen, 2011; Andersson & Coley, 2011], since this could also be caused by an additional term in the stress-energy (c.f. dark energy or quintessence). Backreaction would also solve the *coincidence problem* [Arkani-Hamed *et al.*, 2000], which asks why cosmic acceleration happens to kick in at around the same time that structure begins to grow into the nonlinear regime.

The size of the backreaction effect in our own Universe remains unknown. Contrary to claims that it could be big enough to explain cosmic acceleration, some have suggested that it is negligibly small, on the order of the size of the FLRW metric perturbations (e.g. Ishibashi & Wald [2006]; Green & Wald [2011]; Mattsson & Mattsson [2011]; Clifton [2011]). Others have argued that it could be non-negligible [Clarkson & Umeh, 2011], but perhaps only a $1-10\%$-level effect [Li & Schwarz, 2008; Enqvist *et al.*, 2012; Bolejko & Ferreira, 2012]. I will examine the backreaction effect in more detail in Chapter 2.

1.2.4.3 Fitting problem

A common task is to find the set of FLRW model parameters that correspond to the real Universe by fitting to observational data. One can then make predictions for how the Universe will evolve in future, infer its energy content, and so on, using the corresponding solution to the Friedmann equation.

Our real spacetime cannot actually be a perturbed FLRW model though, since that would not be an exact solution to the field equations. Instead, the FLRW background model is a fictitious, idealised entity that is constructed for theoretical convenience, and which gives a good approximation to whatever the real, complicated, inhomogeneous metric of spacetime is on large enough scales.

Given this, what is the physical meaning of the FLRW model that best fits our observations? The hope is that the best-fit model also describes the (average) evolution of spacetime. The *fitting problem*, posed by Ellis & Stoeger [1987], asks what is the best way of fitting an idealised FLRW model to the real, inhomogeneous spacetime using observational data so as to also recover a good model of the Universe's average dynamics.

In order to estimate FLRW model parameters from data, one normally calculates predictions for the observable in question within a perturbed FLRW framework (possibly coupled with the results of N-body simulations) and then finds the set of FLRW model parameters that best fits the data. Ellis & Stoeger [1987] showed that this is only one possible method – others, such as averaging observables down the past lightcone, or directly inverting them into functions that define the spacetime geometry, also exist. In Chapter 2, I discuss the relationship between FLRW models fitted to observations in, and the average dynamics of, an inhomogeneous spacetime, and show that the two need not be the same.

1.2.5 The Buchert scalar averaging formalism

The Buchert formalism is a covariant (but foliation-dependent) procedure for spatially averaging scalar quantities [Buchert *et al.*, 2000; Buchert, 2000; Buchert & Räsänen, 2012][1]. It can be used to construct a homogeneous effective model from a given inhomogeneous spacetime, and is the most widely used averaging formalism in the literature.

Buchert's method proceeds as follows. First of all, the spacetime is filled with a congruence of (irrotational) curves. It is then foliated with a set of spacelike hypersurfaces orthogonal to these curves. The proper 3-volume of a domain, $\mathcal{D}$, on a given spacelike hypersurface is

$$V_{\mathcal{D}} = \int_{\mathcal{D}} \sqrt{-h}\; d^3x, \tag{1.37}$$

where h_{ij} is the induced metric on the hypersurface, and $h = \det h_{ij}$. In general, the induced metric will be a function of time, and so the volume is time-dependent as well. The proper volume-weighted average of a scalar quantity, S, over a spatial domain, $\mathcal{D}$, can then be written as

$$\langle S \rangle = V_{\mathcal{D}}^{-1} \int_{\mathcal{D}} S(\vec{x}, t)\sqrt{-h}\; d^3x. \tag{1.38}$$

Spatial averaging and time evolution do not, in general, commute. They instead obey the commutation relation

$$\partial_t \langle S \rangle - \langle \partial_t S \rangle = \langle \Theta S \rangle - \langle \Theta \rangle \langle S \rangle. \tag{1.39}$$

An 'effective' homogeneous model can be constructed by averaging over domain sizes greater than the statistical homogeneity scale of the underlying inhomogeneous spacetime. An effective scale factor for the resulting model can then be

---

[1] See also an earlier attempt at constructing a similar formalism, by Marochnik *et al.* [1975]; Krymsky *et al.* [1978].

defined as

$$a_{\mathcal{D}}(t) = \left(\frac{V_{\mathcal{D}}(t)}{V_{\mathcal{D}}(t_0)}\right)^{\frac{1}{3}}, \tag{1.40}$$

where t_0 is some fiducial time. For geodesic curves, and pressure-free matter, one can use this formalism to construct analogues to the Friedmann and Raychaudhuri equations,

$$\begin{aligned} 3H_{\mathcal{D}}^2 &= 8\pi G\langle\rho\rangle + \Lambda - \frac{1}{2}\left(Q_{\mathcal{D}} + \langle{}^{(3)}\mathcal{R}\rangle\right) \\ 3\frac{\ddot{a}_{\mathcal{D}}}{a_{\mathcal{D}}} &= -8\pi G\langle\rho\rangle + \Lambda + Q_{\mathcal{D}}, \end{aligned} \tag{1.41}$$

where $H_{\mathcal{D}} = \dot{a}_{\mathcal{D}}/a_{\mathcal{D}}$. Over-dots denote partial differentiation with respect to t, the proper time along curves orthogonal to the 3-space. The *kinematical backreaction scalar* is defined to be

$$Q_{\mathcal{D}} = \frac{2}{3}\left(\langle\Theta^2\rangle - \langle\Theta\rangle^2\right) - 2\langle\sigma^2\rangle. \tag{1.42}$$

1.3 Light propagation and the Sachs Equations

In this section, I outline a mathematical formalism due to Sachs [1961] for calculating how light propagates in a general relativistic spacetime. The formalism is a vital tool for studying the observational consequences of inhomogeneities, and is the basis of several approximations that are commonly used to relate observables to the properties of spacetime.

This section consists of a brief overview of the Sachs optical equations, their conceptual basis, and examples of their application. The intention here is not to give a detailed derivation of these results, as this has been performed numerous times elsewhere (e.g. Sachs [1961]; Ellis [1971]; Seitz *et al.* [1994]; Perlick [2004]; Ellis *et al.* [2012]).

1.3.1 The Sachs formalism and optical scalars

The propagation of light in a general relativistic spacetime can be described using the Sachs equations. The Sachs equations are derived under the *geometric optics* approximation, which requires that (a) the phase of propagating light waves varies much more rapidly than the amplitude of the wave, and (b) that the light constitutes a test field that does not modify the curvature of spacetime as it travels [Ellis, 1971]. The former condition is essentially the statement that the wave nature of light can be ignored (i.e. diffraction is unimportant), and that the light can be treated as travelling in rays. In what follows, I will always treat light as travelling along rays.

The object of interest in Sachs' formalism is a *bundle* of light rays of infinitesimal cross-section, described by a congruence of null geodesics with tangent vector k^a, and affine parameter λ. The separation between some fiducial 'central' geodesic curve and an arbitrarily close neighbouring curve is described by a *connecting vector*, q^a [Seitz *et al.*, 1994]. As the bundle propagates, its shape and size is distorted by various focusing effects due to the curvature of spacetime, with the form of the distortions being captured by the vector field q^a.

It is useful to consider connecting vectors that are defined such that $k^a q_a = 0$ and $u^a q_a = 0$ (where, as usual, u^a is tangent to the worldlines of observers comoving with the dust fluid). Under these conditions, q^a spans a two-dimensional spacelike *screen space* in the rest frame of the observers, and is orthogonal to k^a [Ellis *et al.*, 2012]. By further decomposing q^a into two orthonormal vectors on the screen space, one arrives at a description of the shape and size of the bundle's cross-section in terms of an (infinitesimal) ellipse. This is analogous to what an observer at a particular instant in time would see projected onto a screen that intersects the bundle [Sachs, 1961; Ellis *et al.*, 2012].

The ellipse can be deformed in only a handful of ways. The simplest deformation is an overall scaling (expansion or contraction) of the ellipse, corresponding to a change in the surface area of the bundle in the screen space (and thus a dimming or brightening of the beam of light). The bundle may also be sheared, corresponding to a 'squashing' of the ellipse in one direction in the screen space relative to the other; and rotated, corresponding to a rotation of the principal axes of the ellipse. These deformations are each sourced differently, as will be seen shortly. In the Sachs formalism, the deformations are described by three scalar quantities: the *expansion scalar* (rate of expansion), θ; the (complex) *shear*, $\hat{\sigma}$; and *vorticity* (rotation), $\hat{\omega}$. The Sachs equations describe the evolution of these quantities as functions of the curvature of the spacetime in which the light rays are propagating.

1.3.2 Observable quantities

Astronomical observations are typically concerned with the apparent brightness and/or angular size of a source of radiation. The cross-sectional area of a bundle of rays is closely related to both of these quantities, and so the Sachs equations give us a way of inferring the properties of spacetime from observations. Importantly, for objects with known intrinsic luminosities or physical sizes, one can use the Sachs equations to define measures of distance. The *angular diameter distance* is given by

$$d_A = \sqrt{\frac{dS}{d\Omega}}, \tag{1.43}$$

where dS is the cross-sectional area of a source and $d\Omega$ is the solid angle it subtends, evaluated at the observer. For a *standard ruler*, dS is known, and so a measurement of $d\Omega$ gives d_A. Similarly, the *luminosity distance* is given by

$$d_L = \sqrt{\frac{L}{4\pi F}}, \tag{1.44}$$

where L is the intrinsic luminosity of the source and F is the flux at the observer. Again, for a *standard candle* (where L is known), a measurement of flux by an observer will yield d_L. The luminosity distance is related to the angular diameter distance by the *reciprocity theorem* [Etherington, 1933; Ellis *et al.*, 2012], which gives $d_L = (1+z)^2 d_A$.

1.3.3 The Sachs equations

I will now inspect the Sachs equations. Excluding vorticity (which is generally negligible for observables of cosmological interest), the Sachs equations are given by [Sachs, 1961]

$$\begin{aligned} \frac{d\theta}{d\lambda} + \theta^2 + |\hat{\sigma}|^2 &= -\frac{1}{2} R_{ab} k^a k^b && (1.45) \\ \frac{d\hat{\sigma}}{d\lambda} + 2\theta\hat{\sigma} &= C_{abcd} (t^*)^a k^b (t^*)^c k^d. && (1.46) \end{aligned}$$

where λ is an affine parameter along the bundle, R_{ab} and C_{abcd} are the Ricci and Weyl tensors of the spacetime, and t^a are (complex) vectors spanning a two-dimensional screen space orthogonal to k^a. The source terms of the evolution equations for the expansion and shear are functions of the Ricci and Weyl curvatures respectively. The expansion scalar depends on the Weyl curvature indirectly, through its coupling to the shear (likewise for the dependence of the shear on the Ricci curvature).

The expansion scalar is related to the angular diameter distance measured along the bundle by $\theta = d\log(d_A)/d\lambda$. Substituting this into Eq. (1.45) yields

$$\frac{d^2(d_A)}{d\lambda^2} = -d_A \left(|\hat{\sigma}|^2 + \frac{1}{2} R_{ab} k^a k^b \right). \tag{1.47}$$

By choosing appropriate initial conditions, this can be solved for a specific spacetime (and specific null curve) to give $d_A(\lambda)$. The affine distance is not an observable quantity though, so it is necessary to rewrite this relation as a function of redshift, z. The affine distance-redshift relation for a general spacetime is given by [Clarkson & Maartens, 2010]

$$\frac{dz}{d\lambda} = -(1+z)^2 H_{||}(z), \tag{1.48}$$

where $H_{||} = \frac{1}{3}\Theta + \sigma_{ab}e^a e^b$ is the expansion rate along the line of sight (which has spatial projection e^a). Equations (1.45)–(1.48) can be solved to give the angular diameter distance-redshift relation, $d_A(z)$, in any given direction, at any given point in spacetime.

1.3.4 Light propagation in an FLRW spacetime

In this section, I briefly outline some key results that are useful for calculating the distance-redshift relation in an FLRW spacetime.

1.3.4.1 Background distance-redshift relation

FLRW spacetimes are Weyl-flat ($C_{abcd} = 0$), and so the initial condition $\hat{\sigma}_0 = 0$ allows us to neglect the shear for the entire evolution of the light ray. The Sachs equations reduce to [Bolejko, 2011]

$$\frac{d^2 d_A}{dz^2} + \left(\frac{1}{H(z)}\frac{dH}{dz} + \frac{2}{1+z} \right) \frac{dd_A}{dz} + \frac{4\pi G\rho(z)}{(1+z)^2 H^2(z)} d_A = 0, \tag{1.49}$$

which is easy to solve numerically for a given expansion history, $H(z)$. In a Milne universe (vacuum FLRW), the luminosity distance takes a particularly simple form,

$$d_L^{\rm Milne}(z) = \frac{c}{H_0}\left(z + \frac{z^2}{2} \right). \tag{1.50}$$

It is often convenient to write luminosity distances in terms of a *distance modulus*,

$$\mu(z) = 5\log_{10}\left(\frac{d_L(z)}{d_L^{\rm Milne}(z)} \right), \tag{1.51}$$

which is more closely related to the magnitude system used by astronomers. This definition of distance modulus, which is normalised to a Milne model, has the property that a positive gradient with respect to redshift denotes acceleration of the FLRW spacetime, and a negative gradient denotes deceleration. The acceleration rate of an FLRW spacetime is related to derivatives of the luminosity distance by [Visser, 2004]

$$d_L(z) = \frac{cz}{H_0}\left(1 + \frac{1}{2}(1 - q_0)z + \mathcal{O}(z^2)\right), \tag{1.52}$$

where a Taylor expansion in redshift has been performed about $z = 0$, and q_0 is the *deceleration parameter*. In a FLRW spacetime, the deceleration parameter is defined by a Taylor expansion of the scale factor with respect to cosmic time [Visser, 2004],

$$\begin{aligned} a(t) &= 1 + H_0(t - t_0) - \frac{1}{2}q_0 H_0^2(t - t_0)^2 + \mathcal{O}([t - t_0]^3) && (1.53)\\ q_0 &= -H_0^{-2}\left.\frac{d^2a}{dt^2}\right|_0 . && (1.54)\end{aligned}$$

A value of $q_0 < 0$ denotes acceleration. A similar expansion can be performed for the angular diameter distance, giving

$$d_A(z) = \frac{cz}{H_0}\left(1 - \frac{1}{2}(3 + q_0)z + \mathcal{O}(z^2)\right). \tag{1.55}$$

1.3.4.2 Perturbed distance-redshift relation

Up to linear order in perturbations, the luminosity distance in a FLRW model may be written as [Bonvin *et al.*, 2006]

$$d_L(z_S) = (1 + z_S)(\eta_O - \eta_S)(1 + \delta_L), \tag{1.56}$$

where η is the conformal time, and S, O refer to quantities evaluated at the source and observer respectively. A full expression is given by Bonvin *et al.* [2006],

$$
\begin{aligned}
(\eta_O - \eta_S)\delta_L \;=\; & +\frac{(\mathbf{v}_S - \mathbf{v}_O)\cdot\mathbf{n}}{a_S H_S} - (\eta_O - \eta_S)\mathbf{v}_S\cdot\mathbf{n}/c \\
& +\frac{(\Psi_S - \Psi_O)}{a_S H_S} - (\eta_O - \eta_S)\Psi_S \\
& +2\int_{\eta_S}^{\eta_O} d\eta \left[\Psi + \frac{\Psi'}{a_S H_S} - (\eta - \eta_S)\Psi' + \frac{1}{2}(\eta - \eta_S)(\eta_O - \eta)\Psi''\right] \\
& -\int_{\eta_S}^{\eta_O} d\eta\; (\eta - \eta_S)(\eta_O - \eta)\nabla^2\Psi. \qquad (1.57)
\end{aligned}
$$

The terms on line 1 give Doppler shifts due to peculiar velocities, line 2 gives 'gravitational redshifts', line 3 gives integrated line-of-sight effects (such as the integrated Sachs-Wolfe effect), and line 4 is a weak lensing term. Using the reciprocity relation, and keeping only terms that are linear in perturbations, one can write the perturbation to the angular diameter distance as

$$
\delta_A = \delta_L - \frac{2\delta\bar{z}_S}{1 + z_S}, \qquad (1.58)
$$

where δ_L is the linear perturbation to d_L, given by Eq. 1.57, and $\delta\bar{z}_S$ is the source redshift perturbation that will be given in Eq. 4.2.

1.3.5 Compton scattering and the SZ effect

The Cosmic Microwave Background (CMB) radiation consists of photons that have been free-streaming since the time of last scattering, when the Universe first became transparent at redshift $z_* \approx 1090$. The photons have been measured to have an almost perfect blackbody frequency spectrum of temperature $T_0 \simeq 2.725$ K [Fixsen, 2009]. A wealth of information is contained in the small temperature anisotropies of the CMB, which carry the imprints of fluctuations in the matter density of the Universe that were seeded by inflation. It is also possible to observe secondary anisotropies in the CMB caused by the scattering of a small fraction of CMB photons by ionised gas associated with cosmic structure. This process is called the Sunyaev-Zel'dovich (SZ) effect. In this section, I briefly review the physics behind the SZ effect, and quote some useful results.

The spectral radiance[1] for a blackbody such as the primary CMB is given by Planck's Law,

$$B(\nu, T) = \frac{2h}{c^2} \frac{\nu^3}{e^x - 1}, \tag{1.59}$$

with $x = h\nu/k_B T$. Blackbody radiation retains its characteristic spectrum even after redshifting, up to a change in blackbody temperature $\tilde{T} = T(1+z)$ [Ellis, 1971]. The scattering of photons by free electrons is known as Compton scattering, and has an angle-dependent scattering cross-section [Marion, 1965]

$$\frac{d\sigma}{d\Omega} = \frac{3}{16\pi} \sigma_T (1 + \cos^2\theta) \tag{1.60}$$

(σ_T is the Thomson scattering cross-section). When low-energy photons are scattered by hot electrons, the photons gain energy, resulting in a characteristic shift of their frequency spectrum to higher energies known as *inverse Compton scattering.*

The scattering of CMB photons by the hot gas in galaxy clusters was first described by Sunyaev & Zel'dovich [1970], and can be divided into two related effects: the *thermal* and *kinematic* Sunyaev-Zel'dovich effects (TSZ and KSZ, respectively) [Sunyaev & Zel'dovich, 1970, 1980]. The thermal effect is due to the inverse Compton scattering of CMB photons by a thermal distribution of electrons, and has a characteristic spectral dependence that looks like a decrement in CMB temperature at low frequencies, and an increment at high frequencies. The kinematic effect is a Doppler shift caused by the bulk motion of the scattering electrons, and has a flat spectral dependence, making it difficult to distinguish from the primary CMB. Extensive reviews of the two effects, including detailed

---

[1] Spectral radiance has units of W $\mathrm{sr}^{-1}\mathrm{m}^{-2}\mathrm{Hz}^{-1}$.

derivations and corrections due to relativistic effects, can be found in Rephaeli [1995] and Birkinshaw [1999].

The thermal SZ effect seen in CMB maps can be used to detect galaxy clusters out to high redshift, and has been shown to be a good proxy for cluster mass [Motl *et al.*, 2005; Planck Collaboration, 2012b]. Observations of the TSZ effect have therefore been considered as a way of measuring the cluster mass function over large volumes [Battye & Weller, 2003]. While the kinematic effect is harder to measure, it has the potential to probe cluster peculiar velocities out to high redshift too [Bhattacharya & Kosowsky, 2007, 2008]. The cosmological applications of the KSZ effect will be discussed in more detail in Chapters 3, 4, and 5, and of TSZ in Chapter 5.

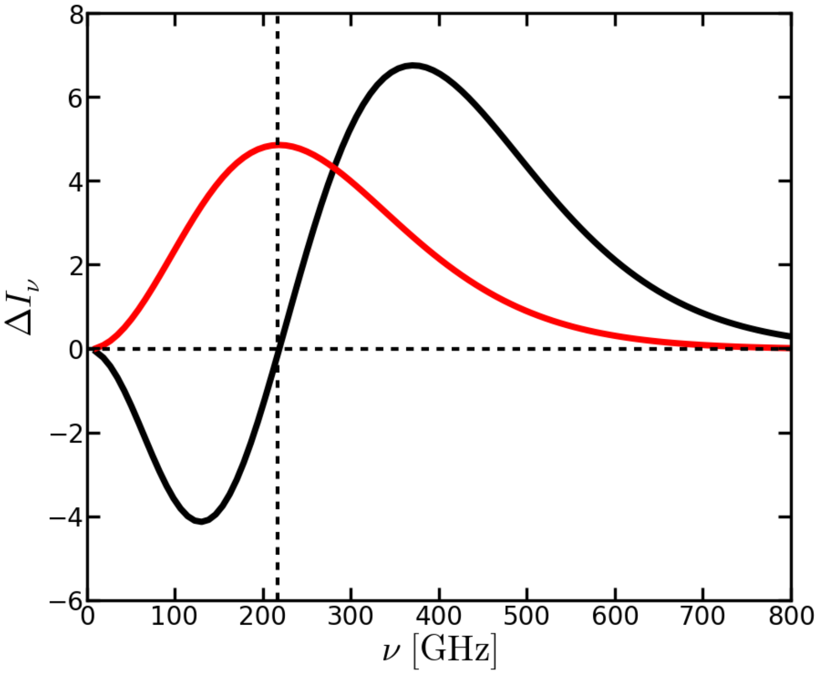

Figure 1.1: Change in CMB spectral intensity due to the thermal (black line) and kinematic (red line) Sunyaev-Zel'dovich effects (for arbitrary optical depth and velocity). Note the null in the TSZ spectrum at $\nu \approx 217$ GHz.

The change in spectral intensity for both effects in the limit of non-relativistic electrons is [Rephaeli, 1995]

$$\left.\frac{\Delta I(\nu)}{I_0}\right|_{\rm TSZ} = g_T(x)\frac{\sigma_T}{m_e c^2}\int k_B T(\hat{n}) n_e(\hat{n}) dl \tag{1.61}$$

$$= g_T(x)\frac{\sigma_T}{m_e c^2}\int P_e(\hat{n}) dl \tag{1.62}$$

$$\left.\frac{\Delta I(\nu)}{I_0}\right|_{\rm KSZ} = -g_K(x)\beta\tau, \tag{1.63}$$

where n_e is the number density of free electrons, P_e is the electron pressure, β is the peculiar velocity of the scattering electron cloud, and dl is the infinitesimal distance element along the line of sight. The optical depth along a line of sight is defined as $\tau \equiv \int \sigma_T n_e dl$, and the spectral dependences of the thermal and kinematic SZ effects are given by

$$g_T(x) = \frac{x^4 e^x}{(e^x-1)^2}\left[\frac{x(e^x+1)}{e^x-1} - 4\right] \tag{1.64}$$

$$g_K(x) = \frac{x^4 e^x}{(e^x-1)^2}. \tag{1.65}$$

There is a null in the spectrum for the TSZ at $\nu \approx 217$ GHz, which is where the KSZ spectrum peaks. In terms of an effective blackbody temperature change,

$$\left.\frac{\Delta T}{T}\right|_{\rm TSZ} = \frac{\sigma_T}{m_e c^2}\frac{g_T(x)}{g_K(x)}\int P_e(\hat{n}) dl \tag{1.66}$$

$$\left.\frac{\Delta T}{T}\right|_{\rm KSZ} = -\beta\tau. \tag{1.67}$$

It can be seen that the thermal effect is a genuine distortion of the blackbody spectrum, whereas the kinematic effect is only a temperature shift, with no additional spectral dependence. This makes it possible to differentiate between the primary CMB anisotropies and TSZ, due to their different spectral dependences, but not the CMB and KSZ. A methodology for extracting both effects from CMB sky maps will be discussed in detail in Chapter 5.

1.4 Statistical methods

In order to assess whether a theoretical model M fits the available data D, it is first necessary to evaluate the posterior probability distribution, $P(M|D)$ – the probability of the model given the data. This quantity is rarely amenable to direct evaluation, but may be rewritten as

$$P(M|D) = \frac{P(D|M)}{P(D)} P(M) \tag{1.68}$$

using Bayes' Theorem. The term $\mathcal{L} \equiv P(D|M)$ is the *likelihood*, $P(M)$ is the *prior* probability of the model, and $P(D)$ is generally taken to be a normalising constant. From a Bayesian perspective, one is free to choose the form of the prior according to *a priori* knowledge of the system under consideration. The problem of estimating the posterior distribution is therefore reduced to estimating the likelihood function.

1.4.1 Likelihood estimation

The evaluation of the likelihood depends on the properties of the dataset being used, but it can usually be evaluated using a combination of simple likelihood functions. For a single data point y with a Gaussian random error (i.e. y is a draw of some Gaussian random variate Y), the likelihood is given by

$$\mathcal{L} = \frac{1}{\sqrt{2\pi\sigma^2}} \exp\left[-\frac{(y-\tilde{y})^2}{2\sigma^2}\right], \tag{1.69}$$

where σ^2 is the error variance and $\tilde{y}$ is the expectation value of the data point given by a theoretical model. Clearly, the likelihood is maximised for $y = \tilde{y}$. For an uncorrelated set of such data points, the total likelihood is simply the product of the individual likelihoods,

$$\mathcal{L} = \prod_i \frac{1}{\sqrt{2\pi\sigma_i^2}} \exp\left[-\frac{(y_i - \tilde{y}_i)^2}{2\sigma_i^2}\right] \tag{1.70}$$

This may be generalised to include (Gaussian) correlated errors by writing

$$\mathcal{L} \propto \exp\left[-\frac{1}{2}\left(\mathbf{y} - \tilde{\mathbf{y}}\right)^{\mathrm{T}} \mathbf{C}^{-1} \left(\mathbf{y} - \tilde{\mathbf{y}}\right)\right], \tag{1.71}$$

where $\mathbf{C}$ is the covariance matrix that describes the correlations. If the individual data points are not Gaussian random variables, a different form for the likelihood of the individual data points must be used. In most cases of interest, this will be either a non-Gaussian distribution with a relatively simple form, or may be well-approximated as Gaussian.

Theoretical models typically depend upon a set of free parameters, $M(\{\theta\})$. By estimating the posterior distribution $P(\{\theta\}|D)$, one can find the values of the parameters that best fit the data (including an estimate of the goodness of the fit), and quantify degeneracies between the parameters. In many cases, only one or a few parameters may be interesting, and so it is necessary to *marginalise* over the uninteresting quantities. For a model with N parameters, $\{\theta_1, \theta_2, \cdots, \theta_N\}$, the marginal distribution for a single parameter θ_1 is given by

$$P(\theta_1|D) = \int d\theta_2 \int d\theta_3 \cdots \int d\theta_N \; P(\theta_1, \theta_2, \cdots, \theta_N|D). \tag{1.72}$$

For problems where there are many data points, or where the model is difficult or time-consuming to calculate, evaluating the likelihood can be computationally intensive. As such, it is desirable to reduce the number of likelihood evaluations required for any given calculation as much as possible. For models with a very small number of parameters (i.e. one or two), evaluating the likelihood over a discrete grid of parameter values and interpolating the result tends to be acceptable.

For higher-dimensional problems, however, such an approach is infeasible, since the required number of likelihood evaluations scales exponentially with the number of dimensions. As a result, it is necessary to find some other way of exploring the parameter space to produce a reasonable approximation to the full likelihood. In the following sections, I will discuss two *Markov Chain Monte Carlo* methods that aim to do this in a computationally-efficient manner.

1.4.2 Metropolis-Hastings algorithm

A *Markov chain* is a discrete-time stochastic process for which the probability of moving to the next state of the system depends only on the current state. Markov chains can be constructed to explore a parameter space in such a way that the distribution of states visited by the chain asymptotically approaches a target probability distribution. Markov Chain Monte Carlo (MCMC) methods are concerned with constructing Markov chains to draw samples from complicated distributions using only simple rules. Amongst other things, they provide a way of approximating the likelihood function over a complex, high-dimensional parameter space with comparatively few evaluations of the likelihood.

MCMC methods are a commonly-used tool within the cosmological community. A number of public MCMC codes exist which implement likelihood functions capable of comparing variations on the standard cosmological model with datasets such as the CMB power spectrum, Type Ia supernova lightcurves, and the products of surveys of large-scale structure. These codes are often modified to take into account new datasets and new theoretical additions to the cosmological model. A popular code is the CosmoMC package [Lewis & Bridle, 2002].

One of the simplest MCMC methods is the Metropolis-Hastings algorithm. The next step in the chain, $\boldsymbol{\theta}'$, is determined by drawing a set of new parameters from a *proposal distribution*, Q, centred on the current location in parameter space, $\boldsymbol{\theta}$. The likelihood is evaluated at the new location, and if it is higher than the likelihood at the current location, the new location is accepted and the chain moves there. If the likelihood is lower, the chain may still move to the new location, but only with some probability that is a function of the change in likelihood. If the move is rejected, the chain stays at the current location and simply draws again from the proposal distribution.

The proposal distribution is generally taken to be symmetric, such that $Q(\boldsymbol{\theta}, \boldsymbol{\theta}') = Q(\boldsymbol{\theta}', \boldsymbol{\theta})$. While not strictly necessary, this condition is sufficient for the Markov chain's equilibrium distribution (the distribution that it would follow after infinite time) to approach the target probability distribution. The proposal distribution should be chosen to give a reasonable approximation to the target distribution, to the extent that its form is already known. In practice, this means that Q is often chosen to be a multivariate Gaussian centred on the current location, $\boldsymbol{\theta}$. In this case, the covariance matrix for Q determines how far the chain is likely to jump in parameter space at each step.

I will now state the Metropolis-Hastings algorithm. First of all, a method for calculating the likelihood of a model given data must be specified. Examples of likelihood functions were given in the previous section. A covariance matrix (or otherwise) for the proposal distribution and prior distributions for all of the parameters must also be chosen. The algorithm then proceeds as follows:

1. Draw an initial set of parameters $\boldsymbol{\theta}$ from their prior distributions and calculate the likelihood $\mathcal{L}(\boldsymbol{\theta})$.
2. Draw a new set of parameters $\boldsymbol{\theta}'$ from the proposal distribution Q centred on the current location, $\boldsymbol{\theta}$, and calculate the likelihood, $\mathcal{L}(\boldsymbol{\theta}')$.
3. Draw from the Uniform distribution, $u \sim U[0, 1]$.
4. Compare the likelihoods:
    - If $\mathcal{L}(\boldsymbol{\theta}')/\mathcal{L}(\boldsymbol{\theta}) \geq u$, accept the proposed step and update $\boldsymbol{\theta} \rightarrow \boldsymbol{\theta}'$.
    - If $\mathcal{L}(\boldsymbol{\theta}')/\mathcal{L}(\boldsymbol{\theta}) < u$, reject the proposed step (do not update $\boldsymbol{\theta}$).
5. Return to (2). Repeat until enough samples have been drawn.

The algorithm accepts all steps where the likelihood increases ($\mathcal{L}(\boldsymbol{\theta}') > \mathcal{L}(\boldsymbol{\theta})$), but only accepts steps where the likelihood decreases with some probability. This ensures that the algorithm will spend most of its time in high-likelihood regions, but won't get stuck in them permanently, giving it the chance to explore slightly less probable regions too.

The Metropolis-Hastings algorithm is a powerful general purpose method, but requires a considerable degree of tuning and additional processing of samples to produce good results. Some common issues with the Metropolis-Hastings algorithm are summarised below:

Convergence and Burn-in The chain starts at an arbitrary location in parameter space, potentially far from where the likelihood peaks. It can take a while for the chain to make its way to a high likelihood region. In the mean-time, it will be producing samples with comparatively low likelihood, which are not representative of the target distribution. The time taken for the chain to *converge* (i.e. to start sampling from the true target distribution) is called the *mixing time*. The samples produced before the chain has converged are called *burn-in*, and are often discarded.

It can be difficult to tell whether a chain has converged, or whether it is stuck in a local minimum (for example). A number of convergence tests have been proposed in the literature (see Cowles & Carlin [1996] for a review), although these should be used more as a guide than as rigorous indicators of convergence.

Sub-optimal acceptance rate The *acceptance rate* is the fraction of proposed steps that are accepted. If this is too low, the algorithm is having to evaluate a large number of likelihoods to produce each sample, which is computationally inefficient. If the acceptance rate is very high, the chain is likely proposing new sets of parameters that are too close to the old ones, and so it will explore the posterior slowly.

Sub-optimal acceptance rates are normally the result of a poor choice of proposal distribution. For example, if the proposal distribution is too broad, the chain will try to take big steps in parameter space, leading to large changes in likelihood that are unlikely to be accepted. Failing to account for parameter degeneracies can also cause poor acceptance rates, as the proposed steps will only be aligned with the direction of the degeneracy relatively infrequently.

Correlated samples Each sample drawn from the posterior distribution should ideally be completely uncorrelated with the previous sample. Because of the way the Metropolis-Hastings algorithm explores the posterior in discrete steps, however, some correlation between samples will arise. The degree of correlation can be estimated by plotting the *autocorrelation function* of the chain.

One way of dealing with correlated samples is to *trim* the chain, by removing every other sample, for example. Another way is to set multiple chains running in parallel and then mix the samples from all of the chains together afterwards.

Multimodality and non-Gaussianity Complex, non-Gaussian distributions can present a challenge for the simple Metropolis-Hastings approach. If the posterior is multimodal (i.e. it has more than one region of high probability), the chain may get stuck in one region without ever exploring the others, thus failing to converge to the target distribution. In this case, a more sophisticated MCMC method should be used (e.g. a Metropolis-Hastings algorithm that alternates between two proposal distributions, one of which is very broad so as to allow large jumps between modes).

1.4.3 Gibbs sampling

As highlighted in the previous section, care must be taken to correctly apply the Metropolis-Hastings algorithm to a given problem. There are numerous alternative methods available that generally offer better performance with respect to one or more of the issues mentioned above (e.g. slice sampling; rejection sampling; importance sampling; see MacKay [2003]), but none of them are guaranteed to work well in the general case.

One particularly robust method is *Gibbs sampling*. This estimates the joint posterior distribution for all parameters, $P(\{\theta_1, \ldots, \theta_N\}|D)$, by sequentially sampling from the conditional distributions, $P(\theta_i|\{\theta_1, \ldots, \theta_{i-1}, \theta_{i+1}, \ldots, \theta_N\}, D)$. It requires that calculation of the conditional distributions is tractable, and (ideally) that they are easy to sample from. In many applications, this is the case for the conditional distributions of at least most of the parameters. There are no issues with acceptance rate or tuning of the proposal distribution, since the algorithm draws from a known distribution, and thus always accepts each step.

An application of Gibbs sampling to CMB component separation is discussed in detail in Chapter 5. The algorithm and its mathematical validation are discussed in MacKay [2003].

Chapter 2

Measures of cosmic acceleration

In this chapter, I will attempt to clarify what is meant by acceleration in an inhomogeneous universe, and to study how different types of acceleration can arise within the context of relativistic cosmology. The existence of new matter fields or modifications to the theory of gravity will not be considered here, but I will allow for the Universe to be strongly inhomogeneous below a certain scale.

In what follows, I find that observations made over large distances (e.g. using supernova and CMB observations) are best fit with models that use non-local averages of geometric quantities. The acceleration that one can infer from these large-scale probes of cosmology is not necessarily similar to any locally-defined measures of acceleration, and does not necessarily imply that the expansion of space itself is accelerating at any point. This is a direct demonstration of back-reaction, of the type that was discussed in Section 1.2.4.

2.1 Measures of acceleration

Following Hirata & Seljak [2005] and Clarkson & Umeh [2011], I will consider multiple different measures of acceleration:

(a). The local acceleration of nearby observers in a small volume of space, as governed by the Raychaudhuri equation (Eq. 1.27);

(b). The acceleration inferred by fitting an FLRW distance-redshift relation to Hubble diagrams constructed from observations made over large distances;

(c). The acceleration inferred by constructing a Hubble diagram from local observations (i.e. at $z \simeq 0$), as described by Kristian & Sachs [1966];

(d). The average acceleration of a large volume of space, as calculated using Buchert's scalar averaging procedure [Buchert & Räsänen, 2012].

For an exactly homogeneous and isotropic FLRW model, all of these measures are identical. In the general case, however, they can be quite different, to the point that some of them can show strong acceleration, while others show deceleration.

Measures (a) and (c) are purely local, and depend only on the curvature of spacetime within the neighbourhood of a point (in the limit of geometric optics). Measures (b) and (d), however, are both inherently non-local in nature. Measure (a) describes the actual, dynamical acceleration of a volume of space, while measure (b) corresponds to what is measured in, for example, supernova surveys. Measure (c) is a local measure of acceleration, based on inferences made using the luminosity distance-redshift relation within a very small region of spacetime. Measure (d) corresponds to the theoretical procedure of fitting a smooth effective model to the real, inhomogeneous Universe.

Each measure has associated with it a *deceleration parameter*. For each definition, I will now set out its theoretical basis and physical interpretation, list the conditions necessary for acceleration to occur, and describe the relation of the deceleration parameter associated with the measure to observable quantities. The measures are summarised in Table 2.1, at the end of the section.

2.1.1 Local volume acceleration

By analogy with the deceleration parameter in an FLRW spacetime, one can define a local volume deceleration parameter in terms of the kinematical scalars introduced in Section 1.2.2,

$$q_\Theta = -1 - 3\frac{\dot{\Theta}}{\Theta^2} = \frac{3}{\Theta^2}\left[\frac{1}{2}(\rho + 3p) - \Lambda + 2\sigma^2\right], \tag{2.1}$$

corresponding to the monopole of the deceleration of the expansion rate of a set of neighbouring particles following worldlines u^a. This measure is said to be accelerating when $q_\Theta < 0$, which from Eq. 2.1 can be seen to occur if and only if $p < -\frac{1}{3}\rho$ or $\Lambda > 0$.

Now, q_Θ is a local measure of acceleration, defined only in the neighbourhood of a point in spacetime. Determining q_Θ from observations therefore requires Θ (and its first derivative) to be determined using observations within the neighbourhood of a single point in spacetime only. These observations need to be of the rate of change of proper distance between particles in their own rest-frame, which is not necessarily the same as the angular diameter distance or luminosity distance (for these see measure (c), below). The Universe is extremely inhomogeneous on small scales, and so this measure of acceleration is likely to display considerable spatial variation. A single local measurement of q_Θ need not, then, be particularly close to the mean value of the local volume acceleration.

2.1.2 Observed acceleration (from Hubble diagram)

To date, the strongest observational evidence for an accelerating universe comes from the distance-redshift relation, which is measured using "standardisable candles" such as Type Ia supernovae, as well as the CMB. By fitting these data to the FLRW distance-redshift relations given in Section 1.3.4, one finds that models with $\Omega_\Lambda > 0$ are strongly favoured, while those with $\Omega_\Lambda = 0$ are ruled out to a high degree of confidence. Under the assumption that spacetime is well-described by FLRW, this constitutes strong evidence for accelerating expansion.

A series expansion in the angular diameter distance about $z = 0$ gives Eq.

1.55, involving quantities such as the deceleration parameter, q_0. The value of q_0 can be found in a purely observational manner by taking derivatives of the fitted distance-redshift relation [Visser, 2004],

$$q_0 = - \left. \frac{d''_A}{d'_A} \right|_0 - 3, \tag{2.2}$$

where primes denote derivatives with respect to redshift, and where subscript 0 denotes that the quantity is evaluated at the observer. Note that this measure of deceleration is inferred from observations over large distances, and so assigns information to a point in spacetime based on information obtained from the entire extended region over which observations have been made. This is a highly non-local process.

Eq. 2.2 is derived from the distance-redshift relation in FLRW geometry, but one should note that the existence of such a geometry is not required in order to infer q_0 from observations. The relation given by Eq. 2.2 should simply be seen as defining a fitting procedure, and is an observable in *any* spacetime (after averaging over the celestial sphere). As such, anyone can measure q_0 if they are willing to interpret their observations within the framework of an FLRW model, regardless of the spacetime they actually inhabit. In what follows, I will call the acceleration inferred by fitting FLRW relations to the distance-redshift relation the *observed acceleration*.

This procedure can be repeated for every direction on the sky, and an FLRW model can be fitted to the monopole of the resulting angular distribution. The best-fit model can then be used to find q_0. The result of this procedure in a general spacetime is denoted by q_{obs}.

This definition of acceleration corresponds most closely to the one used by observers. It is a non-local measure, since it depends on solutions to the Sachs equations, which describe bundles of null geodesic curves that extend throughout the spacetime (see Section 1.3.3). In effect, the measurement of q_{obs} depends on finding the entire past null cone of an observer out to some z, and fitting some distance-redshift relation to it. The conditions for a spacetime to have $q_{\rm obs} < 0$ are therefore complicated in general. As I will show below, it is possible to find spacetimes that are quite different from simple Λ-dominated FLRW models that nevertheless have an apparent acceleration, $q_{\rm obs} < 0$.

2.1.3 Acceleration from local observations (using the Kristian-Sachs formalism)

The measure of acceleration that I just described has the disadvantage of requiring full solutions to the Sachs equations to be found as a function of redshift and angle on the observer's sky (see Section 1.3.3). This can be a difficult task in general, as it requires detailed knowledge of the geometry of spacetime. Instead, one can use the Kristian-Sachs formalism [Kristian & Sachs, 1966] to obtain a fully general and covariant series expansion of the distance-redshift relation about an observer without needing to consider solutions to the geodesic equations at all. Furthermore, the expansion can be decomposed directly into covariant spherical harmonics about the observer, allowing the monopole term to be calculated straight away [Clarkson & Umeh, 2011].

This procedure has been spelled out in detail by Clarkson & Umeh [2011]. The generalised form of Eq. 1.55 is

$$d_A = \frac{z}{[K^a K^b \nabla_a u_b]_0} \left(1 - \left[\frac{K^a K^b K^c \nabla_a \nabla_b u_c}{2(K^d K^e \nabla_d u_e)^2} \right]_0 z + \mathcal{O}(z^2) \right), \tag{2.3}$$

where the past-pointing null direction can be written in terms of the tangent vector to a comoving observer's world-line, u^a, and a direction on their sky, e^a,

$$K^a = \frac{k^a}{[u_b k^b]_0} = -u^a + e^a. \tag{2.4}$$

The subscript 0 again denotes evaluation at the observer's location. The terms in Eq. 2.3 can be expanded using a covariant decomposition in spherical harmonics. In order to facilitate this expansion, it is useful to invert Eq. 2.3 to give

$$z = [K^a K^b \nabla_a u_b]_0 d_A + \frac{1}{2}[K^a K^b K^c \nabla_a \nabla_b u_c]_0 d_A^2 + \mathcal{O}(d_A^3). \tag{2.5}$$

All of the terms that we wish to expand are now in the numerator. Comparing the monopoles of the coefficients in Eq. 2.5 with the corresponding FLRW relation then gives (with $8\pi G = 1$)

$$q_{\mathrm{KS}} = \frac{3}{\Theta^2}\left[\frac{1}{2}(\rho + 3p) - \Lambda + 6\sigma^2\right]_0 , \tag{2.6}$$

where I have used $H_0 = \frac{1}{3}\Theta$, which corresponds to the monopole of this term rather than its full spherical harmonic expansion. This matches most closely with the way that H_0 is typically used in observational studies; the monopole of H_0 tends to be determined separately from other quantities. From Eq. 2.6, it can be seen that $q_{\mathrm{KS}} \geq 0$ unless $p < -\frac{1}{3}\rho$ or $\Lambda > 0$. That is, acceleration of this measure can only occur if there is a cosmological constant, or if an exotic fluid with negative pressure is present.

There is clearly some similarity between the deceleration parameter of the local volume, q_Θ, and that which is obtained from the local distance-redshift relation, q_{KS}. Both measures of acceleration are local (depending only on quantities defined within the neighbourhood of the observer), and both are given by expressions that differ only by a term involving the shear scalar. This does not, however, mean that these two measures of acceleration are the same. They correspond to different physical quantities.

The relation between the Kristian-Sachs and observational acceleration measures is less clear. This has to do with the non-locality of the latter; if the Hubble diagram could be measured precisely at $z = 0$ (i.e. in the limit of geodesics of zero affine length), one would find $q_{\mathrm{obs}} = q_{\mathrm{KS}}$. But, because real observations necessarily cover a range of redshifts, the process of fitting a curve to the data and extrapolating that back to $z = 0$ means that in general one has $q_{\mathrm{obs}} \neq q_{\mathrm{KS}}$. This phenomenon has been investigated using observational data in Clifton *et al.* [2008]. As I will show shortly, even the signs of q_{obs} and q_{KS} can be different. That is, a locally-decelerating spacetime can still have a Hubble diagram that implies acceleration.

2.1.4 Acceleration of the average (Buchert's formalism)

In Section 1.2.5, I outlined Buchert's method of constructing a homogeneous and isotropic 'effective' model from an inhomogeneous spacetime by taking averages of scalar geometrical quantities over spacelike hypersurfaces. The hope is that the behaviour of the averaged model will capture some aspects of the real spacetime, both in terms of its dynamics and the observational quantities that are calculated within it.

By analogy with the FLRW result, I define a deceleration parameter for the averaged hypersurfaces as

$$q_{\mathcal{D}} = -\frac{1}{H_{\mathcal{D}}^2}\frac{\ddot{a}_{\mathcal{D}}}{a_{\mathcal{D}}}. \tag{2.7}$$

An effective distance-redshift relation can also be found for the averaged model by assuming that light rays follow null geodesics of the averaged spacetime, and that geodesic observers are comoving in the averaged geometry.

In general, the deceleration parameter $q_{\mathcal{D}}$ is non-local, and not directly observable, as it depends on averages over extended spacelike hypersurfaces. From Eq. 1.41, one can see that if the averaged spatial Ricci curvature, $\langle {}^{(3)}\mathcal{R} \rangle$, and backreaction, $Q_{\mathcal{D}}$, behave in a certain way, then it is possible to have $q_{\mathcal{D}} < 0$ without having $\Lambda > 0$ or $\langle p \rangle < 0$. In particular, spacetimes consisting of collapsing regions in an expanding background can exhibit this behaviour, which has led some to claim that the apparent cosmic acceleration inferred from supernova observations could instead be explained as a consequence of the variance of the inhomogeneous expansion rate that enters into the definition of $Q_{\mathcal{D}}$ (see Section 1.2.4 for further discussion). I will examine this claim in detail later in the chapter, but for now I will just note that it is possible for the Buchert averaged model to accelerate, even if $q_{\Theta} > 0$ everywhere.

Measure	**Local**	**Support**	**Observable**
Local volume, q_{Θ}	Yes	Spacetime point	In principle
Observational, q_{obs}	No	Null geodesics	Yes
Kristian-Sachs, q_{KS}	Yes	Spacetime point	In principle
Buchert average, $q_{\mathcal{D}}$	No	Spatial domain	No

Table 2.1: Summary of the measures of acceleration defined in Section 2.1.

The quantities of particular interest are the deceleration parameters that observers in a given region of spacetime should *expect* to infer, rather than the actual values of these parameters at single points (which may not be representative). To this end, I will also use Buchert's formalism to average the various measures of acceleration, using Eq. 1.38. For example, $\langle q_{\text{KS}} \rangle$ will be taken to correspond to the value of the Kristian-Sachs deceleration parameter that a typical observer would expect to measure in a given region. Unless specified otherwise, the averaging domain is taken to be larger than the homogeneity scale of the model[1].

2.2 Inhomogeneous cosmological models

I will now examine a number of different relativistic models, and demonstrate how the measures of acceleration defined in Section 2.1 can be calculated in each of them. Only cases with vanishing cosmological constant will be considered, as a non-zero Λ generically results in accelerating expansion in all of the measures discussed above. The models I consider are chosen as illustrative examples,

---

[1] It should be noted that this averaging scheme is weighted by proper volume, and so the density of observers is implicitly assumed to be weighted in a similar manner. Of course, this need not be the case, and other ways of distributing observers throughout space could be considered. This would affect what a 'typical' observer should expect to see.

as they are capable of showing acceleration in some measures, while displaying deceleration in others.

2.2.1 Spherical collapse model

In this section I will consider the spherical collapse model, which consists of an ensemble of disjoint FLRW regions [Gunn & Gott, 1972; Padmanabhan, 1993; Fosalba & Gaztañaga, 1998; Abramo *et al.*, 2009]. It is not a globally exact solution to Einstein's equations (distinct FLRW models cannot satisfy the Darmois-Israel junction conditions on their shared boundary), but provides a useful toy model of collapsing structures in an otherwise expanding universe. By virtue of each individual region being homogeneous, spatial averages take a particularly simple form in spherical collapse models. A scalar quantity S may be averaged simply by taking the sum of its values in the different regions weighted by the proper 3-volume of each region, V, at a given time [Ishibashi & Wald, 2006; Räsänen, 2009c],

$$\langle S \rangle = \frac{\sum_i S_i V_i}{\sum_i V_i}. \tag{2.8}$$

A configuration consisting of collapsing structures in an expanding background is known to lead to acceleration of the Buchert averaged spacetime, $q_{\mathfrak{D}} < 0$ [Ishibashi & Wald, 2006; Räsänen, 2009c]. In order to reproduce this, the model I am using here is constructed from alternating regions of collapsing, spatially closed and dust-dominated regions, and expanding, spatially open vacuum regions, as illustrated in Fig. 2.1. The regions are modelled using FLRW geometry (with $\Lambda = 0$), and will be referred to as Regions I and II, respectively. The collapsing regions are chosen so that they have a comoving size of order 10% of the vacuum regions at the present time. As one looks further back in time, the collapsing regions increasingly dominate the proper spatial volume.

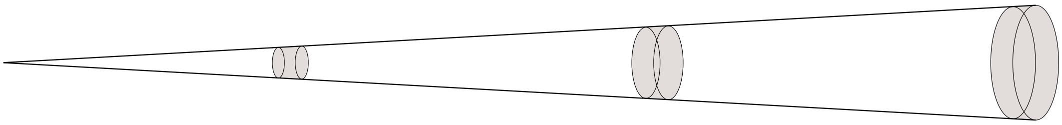

Figure 2.1: Schematic representation of a line-of-sight through a universe with alternating expanding vacuum regions (clear), and collapsing dust regions (grey).

In what follows, I will use the following form for the FLRW metric,

$$ds^2 = -dt^2 + \frac{a^2\left(dX^2 + dY^2 + dZ^2\right)}{[1 + \frac{k}{4}(X^2 + Y^2 + Z^2)]^2}, \tag{2.9}$$

and individual domains will be taken to have coordinate length $X_{\mathcal{D}}$ along the line of sight. The proper volume of each domain is

$$V_i = \int_{\mathcal{D}_i} \frac{a_i^3 dX dY dZ}{[1 + (k_i/4)(X^2 + Y^2 + Z^2)]^3}, \tag{2.10}$$

and the comoving depth of a domain is

$$\chi_i = \int_0^{X_{\mathcal{D}_i}} \frac{dX}{1 + (k_i/4)(X^2 + Y^2 + Z^2)}. \tag{2.11}$$

The effective scale factor, defined in Eq. 1.40, is

$$a_{\mathcal{D}}(t) = \left(\frac{\sum_i V_i(t)}{\sum_i V_i(t_0)}\right)^{\frac{1}{3}}, \tag{2.12}$$

and the Buchert average deceleration parameter $q_{\mathcal{D}}$ is calculated using Eq. 2.7.

The distance-redshift relation is needed in order to calculate q_{obs}. It can be found by solving the Sachs optical equations for a ray passing through a number of different FLRW regions. All that is required is to ensure continuity of the affine parameter, λ, the redshift, z, the angular diameter distance, d_A, and the null expansion scalar, θ, at the boundary, as a ray leaves one region and enters another. These conditions impose no restrictions on the individual FLRW regions – their size, matter content, and expansion rate can be chosen separately. I do choose the cosmic time in individual regions such that it is continuous on the boundary between them, however.

The Sachs equations in each region reduce to

$$\frac{d^2(d_A)}{d\lambda^2} = -4\pi G\rho_i \, (1+z)^2 d_A, \tag{2.13}$$

with 4-vector tangent to the null curves given by

$$k^a = \left(1+z, \pm\frac{1+z}{a_i}\sqrt{1+\frac{1}{4}k_i X^2}, 0, 0\right). \tag{2.14}$$

The redshift as a function of affine distance is then

$$\frac{dz}{d\lambda} = -H_i(1+z)^2. \tag{2.15}$$

The relation $1+z = a^{-1}$ has not been used, as the total redshift along a ray, $z(\lambda)$, is not the same as the redshift that one would obtain by ray-tracing through a single FLRW region.

The light rays are propagated through each region in turn, until the edge of the region is reached at some coordinate distance X_i (which I call the 'length' of the region here). This length is a function of time (evaluated at the instant the ray enters a region), chosen so that the ray travels a proper distance in each region proportional to the fraction of the proper volume taken up by that region on a surface of constant t, i.e.

$$\frac{a_I \chi_I}{a_{II}\chi_{II}} = \frac{V_I}{V_{II}}. \tag{2.16}$$

This choice takes into account not only the different expansion rates of the two different regions along the line of sight, but also the fact that as one goes forwards in time, the number density of dust regions should be expected to decrease. For simplicity, I fix the (comoving) length of the collapsing region, χ_I, and then solve

Eq. 2.16 for χ_{II} on entering each new region.

The redshift through the model is given by integrating Eq. 2.15. There is a blueshift as the photons pass through collapsing regions, and a redshift as they pass through expanding regions. The angular diameter distance increases despite the blueshift, and the distance-redshift relation becomes multi-valued. This leads to it taking on a jagged appearance, although the distance remains smooth as a function of affine parameter. The observational deceleration parameter can be calculated by fitting an FLRW model with dust, curvature, and Λ to the jagged distance-redshift curve using a simple least-squares procedure. The FLRW deceleration parameter, defined by Eq. 2.2, can then be calculated to give q_{obs}.

The local volume deceleration parameter in each FLRW region is given by Eq. 2.1. In my chosen spherical collapse model, $\Omega_\Lambda = 0$ in both types of region, and $\Omega_m = 0$ in the vacuum regions, so the average of the local deceleration parameter reduces to

$$\langle q_\Theta \rangle = \frac{1}{2} \frac{\Omega_{m,I} V_I}{V_I + V_{II}} \bigg|_0 , \tag{2.17}$$

which is positive definite (i.e. decelerating everywhere). The equality $q_\Theta = q_{\text{KS}}$ holds, since each region is FLRW, and therefore has vanishing shear.

2.2.2 Kasner-EdS model

In the previous section I considered the spherical collapse model, which consists of disjoint regions of different FLRW spacetimes. This model is simple to work with, but only forms an approximate global solution of Einstein's equations. In this section I consider an exact solution that is inhomogeneous along the line of sight, with alternating regions of collapsing dust and expanding vacuum, as illustrated in Figure 2.1. The two spacelike directions orthogonal to the line of sight span a planar-symmetric subspace, and statistical homogeneity is enforced in the line of sight direction only.

In order to prevent the rapid formation of singularities that often occurs when dust is allowed to collapse in general relativistic models, I take the dust-dominated regions to be locally spatially homogeneous and isotropic. These symmetries prevent the sudden formation of singularities at different points in space, as every point is taken to be identical to every other point by fiat. The geometry of these regions is therefore given by the FLRW line-element 2.9, where $a(t)$ is the scale factor that obeys the Friedmann equation (Eq. 1.9, for matter and curvature only). In the vacuum regions, the geometry is taken to exhibit translational symmetry along the line of sight, but is not restricted to be FLRW, as it is known that no solutions that satisfy the junction conditions will exist in this case. The geometry of this region is then given by

$$ds^2 = -d\hat{t}^2 + b_1^2(\hat{t}) d\hat{X}^2 + b_2^2(\hat{t}) \left(d\hat{Y}^2 + d\hat{Z}^2 \right), \tag{2.18}$$

where $b_1(\hat{t})$ and $b_2(\hat{t})$ are the scale factors in the directions tangent and normal to the line of sight, respectively.

It can be shown that the junction conditions between these two regions are satisfied if the hatted and unhatted coordinates are identified with one another at the boundary, and if $k = 0$, $b_1 = a^{-1/2}$ and $b_2 = a$ [Lake, 1992; Dyer & Oliwa, 2001]. The dust-dominated regions are then spatially-flat FLRW, the vacuum regions are Kasner, and the entire geometry is an exact solution of Einstein's equations [Landry & Dyer, 1997]. These solutions are, in fact, a special case of the general dust solution admitting a three-dimensional group of spacelike Killing vectors on two-dimensional planar subspaces [Stephani *et al.*, 2003; Di Dio *et al.*, 2012], but are chosen such that one can have collapsing regions that do not exhibit the shell-crossing singularities that tend to rapidly form in the general case. It is possible to arrange for either the dust regions to be collapsing and the vacuum regions to be expanding along the line of sight, or the dust regions to be expanding and the vacuum regions to be collapsing along the line of sight. Here

I will concentrate on the former, which is more in-keeping with the usual picture of what is expected to happen in the late Universe (voids expanding, and dense regions collapsing).

In order to calculate observational quantities within this solution along the chosen line of sight, a set of observers must be specified. In the dust-dominated regions these can be conveniently chosen to be comoving with the fluid, such that they follow a set of geodesic curves with tangent vector $u^a = (1, 0, 0, 0)$. In the vacuum regions, I also take observers to follow curves with tangent vector $u^a = (1, 0, 0, 0)$ in the coordinates used in Eq. 2.18. Note that although there is no fluid in this case, so that this choice is not unique, it is a choice that picks out a set of geodesic curves that are parallel to the world-lines of observers who stay at the boundary between regions. These choices therefore correspond to a congruence of complete geodesic curves that fill the entire spacetime.

As before, I will refer to the dust-dominated regions as Region I and the vacuum regions as Region II. Null geodesic curves in these two regions, in the direction of the inhomogeneity, are given by

$$\begin{aligned} k^a_I &= \frac{c_1}{a^2}\,(a, -1, 0, 0) && (2.19)\\ k^a_{II} &= c_2\left(\sqrt{a}, -a, 0, 0\right), && (2.20) \end{aligned}$$

where c_1 and c_2 are constants, and where the affine parameter that defines these tangents has been taken to decrease into the past. The energy of a photon following k^a, as measured by the observers following the curves u^a, is given by

$$\begin{aligned} E_I &= \frac{c_1}{a} && (2.21)\\ E_{II} &= c_2 a^{1/2}, && (2.22) \end{aligned}$$

where $E = -u_a k^a$. The Sachs optical equations in the two regions reduce to

$$\frac{d^2 d_{A,I}}{d\lambda^2} = -\frac{2c_1^2}{3a^5} d_{A,I} \tag{2.23}$$

$$\frac{d^2 d_{A,II}}{d\lambda^2} = 0, \tag{2.24}$$

where c_1 is the constant from Eq. 2.19, which will be different within each individual dust-dominated region. As always, the redshift is given by taking the ratio of photon energy at the time of emission and observation, calculated using Eqs. 2.21 and 2.22.

The trajectories of photons can be straightforwardly integrated between the different regions, using Eqs. 2.19 and 2.20, and by taking the value of $\hat{X}(\hat{t})$ on leaving one region as its initial value on entering the next. Likewise, the value of E can be calculated along the null trajectories by setting its value on entering one region as being equal to its value on leaving the last. This gives the value of the constants c_1 and c_2 in each of the dust and vacuum regions respectively, and allows Eqs. 2.23 and 2.24 to be integrated along the null trajectory. Integration of this equation again requires setting d_A and θ to be continuous at the boundaries between regions. Following the prescription above, the model is uniquely specified once three pieces of information are given: (i) The comoving size of the vacuum regions, (ii) the comoving size of the dust regions, and (iii) the time until the dust regions collapse to zero thickness (the 'big crunch').

Now consider the Buchert average of this geometry. The usual procedure is to average the expansion scalar over a spacelike hypersurface and use the averaged value to calculate observables. The model that has been created here is inhomogeneous in one direction only, however, and so averaging in all three spatial directions should *not* be expected to reproduce anything like the observations that one would obtain by looking in the direction of the inhomogeneity. Instead, the most appropriate thing to do (by analogy with the case of inhomogeneity in all 3 spatial directions), is to average the scale factor in the direction of inhomogeneity only. This leaves an averaged geometry with line-element

$$ds^2 = -dt^2 + \langle b \rangle^2 \, dX^2 + a^2(t) \left(dY^2 + dZ^2 \right), \tag{2.25}$$

where the averaged scale factor is given by $\langle b \rangle = \int \sqrt{g_{XX}} dX / \int dX$. It is now possible to calculate observables in this averaged geometry and compare them to the observations made along the line of sight in the actual geometry of the spacetime.

Finally, consider the spatial average of the local volume deceleration parameter. Again, averaging over all spatial directions is not necessary, as I am only considering inhomogeneity and observations along one preferred direction. The average of q_Θ along the line of sight is therefore given by

$$\langle q_\Theta \rangle = \frac{\int q_\Theta \sqrt{g_{XX}} dX}{\int \sqrt{g_{XX}} dX}, \tag{2.26}$$

where q_Θ is $1/2$ in the collapsing dust regions, and -4 along the X-direction in the vacuum regions. A similar expression is found for q_{KS}, which takes the same value as q_Θ in both the dust and vacuum regions.

2.2.3 Lemaître-Tolman-Bondi model

In the previous two sections, I considered models consisting of alternating expanding vacuum and collapsing dust regions. I will now consider a model with no discontinuities in the density distribution, in the form of the spherically-symmetric, dust-only Lemaître–Tolman–Bondi (LTB) solutions that were described in Section 1.2.3. These have been the focus of much recent interest due to their ability, in the guise of 'giant void' models, to reproduce the observed supernova Hubble diagram without a cosmological constant [Célérier, 2000; Célérier *et al.*, 2010; Biswas *et al.*, 2010; Bolejko *et al.*, 2011a; Moss *et al.*, 2011; Nadathur & Sarkar, 2011; Bolejko *et al.*, 2011b]. They are also capable of having an accelerating spatial average under certain conditions [Räsänen, 2004a; Paranjape & Singh, 2006; Bolejko & Andersson, 2008; Sussman, 2011]. The density, expansion, and shear scalars for this spacetime were given in Section 1.2.3 (Eqs. 1.31–1.33) along with other details of its dynamical behaviour, so I will concentrate on its optical properties in this section.

Observers away from the centre of symmetry have anisotropic distance-redshift relations, in general. Rather than solving the Sachs equations in full for every direction on the sky, I will instead use the *dipole approximation*[1], which assumes that the dipole term dominates the anisotropy of the distance-redshift relation. The dipole is aligned with the radial direction due to the symmetry of the model, and so the monopole can be estimated by taking the mean of the angular diameter distance in the radial directions facing into and out from the centre of symmetry,

$$d_A(z)|_{\ell=0} \approx \frac{1}{2}[d_A(+\hat{r}, z) + d_A(-\hat{r}, z)]. \tag{2.27}$$

I expect this to be a reasonable approximation for the models considered here. The observational deceleration, $q_{\rm obs}$, is defined using the monopole of d_A only.

For light propagation purely in the radial direction, the tangent vector to the null geodesics is

$$k^a = \left((1+z), \pm\frac{\sqrt{1-kr^2}}{a_2}(1+z), 0, 0\right), \tag{2.28}$$

and the redshift is given by integrating

$$\frac{dz}{d\lambda} = -H_2(1+z)^2. \tag{2.29}$$

The angular diameter distance in either direction can be found using the Sachs

---

[1] See the end of Section 2.3.3, and Alnes & Amarzguioui [2006], for a discussion of the validity of this approximation.

equation (Eq. 1.47) in the radial direction; for an observer at the centre of symmetry, this becomes

$$\begin{aligned} d_A(z) &= r(z)\, a_1(r(z), t(z)); && (2.30) \\ 1+z &= \exp\left\{ \int_{t_e}^{t_o} H_2(t, r(t)) dt \right\}. && (2.31) \end{aligned}$$

In general, spatial averages in an LTB spacetime will be both position- and domain-dependent. In what follows, I will consider spatial averaging only for spherical domains centred at $r = 0$, on hypersurfaces of constant t. The effective scale factor is defined to be $a_{\mathcal{D}} = (V_{\mathcal{D}}/V_{\mathcal{D},0})^{\frac{1}{3}}$, where

$$V_{\mathcal{D}} = 4\pi \int_0^{r_{\mathcal{D}}} \frac{a_2 a_1^2 r^2}{\sqrt{1 - k(r) r^2}} dr \tag{2.32}$$

and $r_{\mathcal{D}}$ is the radius of the spherical domain. The average of a scalar quantity is then given by

$$\langle S \rangle = \frac{4\pi}{V_{\mathcal{D}}} \int_0^{r_{\mathcal{D}}} S(r, t) \frac{a_2 a_1^2 r^2}{\sqrt{1 - k(r) r^2}} dr. \tag{2.33}$$

I will only consider the class of LTB models with $\Lambda = 0$. This means that the spacetime is locally decelerating everywhere, $q_\Theta \geq 0$, and the Kristian-Sachs measure is also necessarily decelerating ($q_{\mathrm{KS}} \geq 0$). Nevertheless, the freedom in the LTB radial profiles makes it possible to construct models in which the Hubble diagram exactly matches that of an accelerating FLRW model for $z > 0$, as seen by an observer at the centre of symmetry [Mustapha *et al.*, 1997; Bolejko & Wyithe, 2009] (although see Romano [2010]).

Acceleration of the Buchert average, $q_{\mathcal{D}} < 0$, has been demonstrated for a number of different LTB models (e.g. Räsänen [2004a]; Paranjape & Singh [2006]; Kai *et al.* [2007]; Bolejko & Andersson [2008]; Chuang *et al.* [2008]). The cases studied generally take spherical averaging domains, centred about the origin, and typically find acceleration only for finite ranges of domain size, which do not correspond to the homogeneity scale (if one exists). Additionally, models in which observers at the centre of symmetry infer acceleration from their Hubble diagram seem not to correspond to those with an accelerating Buchert average [Bolejko & Andersson, 2008], and vice versa [Romano, 2007]. Since the spacetime is always decelerating locally, the existence of acceleration in the Buchert average must be caused purely by the backreaction term, Eq. 1.42.

In what follows, I will specialise to LTB models with a simple Gaussian spatial curvature profile

$$k(r) = A_k \exp\left(-\frac{r^2}{w_k^2}\right), \tag{2.34}$$

with t_B =constant, and with a choice of radial coordinate such that $m(r)$ =constant. When $A_k < 0$, there is a central void region (typically surrounded by an overdense shell), and an asymptotic flat FLRW region. These models are capable of producing good fits to the existing supernova data for an observer at the centre of symmetry.

2.3 Results

2.3.1 Spherical collapse

In this section, I evaluate the four chosen measures of acceleration in the spherical collapse model (as described in Section 2.2.1). This model is known to be able to have an accelerating Buchert average, despite locally decelerating everywhere [Ishibashi & Wald, 2006].

Figure 2.2 plots the magnitude of sources, μ, that an observer in the spherical collapse model would see, minus the magnitude a source at the same redshift would have in a pure vacuum model (with all of the dust regions removed). The model I used in this figure is one in which the vacuum regions are 80 Mpc wide at the present time, and dust regions are 15 Mpc wide. In what follows, I will refer to these plots as 'the Hubble diagram' (see also Section 1.3.4.1).

The results for two different observers are plotted: one at the centre of a collapsing dust region (red line), and one at the centre of an expanding vacuum region (blue line). The plot shows that the type of region that the observer finds themselves in can have a considerable impact on the behaviour of the Hubble diagram they construct at low z. At high z, however, the curves evolve almost identically (up to a vertical displacement). In both cases, the blueshifting that occurs in the collapsing region forces the curves upwards, due to the magnitude continuing to increase even while the redshift decreases. This leads to an overall positive gradient for the curves in Figure 2.2, while the gradient at any point on each individual curve is negative. This result is significant, as accelerating FLRW models would have positive gradient in these plots, while decelerating FLRW models have negative gradient, as noted in Section 1.3.4.1.

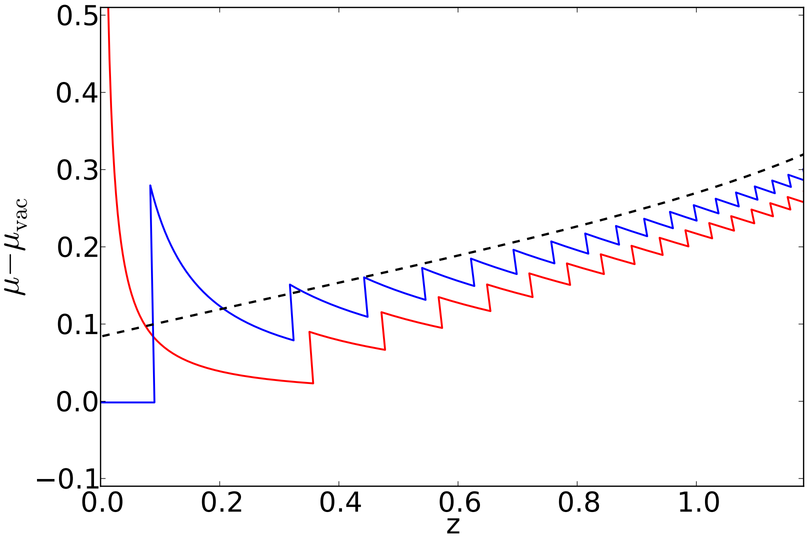

Figure 2.2: Magnitude of sources in the spherical collapse model, minus the magnitude they would have in pure vacuum. Observations made by a single observer, from the centre of the dust and vacuum regions, are displayed as solid red (lower at $z = 1$) and blue lines, respectively. The dashed black line is the same quantity in the Buchert averaged model.

Figure 2.3 plots the result of averaging the Hubble diagrams constructed by observers in both the dust and vacuum regions of the same model shown in Figure 2.2. I did this by constructing individual distance-redshift relations for a large number of observers (all in the same model), binning these relations in redshift, and then calculating the mean and standard deviation in each bin. I also calculated the magnitudes that would be found in the Buchert averaged model, and the spatially averaged deceleration parameter $q_\Theta = q_{\rm KS}$. The upper panel of Figure 2.3 plots the magnitude of sources, minus the magnitude they would have at the same redshift if all the dust regions were removed (as in Figure 2.2). The lower panel plots the magnitude of sources minus the magnitude they would have in the Buchert averaged model. In this figure, I have shifted the curves so that they coincide at $z = 0$. This corresponds to a change in the local Hubble rate.

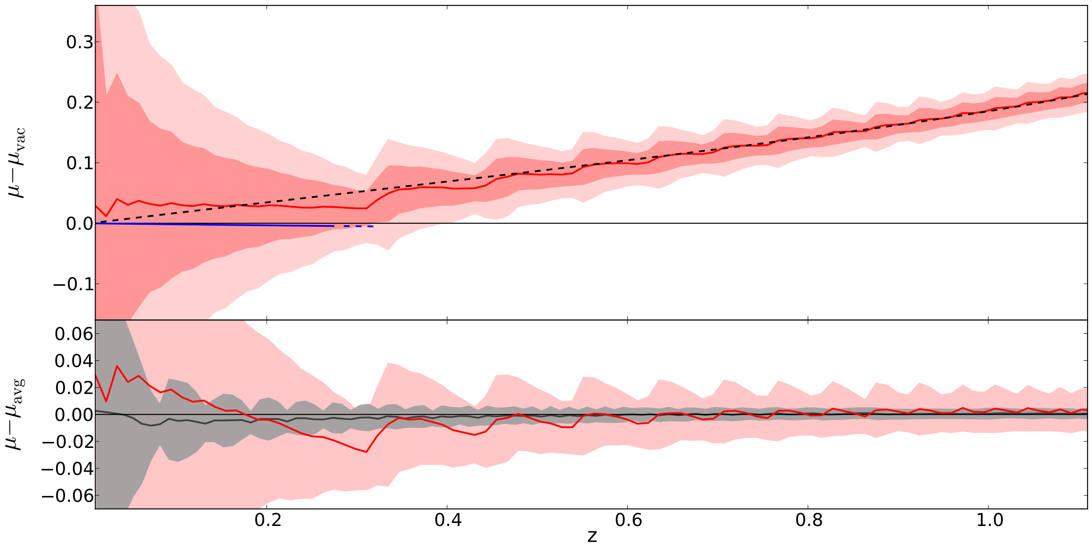

Figure 2.3: Upper Panel: Magnitude of sources in the spherical collapse model, minus the magnitude they would have in pure vacuum. The solid red line is the mean observed magnitude, obtained by spatially averaging distance-redshift relations on a surface of t =constant. The pink bands are 1σ and 2σ confidence regions. The black dashed line shows the corresponding quantity in the Buchert averaged model. The short blue line is the distance modulus for a FLRW model with deceleration parameter $q = \langle q_\Theta \rangle$. Lower Panel: A difference plot of the red line and dashed line, from the panel above. The solid black line corresponds to a model with regions that are a quarter of the size of those used in the upper panel. The pink (wide) and grey (narrow) bands are 1σ confidence regions for the two different models.

The upper panel of Figure 2.3 shows that the Buchert average (dashed black line) closely traces the mean observed magnitude (solid red line). The 1 and 2σ confidence regions appear to oscillate, because of the jaggedness of the individual distance-redshift curves that were averaged over (see Figure 2.2). Nevertheless, the curve for the Buchert average stays within the 1σ confidence region for the entire redshift range considered. Part of the reason for this is that the black line has been shifted vertically to match the red line at high z, in order to aid comparison. Without this shift, the two curves have the same zero-point, but fluctuations in the mean observational curve at low z cause an offset to build up at higher z. The zero-points are the same because they are governed by the same spatial average of the local Hubble rate $\langle H_0 \rangle$ (for the observational curve) and the Buchert average Hubble rate $H_{\mathcal{D}}$ (for the Buchert average curve). These are equal at $z = 0$.

The lower panel in Figure 2.3 shows that making the comoving size of the regions smaller, so that the initial region is less dominant, significantly reduces the fluctuations of the mean observational curve (in both cases, these fluctuations decrease as redshift increases). This in turn reduces the offset that develops between the observational curve and the Buchert average curve.

The short blue line in the upper panel of Figure 2.3 is the 'effective' curve obtained by setting $q_0 = \langle q_\Theta \rangle$ in the FLRW series expansion for $d_A(z)$. Again, $q_\Theta = q_{\rm KS}$ in the spherical collapse model, so this line is also the effective curve for the Kristian-Sachs deceleration parameter. It bears little resemblance to the observational and Buchert average curves here.

The values for the deceleration parameters measured in this model are

$$\langle q_\Theta \rangle \simeq 0.017 \tag{2.35}$$

$$q_{\mathcal{D}} \simeq -0.167, \tag{2.36}$$

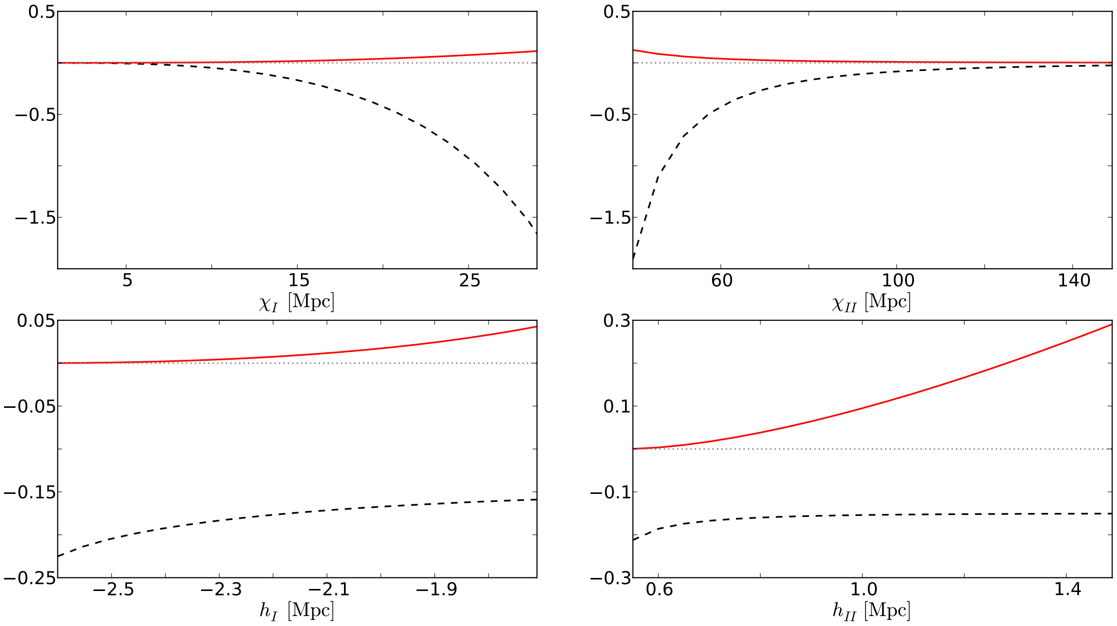

Figure 2.4: Dependence of the Buchert average deceleration parameter, $q_{\mathfrak{D}}$ (dashed black line), and spatially-averaged local volume deceleration parameter, $\langle q_\Theta \rangle$ (solid red line), on the parameters of the spherical collapse model. Shown is the dependence on the Hubble rates in the collapsing and vacuum regions, h_I and h_{II}, and the comoving region sizes, χ_I and χ_{II}.

with $\langle q_{\rm KS} \rangle = \langle q_\Theta \rangle$, and $\langle q_{\rm obs} \rangle \simeq q_{\mathfrak{D}}$. By considering other model parameters, I have confirmed that the curves due to averaging observations, and the Buchert average distance curve, always seem to show similar functional behaviour (and thus have similar deceleration parameters). Neither of these quantities are ever close to $\langle q_{\rm KS} \rangle$ or $\langle q_\Theta \rangle$, unless the dust regions are made to expand, or are made to be very small.

I find that the existence of acceleration in both the Buchert average and the observational distance-redshift relations is therefore a generic feature of spherical collapse models consisting of expanding and collapsing regions. Figure 2.4 shows the results of varying the parameters of the FLRW regions that constitute the model. The base model has the parameters $h_I = -2.0$ and $\Omega_{m,I} = 1.8$ in the dust regions, and $h_{II} = 0.7$ and $\Omega_{m,II} = 0$ in the vacuum regions. The comoving sizes of these regions are taken to be $\chi_I = 15$ Mpc and $\chi_{II} = 80$ Mpc, respectively.

The collapsing region is chosen to be 52% of its maximum age. The plots in Figure 2.4 are for models with these parameter values, apart from the parameter being varied. The figure shows a strong dependence of the Buchert average acceleration on region size – models with collapsing regions that are relatively larger have greater acceleration, as expected. Increasing the Hubble rate in the vacuum regions reduces the current age of the model, and correspondingly increases $\langle q_\Theta \rangle$. This is due to this quantity being evaluated at an earlier time, when the collapsing regions are more dominant. Figure 2.4 shows that the deceleration parameter of the Buchert averaged model is negative as long as the collapsing region takes up a non-negligible fraction of the comoving volume. If the vacuum region dominates, both the local volume and Buchert average deceleration parameters tend to zero. Since the observational deceleration parameter is well-approximated by the Buchert average measure, it seems that all that is required for observers to see an apparent acceleration is the existence of a non-negligible fraction of collapsing regions.

2.3.2 Kasner-EdS

I will now repeat the analysis of the previous section for the Kasner-EdS model. This is included in order to allay concerns that the coherence in the accelerations of the Buchert average and observational measures seen in the spherical collapse model were caused simply by some 'special' feature of the model, e.g. the fact that it is disjoint.

Figure 2.5 plots the magnitude of sources, μ, that an observer in the Kasner-EdS model would see, minus the magnitude a source at the same redshift would have in a pure vacuum model (with all of the dust regions removed). The model used in this figure again has dust regions that are 15 Mpc wide, but the vacuum regions are now $\sim$ 1500 Mpc across. This large number is required in order to get cosmologically interesting redshifts, because of the rapid acceleration in the

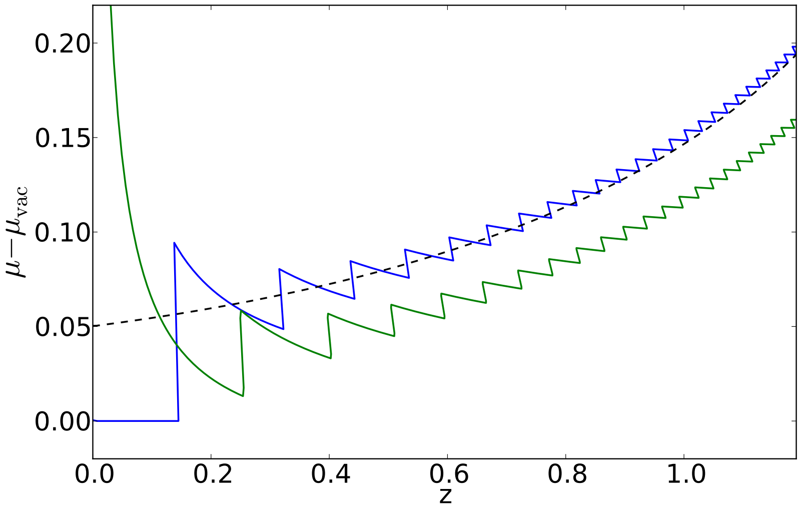

Figure 2.5: The same quantities that were plotted in Figure 2.2, but using the Kasner-EdS model.

vacuum regions along the preferred line of sight[1]. The model here is chosen such that the dust regions collapse to a singularity in ~ 5 billion years.

Two different observers are considered in Figure 2.5: one at the centre of a collapsing dust region (green line), and one at the centre of an expanding vacuum region (blue line). Again, it is apparent that the type of region that the observer finds themselves in can have a considerable impact on the behaviour of the Hubble diagram they construct at low z, while at high z the curves evolve almost identically (up to a vertical displacement). Blueshifting again occurs in the collapsing regions, forcing the curves upward.

Figure 2.6 plots the results of averaging the distance-redshift relations of observers in both the dust and vacuum regions of the same model considered in Figure 2.5, as was done in Figure 2.3 for the spherical collapse model. Magnitudes in the Buchert averaged model, and the spatially averaged deceleration parameter $q_{\Theta} = q_{\rm KS}$, have also been calculated. With this model, however, no vertical shift of the Buchert averaged model curve is required in order for it to agree

---

[1] It should be reiterated here that this model is not being proposed as a realistic representation of the actual Universe, but rather to provide a simple exact solution of Einstein's equations that allows the relativistic behaviour that may occur in more realistic solutions to be studied. In this sense, it should be considered as proof-of-concept only.

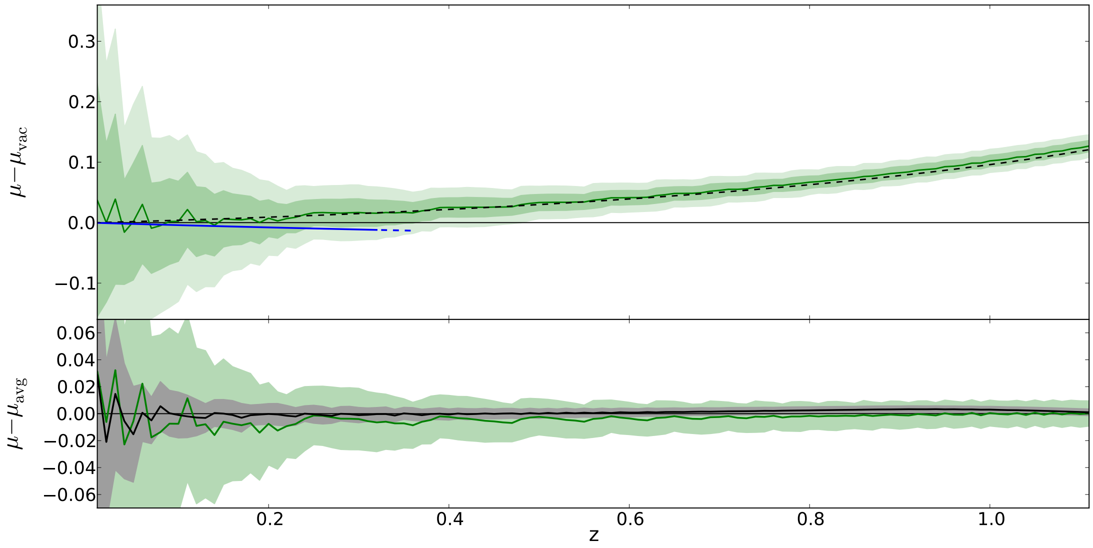

Figure 2.6: The same quantities that were plotted in Figure 2.3, but using the Kasner-EdS model.

well with the average of the observed magnitudes. The Buchert average closely traces the mean observed magnitudes. A vertical shift has been performed on all of the curves in Figure 2.6 simultaneously, however, so that they approach the origin at $z = 0$. Again, reducing the comoving size of the regions, so that the initial region is less dominant, significantly reduces the fluctuations of the mean observational curve.

The short blue line in the upper panel of Figure 2.6 is again the ‘effective’ distance modulus curve obtained by setting $q_0 = \langle q_\Theta \rangle$ in the FLRW series expansion for $d_A(z)$, and $q_\Theta = q_{\rm KS}$ too. The values for the deceleration parameters measured in this model are

$$\langle q_\Theta \rangle \simeq -3.96 \tag{2.37}$$

$$q_{\mathcal{D}} \simeq -7.18, \tag{2.38}$$

with $\langle q_{\rm KS} \rangle = \langle q_\Theta \rangle$, and $\langle q_{\rm obs} \rangle \simeq q_{\mathcal{D}}$. This value of $\langle q_\Theta \rangle$ corresponds to rapid acceleration, but not as rapid as simply looking through pure vacuum regions in the direction of inhomogeneity, where $q_0 = -4$. The value of $q_{\mathcal{D}}$, on the other hand, corresponds to considerably more acceleration than simply looking through the vacuum regions alone. As in the spherical collapse models, therefore, the presence of the collapsing dust regions causes a dramatic increase in both the acceleration of the Buchert averaged model, and the average of the observational acceleration.

By considering models with other parameter values, it has been confirmed that the curves due to averaging observations, and the Buchert average distance curve, always seem to show similar functional behaviour (and thus have similar deceleration parameters). Neither of these quantities are ever close to $\langle q_{\mathrm{KS}} \rangle$ or $\langle q_{\Theta} \rangle$, unless the dust regions are removed, or become vanishingly small.

2.3.3 LTB

The final model that I will consider is an LTB spacetime, with parameters chosen to produce a good fit to the supernova data for an observer at $r = 0$. These are displayed in Figure 2.7. Unlike the other models that I have considered, the LTB model has smooth density and Hubble rate profiles on spatial slices. There are, however, no collapsing regions at $t = t_0$.

Figure 2.8 displays the magnitudes of sources in the LTB model for the various acceleration measures. Since the chosen model has no homogeneity scale, I plot the distance modulus curves for two different averaging domain radii: $r_{\mathcal{D}} = 1000$ Mpc (well inside the void), and $r_{\mathcal{D}} = 3000$ Mpc (near the void boundary). The results in the two cases differ significantly, with the smaller averaging domain displaying acceleration for the mean observational curve (solid red line), while its counterpart for the larger domain (solid blue line) shows a strong deceleration. Note that the observational curves are for the *monopoles* of the distance-redshift relation, obtained using the dipole approximation described in Section 2.2.3. The curves for the Buchert average (dashed lines) do not match the mean observational

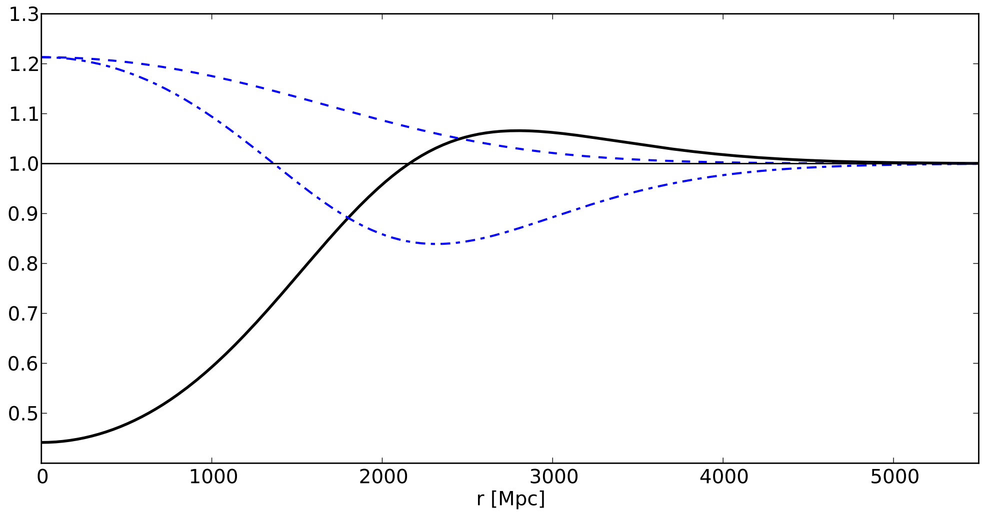

Figure 2.7: Density and expansion rates as a function of radius in an LTB void model. The model has spatial curvature of the form given in Eq. 2.34, with $A_k = -3.82 \times 10^{-8}\text{Mpc}^{-2}$ and $w_k = 1800$ Mpc. Shown are the density, ρ (solid black), transverse Hubble rate, H_1 (blue dashed), and radial Hubble rate, H_2 (blue dash-dot). All of the curves are normalised to their values in the asymptotically-homogeneous region ($\rho = 9.2 \times 10^{10}\text{M}_\odot\text{Mpc}^{-3}$, $H_1 = H_2 = 57.7$ kms^{-1}Mpc^{-1}).

curves (solid lines) in any significant way. In particular, both of the curves for the Buchert average are decelerating, while the averaged observed relation for the smaller domain size is accelerating.

The dotted and dash-dotted lines are ‘effective’ distance moduli for the local volume and Kristian-Sachs deceleration parameters. These correspond to series expansions of the FLRW $d_A(z)$ relation with deceleration parameters $q_0 = \langle q_\Theta \rangle$ and $q_0 = \langle q_{\text{KS}} \rangle$ respectively. Neither follows the Buchert average, nor the mean observational curves. They are closely related to one another though, with only a slight discrepancy apparent at higher redshift for the larger domain size. This is because the two measures only differ by a term proportional to the shear, which is relatively small in this case.

The upper set of observational curves in Figure 2.8 show that a substantial fraction of observers within a radius of $r \leq 1000$ Mpc will infer acceleration from the monopole of their Hubble diagram, despite all of the other deceleration pa-

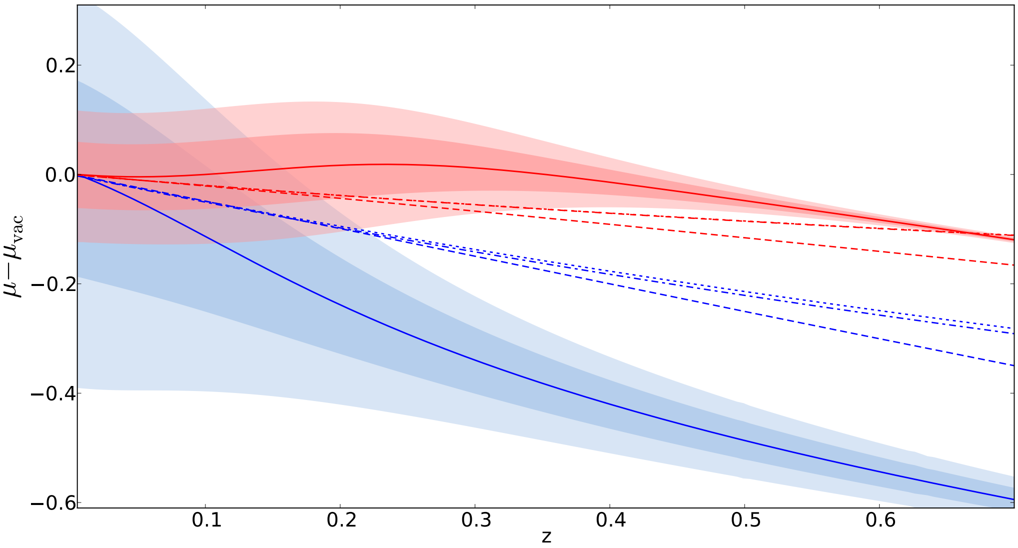

Figure 2.8: Distance moduli in the LTB model. The red curves (uppermost) are for averaging domains of size $r_{\mathfrak{D}} = 1000$ Mpc, and the blue curves for $r_{\mathfrak{D}} = 3000$ Mpc. The solid lines are the mean distance moduli found by spatially averaging the monopole of the observed distance-redshift relation, with accompanying 1σ and 2σ confidence bands. The dashed lines are the distance moduli for the distance-redshift relation in the Buchert averaged spacetime. The dotted and dot-dashed lines are the distance moduli for a series expansion of the FLRW $d_A(z)$ relation, with deceleration parameters $q = \langle q_\Theta \rangle$ and $q = \langle q_{\rm KS} \rangle$, respectively. The curves have all had their zero-points shifted to match at $z = 0$.

rameters indicating deceleration. This is caused by spatial variations in expansion rate along their lines of sight, but does not seem to be linked with spatial average properties of the spacetime, as it was in the spherical collapse and Kasner-EdS models.

Fig. 2.9 suggests that many of these observers will see a large dipole in the distance-redshift relation over their sky. Presumably, most of the observers would conclude that they lived in a Universe that is inhomogeneous on large scales, and would therefore not attempt to fit an FLRW model to their observations at all. In that case, the question of whether the monopole of the observational relation is accelerating or not becomes less of an issue. Attempts to summarise the (observational) acceleration of the model with one number, the monopole $q_{\rm obs}$, would fail. Attempting to construct a homogeneous Buchert average model

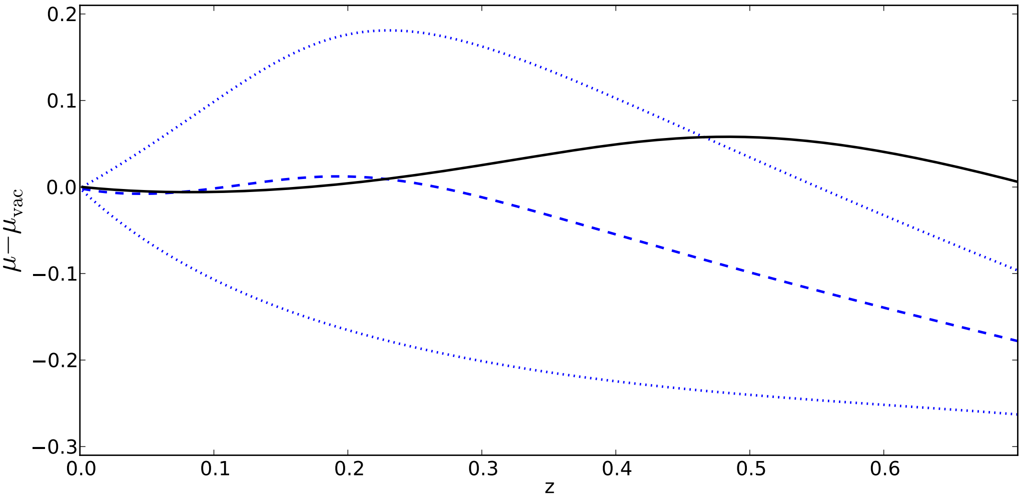

Figure 2.9: Distance modulus curves for an off-centre observer in the same model, at $r = 915$ Mpc. The dotted blue lines show the distance modulus as a function of redshift for radial lines of sight looking out of and into the void (upper and lower curves respectively). The dashed blue line is the distance modulus for the monopole of the distance-redshift relation, calculated using the dipole approximation. The solid black line is the relation for an observer at the centre of symmetry.

would probably not be seen as a sensible procedure either[1].

The Buchert average curve in Figure 2.8 is much closer to the effective local volume acceleration and Kristian-Sachs curves than to the observational curve, although it still deviates from both of them substantially. There are a number of reasons why this is the case. The first is that the model is not statistically homogeneous, and so the Buchert average does not represent the ‘typical’ conditions that a light ray would experience travelling through the spacetime[2]. Secondly, the backreaction scalar $\mathcal{Q}_{\mathcal{D}}$, of Eq. 1.42, is small in this model, because both the shear and the variance of the expansion rate are small. As such, the Buchert average deceleration parameter $q_{\mathcal{D}}$, defined in Eq. 2.7, is dominated by the same terms that appear in the definitions of the Kristian-Sachs and local volume mea-

---

[1] Instead, the Buchert averaging procedure could be used to define a ‘smoothed-out’ model that is inhomogeneous. This would result in position-dependent average quantities, and would likely be sensitive to both the shape and size of the averaging domain.

[2] In fact, it cannot, as the null geodesics involved in calculating this quantity go outside of the averaging domain.

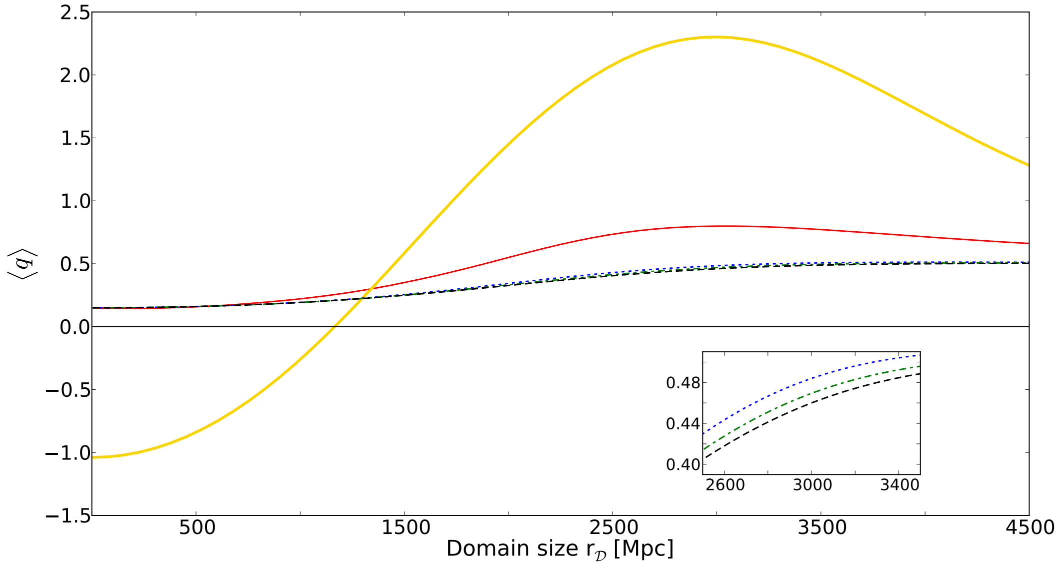

Figure 2.10: Spatial averages of various deceleration parameters as a function of averaging domain radius, $r_{\mathfrak{D}}$. The local volume (dash-dotted green line), Kristian-Sachs (dotted blue), and Buchert average (dashed black) deceleration parameters have rather similar values. A close-up of these curves is shown in the inset so that they can be distinguished. The thick, solid yellow line is the deceleration parameter found by fitting an FLRW model to the distance-redshift relation for a wide range of redshifts, $z \leq 1$. The narrower solid red line shows the same measure, but for a fit to only $z \leq 0.1$.

sures, most notably the density. While these different measures of acceleration do not *exactly* reduce to one another in this case, they are rather close (as shown in Figure 2.10, inset). One can also see that in the absence of a sensible way of defining a representative smooth model (due to the lack of a homogeneity scale), the mean behaviour of light rays should not be expected to correspond to the Buchert averaged model.

In Figure 2.10, the various (spatially-averaged) deceleration parameters are plotted as a function of averaging domain radius, $r_{\mathfrak{D}}$. The Buchert average, local volume, and Kristian-Sachs deceleration parameters track one another rather closely over the whole range of domain sizes, for the reasons discussed above. The observational curves (thick and thin solid lines) have a rather different behaviour. I obtained both of these by calculating q_0 in a (matter + curvature + Λ) FLRW model that has been fit to the monopole of the distance-redshift relation as a function of observer position[1], and then spatially averaged the resulting position-dependent value of $q_0(r)$. The yellow curve corresponds to fitting FLRW models to the distance-redshift monopole out to $z = 1$, and the red one to $z = 0.1$.

The two are very different. In particular, the fit out to higher redshifts shows acceleration for small averaging domain radii. Figure 2.9 shows why this is the case: At low redshift, the observational distance modulus curve is decelerating (which is also suggested by the fact that $q_{KS} > 0$ everywhere), but appears to accelerate at higher redshifts for observers inside the void. By fitting FLRW models to the larger redshift range, more of the apparent acceleration is captured. This behaviour is wholly due to quantities being integrated along past null directions, and is not caused by the local curvature of spacetime at any one point.

The results that I have presented for the observational deceleration are subject to the validity of the dipole approximation that was briefly discussed in Section 2.2.3. This approximation will tend to overestimate the monopole of the angular diameter distance at a given redshift, causing a decrease in $q_{\rm obs}$ relative to its exact value. As shown in Figure 2.10, this only serves to worsen the discrepancy between $\langle q_{\rm obs} \rangle$ and the other deceleration parameters at high redshift. At low redshift the approximation is most accurate [García-Bellido & Haugbølle, 2008b], and so the correction required in this regime should be expected to be small. As such, I consider these results to be robust to the use of this approximation.

2.4 Discussion

In this chapter, I have studied different concepts of what it means for a spacetime to display ‘accelerating expansion’. The measures of acceleration that are associated with these concepts all reduce to the same quantity in a perfectly

---

[1] The best-fit FLRW model may not always be a particularly good fit – the monopole of the distance-redshift relation in LTB models can take on much more complicated functional forms than are allowed in FLRW.

homogeneous and isotropic FLRW universe, but in an inhomogeneous universe I have shown that they can be very different indeed. This occurs even to the extent that some can indicate deceleration, while others indicate that exactly the same spacetime is accelerating. In universes that are statistically homogeneous on large scales, I find that in order to estimate the acceleration inferred by making observations over large distances (as is the most usual way to infer acceleration in cosmology), one is best off using a model constructed from non-local averages of geometric quantities, as occurs in Buchert's formalism, rather than considering the local expansion rate of space. This is in agreement with an argument put forward by Räsänen [Räsänen, 2009a, 2010c]. The appearance of acceleration in observations made over large scales does not necessarily imply or require the expansion of space to be accelerating, nor does it require local observables to indicate acceleration.

In the spherical collapse and Kasner-EdS models, the reconstructed distance-redshift relation, which corresponds most closely to what is actually measured in observational cosmology, is closely related to the Buchert average, and not the mean local properties of the spacetime. This means that showing that local spacetime cannot accelerate without Λ, or a quintessence field, is not sufficient to disprove backreaction as a source for the apparent late-time accelerating expansion of the Universe [Ishibashi & Wald, 2006; Green & Wald, 2011]. This does not, of course, mean that the observed acceleration can currently be said to be due to backreaction: the situations I have considered here are very much toy models (albeit ones that capture some of the properties of the real Universe). More realistic non-perturbative models of the Universe are required before any definite conclusions can be drawn about the *real* Universe. One recent attempt at constructing such models appears to show some evidence of the effects that I have described here [Bolejko & Ferreira, 2012], but it is still neither conclusive nor fully realistic.

As a corollary of the results presented here, a possible source of observational evidence for the hypothesis that the apparent acceleration of the Universe is due to inhomogeneity presents itself: if the parameters of FLRW models inferred from local observations are significantly different from those inferred from observations made over large distances, then this would seem to imply that the FLRW model used to model local spacetime is different to the FLRW model that best describes the evolution of the Universe on large scales. Any such difference would signal a significant departure from the predictions of the concordance model, and would therefore cast considerable doubt on the detection of $\Lambda \neq 0$. Of course, inferring cosmological parameters from observations made on small scales is a considerable challenge. Sample variance due to the presence of local structures, and the peculiar velocities they induce, would have to be very well-understood. Nevertheless, the possible detection of a 'Hubble Bubble' [Sinclair *et al.*, 2010] suggests that it may not be entirely impossible.

The link that I have found here between observations and the spatial average can be explained by considering that, for a large enough collection of null rays, the typical conditions experienced by a ray at a given time, t, are likely to correspond to the average of local conditions on a hypersurface of $t =$constant. These averages are exactly what Buchert's approach is constructed to estimate. As long as spacetime is statistically homogeneous and isotropic above some scale, the result then follows (assuming observers and sources are distributed in a volume-weighted way). These issues have been considered in detail in Räsänen [2010b].

In the case of the LTB model, in Section 2.3.3 I found that the Buchert average was more closely related to the local measures than to the typical distance-redshift relation of an observer, apparently in contradiction with my previous results. This model, however, is not statistically homogeneous or isotropic, and shows apparent (observational) acceleration only for a limited range of averaging domain sizes. Furthermore, the distance-redshift relation is only poorly represented by its monopole alone, since the dipole of the relation would certainly be important too. Therefore, my conclusion is that in this case the Buchert average is not enough to characterise the 'typical' properties of the spacetime, and the mean of the monopole of the distance-redshift relation is also not enough to characterise what a typical observer should expect to see. This leads me to question whether a homogeneous 'accelerating' average model, derived from an LTB model which is inhomogeneous on large scales, is in any sense physically meaningful.

Chapter 3

The KSZ effect as a test of radial inhomogeneity

As discussed in Section 1.1, the simplest and most widely applied cosmological models are based on FLRW solutions, which require the existence of some additional, unknown ‘dark energy’ component if they are to fit current observations. But are these models the only ones capable of accounting for the apparent acceleration of the cosmos?

Here, I will focus on the problem of radial inhomogeneity, as modelled by the Lemaître-Tolman-Bondi (LTB) solutions of general relativity that were outlined in Section 1.2.3. These are the general spherically-symmetric solutions of Einstein’s equations with dust, and are widely known to have more than enough freedom to account for the supernova observations without recourse to dark energy [Célérier & Schneider, 1998]. They are often referred to as ‘void models’ in the literature (but see also [Célérier *et al.*, 2010]). The relevant question is whether or not these models are compatible with other observational probes of cosmology.

This question has been addressed by various authors in a number of different contexts [Alnes & Amarzguioui, 2006; Clifton *et al.*, 2008; García-Bellido &

Haugbølle, 2008a; Zibin *et al.*, 2008; Clifton *et al.*, 2009; Bolejko & Wyithe, 2009; Biswas *et al.*, 2010; Yoo *et al.*, 2010a,b; Bolejko *et al.*, 2011a; Zhang & Stebbins, 2011; Zibin & Moss, 2011; Moss *et al.*, 2011]. Most of these studies have, however, limited themselves to the special case of spacetimes that have a spatially homogeneous energy density at early times. This is achieved by considering only those models that have a constant 'bang time'. In this case it is known that while the small angle CMB generated by a power-law spectrum of initial fluctuations can be easily reproduced within void models, an unacceptably low value of H_0 is required to do so [Zibin *et al.*, 2008; Clifton *et al.*, 2009]. However, it is also known that this problem can be alleviated by allowing for *general* radial inhomogeneity, with non-constant bang time [Clifton *et al.*, 2009]. Here I will address the problem of whether or not other cosmological observables are also consistent with models that allow for this additional freedom, as well as further investigating the parameter space of solutions that fit the small-angle CMB. In particular, I will be focusing on the kinematic Sunyaev-Zel'dovich (KSZ) effect, which was previously discussed in Section 1.3.5.

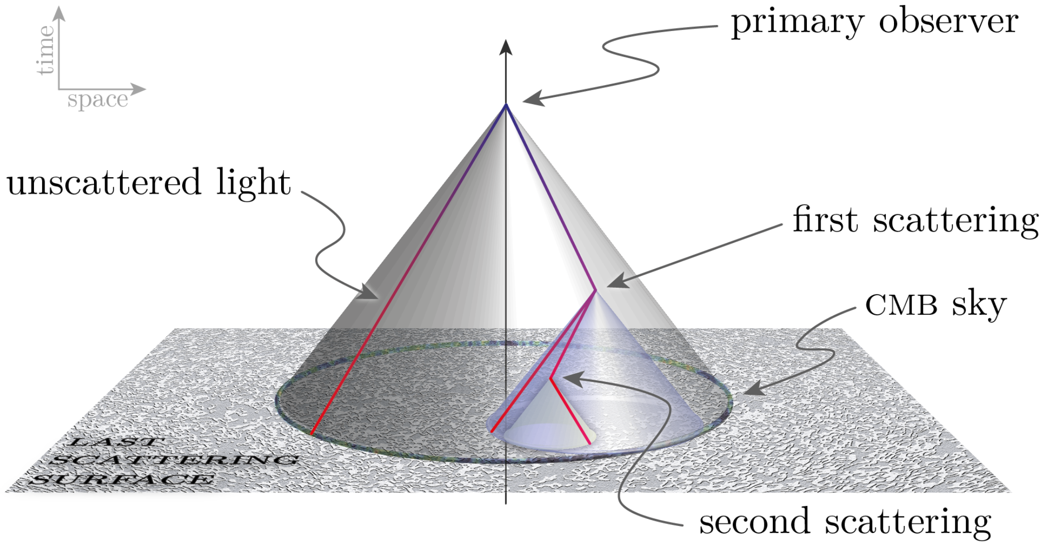

Figure 3.1: Schematic showing how the scattering of CMB photons by galaxy clusters can provide information from *inside* our past lightcone. (Taken from Clifton *et al.* [2012a].)

The KSZ effect is a particularly powerful probe of inhomogeneity as it allows us to make observations not only along the null cone that is the boundary of our causal past, but also along null curves that go inside this cone (Figure 3.1). Distant galaxy clusters essentially act as mirrors, reflecting light from the last scattering surface that would otherwise be unobservable to us. This extra information is above and beyond that which is available from the usual observations of distance measures, expansion rates and number counts, and so it is of great potential significance as a cosmological probe. The power of the KSZ effect in this context appears to have first been pointed out by Goodman [1995], although the first application of it to models that attempt to account for dark energy was performed by García-Bellido & Haugbølle [2008b]. These authors considered models with constant bang time only. I build on their work by allowing for a radially-dependent bang time.

To make progress it will be necessary to make a number of assumptions, which to avoid confusion I will state here. I assume:

- That there is perfect spherical symmetry, with ourselves at the centre of symmetry.
- That the formation of the last scattering surface proceeds as in FLRW cosmology.
- That there is a constant ratio of photons to baryons in the early universe.
- That the spectrum of initial fluctuations is a power law in wavenumber, k.
- That the energy density and all functions in the metric have smooth profiles.

The first of these is inherent in the problem I have chosen to address. General perturbations to this exact set of symmetries have been considered in Zibin [2008] and Clarkson *et al.* [2009], and the effects of being off-centre have been considered in Alnes & Amarzguioui [2006]. The second of these points is made for convenience. I am not aware of any rigorous calculation involving the formation of the last scattering surface in inhomogeneous spacetimes. The effect of allowing for an inhomogeneous photon-to-baryon ratio has been considered in Clarkson & Regis [2011], and the related question of changing the position of the last scattering surface, while keeping the bang time constant, has been addressed in Yoo *et al.* [2010b]. The effect of allowing a kink in the spectrum of initial fluctuations has been considered in Nadathur & Sarkar [2011]. I will not consider these freedoms further here, but note that a constant bang time is an assumption that would be added to similar lists in most papers. For details of the effects of relaxing these assumptions, refer to the papers cited above.

3.1 Physical properties of LTB spacetimes

In what follows, I will use the LTB solutions described in Section 1.2.3 as cosmological models that exhibit an arbitrary amount of radial inhomogeneity by supposing ourselves to be observers at the centre of symmetry. Such models are known to be able to produce excellent fits to the supernova data without requiring any dark energy, and often result in the observer being at the centre of gigaparsec-scale underdensity, or ‘void’. This is possible due to both temporal *and* spatial variations in the geometry of the spacetime that is experienced by photons as they travel through the void. Such calculations require knowledge of redshifts and distance measures in this spacetime, which can be calculated using the Sachs equations (Section 1.3.3). Expressions for the angular diameter distance and redshift for the central observer are given by Eqs. 2.30 and 2.31 in Section 2.2.3.

As discussed in Section 1.2.3, the LTB solutions have three free functions: $k(r)$, $m(r)$ and $t_B(r)$. In what follows, I set $m =$ constant (without loss of generality) by using the fact that the form of the metric is invariant under a coordinate transformation $r \to f(r)$. This leaves only two free functions, $k(r)$ and $t_B(r)$, which I parametrise as Gaussian curves,

$$k(r) = A_k \exp(-r^2/\lambda_k^2) + k_\infty \tag{3.1}$$

$$t_B(r) = A_{t_B} \exp(-r^2/\lambda_{t_B}^2) f(r), \tag{3.2}$$

where A_k, A_{t_B}, λ_k, λ_{t_B} and k_∞ are constants, and the factor $f(r) = \exp(-r^{10}/\lambda_{t_B}^{10})$ is included to attenuate the bang time profile at large r. This is done so that wide profiles can be used, while limiting the effect of early inhomogeneity on the central observer's last scattering surface. I discuss this further in Section 3.1.2.

The profiles above are defined by their amplitudes, A_i, and widths, λ_i. A further parameter k_∞ defines the asymptotic spatial curvature outside the void. The timescale of the model is set by choosing a local Hubble parameter $H_0 = H_1|_{r=0} = H_2|_{r=0}$ at time t_0, where $(t_0 - t_B)|_{r=0}$ is the age of the Universe along the world-line of an observer at $r = 0$. A rescaling can be used to set $a_1(0, t_0) = a_2(0, t_0) = 1$.

The amplitudes in Eqs. 3.1 and 3.2 can be expressed in a more familiar form as fractions of the total density at the origin today. For this purpose, I define

$$\Omega_{k_1} \equiv -A_k/H_0^2 \tag{3.3}$$

$$\Omega_{k_2} \equiv -k_\infty/H_0^2 \tag{3.4}$$

$$\Omega_k \equiv \Omega_{k_1} + \Omega_{k_2} \tag{3.5}$$

$$\Omega_m \equiv \frac{8\pi G}{3H_0^2} m(r), \tag{3.6}$$

such that $\Omega_k + \Omega_m = 1$, and consider only $\Omega_k \leq 1$ so that $\Omega_m \geq 0$.

I will now briefly consider the consequences of fluctuations in $k(r)$ and $t_B(r)$. The former of these is the analogue of the spatial curvature in FLRW solutions, which dominates the dynamical evolution of the Universe at late times. The latter changes the location of the initial singularity, and so can be thought of as modifying the early stages of the Universe's history. This interpretation is supported by treating the LTB geometry as a fluctuation about an FLRW solution. In this case the fluctuations in $k(r)$ can be mapped into growing modes, while fluctuations in $t_B(r)$ are mapped onto decaying modes [Silk, 1977].

3.1.1 Inhomogeneous late universe

First, consider $k(r)$. It can be seen from Eq. 1.30 that $k < 0$ gives a positive contribution to the expansion of a_1, while $k > 0$ gives a negative contribution. This behaviour is familiar from the Friedmann equation of FLRW cosmology. Unlike the homogeneous FLRW solutions, however, the expansion of a_2 does not always get a positive contribution from $k < 0$. On the contrary, in regions of $k < 0$ the expansion of a_2 can slow, and re-collapse can occur. This behaviour is well known, and can lead to the formation of a 'shell crossing singularity' when the collapsing region reaches $a_2 = 0$.

One can avoid shell crossing singularities in a region by satisfying the Hellaby-Lake conditions [Hellaby & Lake, 1985]. These depend on the sign of $k(r)$, and for $k \leq 0$ may be written using my notation as [Sussman, 2010]

$$(mr^3)' \geq 0, \; t_B' \leq 0, \quad \text{and} \quad (kr^2)' \leq 0, \tag{3.7}$$

while for $k > 0$ the last of these should be replaced by

$$\left[\log\left(\frac{m}{k^{\frac{3}{2}}}\right)\right]' + \frac{3t_B'|k|}{8\pi G m} \geq 0. \tag{3.8}$$

These conditions guarantee that $a_2 > 0$, so that shell crossing singularities cannot occur[1]. They are, however, very restrictive, and most applications of the LTB solutions to cosmology simply avoid the issue by making sure that shell crossings

---

[1] There are some subtleties with the sign of a_2 when $k > 0$. For details, see Sussman [2010].

only happen in the distant future. They can then be considered as a breakdown of the model at some future time, after which a more sophisticated solution including pressure would be required to avoid the formation of singularities. The existence of pressure is expected to prevent the complete collapse of matter, and a large overdensity of collapsed structures is thus expected to form instead.

3.1.2 Inhomogeneous big bang

Now, consider the consequences of fluctuations in $t_B(r)$. If $t_B(r)$ is not constant, then the 'age of the universe' differs from place to place. This is a significant departure from the standard picture of the big bang, and may initially seem odd. Certainly, there have been a number of objections to allowing inhomogeneous bang times in the literature, with the result that to date most studies of void models have expressly set $t_B(r) =$ constant *a fortiori*. In this section, I will discuss the physical significance of an inhomogeneous big bang, and argue that it is reasonable to consider models with such a feature.

As mentioned above, fluctuations in $t_B(r)$ correspond to decaying modes when the spacetime is approximated as a perturbed FLRW solution. A non-constant bang time therefore corresponds to an inhomogeneous early universe, and as one goes further back in time the size of the consequent inhomogeneity generally increases. As with the case of fluctuations in $k(r)$, there exist points beyond which the scale factor a_2 is contracting rather than expanding, and in cases where the Hellaby-Lake conditions are violated, shell crossing singularities can occur. In the case of fluctuations in $t_B(r)$, however, this behaviour occurs at very early times rather than at very late times.

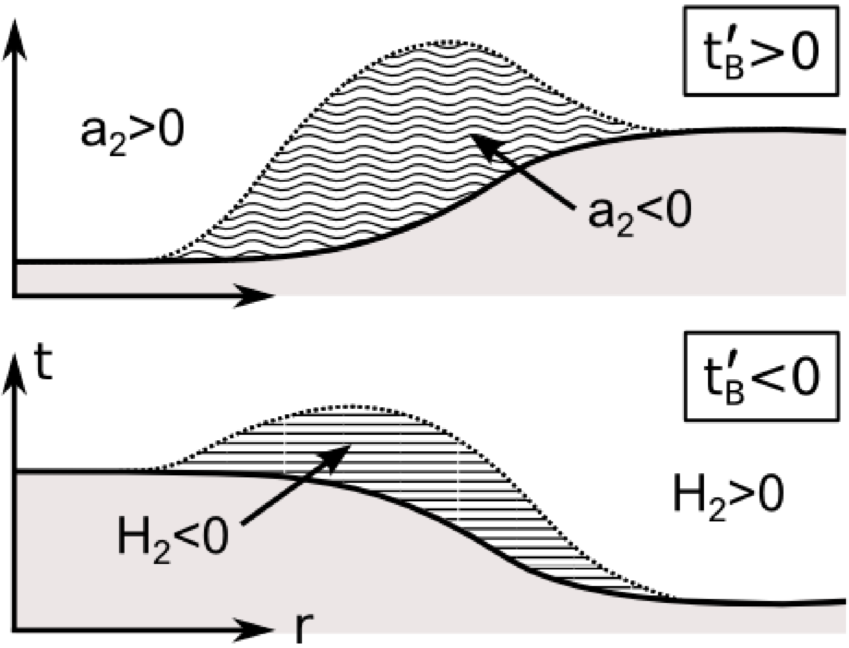

Figure 3.2: Upper panel: If $t_B' > 0$ then a surface exists with $a_2 = 0$, corresponding to the occurrence of a shell crossing singularity (dotted line). Beyond this the formal solution for the energy density gives negative values (hatched area). Lower panel: If $t_B' < 0$, regions with $H_2 < 0$ form (hatched area). The solid lines correspond to the surfaces $t = t_B$.

In Fig. 3.2, I illustrate the existence of surfaces of $a_2 = 0$ in cases with $t_B' > 0$, and regions with $H_2 < 0$ in cases with $t_B' < 0$. The former of these are the early universe analogue of the shell crossing singularities I described in the previous section, and in this case I consider the singular surface with $a_2 = 0$ to be the initial hypersurface. The latter case corresponds to regions that have started to collapse, but reach the singular surface $t = t_B$ before shell crossings occur. Contraction of this type should be expected to cause blueshifts when looking along exactly radial geodesics [Hellaby & Lake, 1984], and again this behaviour has an analogue in the inhomogeneities that form at late times [Biswas *et al.*, 2010; Moss *et al.*, 2011]. Such blueshifts would have serious effects if they were allowed to occur between the last scattering surface and an observer (for example, a distance-redshift relation $r(z)$ that is not monotonic could occur).

Célérier *et al.* [2010] find that small variations in the bang time, of order hundreds of years, lead to temperature anisotropies in the CMB of $\mathcal{O}(10^{-6})$, which are currently only marginally too small to be observed. Larger bang time variations would have a stronger observational signal, but this need not be an issue if the region of varying bang time occurs far inside the void, away from the surface of last scattering that we see directly. Nevertheless, observers elsewhere in the spacetime would see considerable anisotropies in their CMB sky, and this could be observable in the KSZ effect that we see from CMB photons that re-scatter off their cluster. The KSZ effect therefore has the potential to provide powerful constraints on the inhomogeneities caused by bang time fluctuations.

Of course, LTB models are dust-only solutions of Einstein's equations, and lose their validity when radiation becomes important at early times [Célérier *et al.*, 2010; Clarkson & Regis, 2011]. The introduction of a radiation fluid into inhomogeneous solutions complicates matters considerably, and I do not attempt to include the gravitational effects of radiation in the models here. However, in the same way that one would expect pressure to prevent the formation of shell crossing singularities at late times, one could reasonably speculate on a similar mechanism occurring at early times. I concentrate here on the matter-dominated phase of the Universe's history, which should be sufficient to model the Universe from last scattering to the present time. This is well-modelled by the LTB solutions. I leave the consideration of the gravitational effects of inhomogeneous radiation fields to other studies. For further details of this, see Clarkson & Regis [2011] and Marra & Pääkkönen [2012].

An obvious concern with models of this type is that they are difficult to reconcile with early universe inflation. This is true with models that have $t_B =$ constant, as well as models with an inhomogeneous big bang. One must then either discard inflation for the time being, or attempt to construct inflationary scenarios that result in occasional large inhomogeneities (e.g. Linde *et al.* [1995]; Afshordi *et al.* [2011]). Here, I will only address the problem of what can be said about the geometry of the Universe directly from observations, rather than imposing requirements from theories of the very early universe.

3.2 Results with constant bang time

Void models that reproduce the observed supernova distance modulus curve have proved relatively easy to construct, and little more than a moderately deep underdensity with a comoving width of order a gigaparsec is required to obtain a satisfactory fit. Indeed, the ease with which the supernova observations can be reproduced has been one of the principle factors motivating interest in these models.

The introduction of such a large inhomogeneity can hardly be expected to leave predictions for other cosmological observables unchanged, and so there have been a number of attempts to make detailed tests of voids using multiple datasets [Zibin *et al.*, 2008; García-Bellido & Haugbølle, 2008a; Biswas *et al.*, 2010]. While thorough, these previous studies have limited themselves to the case of voids with constant bang times. In this section, I summarise the constraints that can be imposed on such void models from observations of supernovae, the CMB, the local Hubble parameter, and the KSZ effect. In particular, I will draw attention to the difficulty that voids with constant bang time have in fitting the CMB and H_0 simultaneously, and will also discuss the power of the KSZ effect as a test of large-scale inhomogeneity in these models [García-Bellido & Haugbølle, 2008b; Zhang & Stebbins, 2011; Zibin & Moss, 2011].

In Section 3.3, I will consider more general voids with varying bang times. This additional freedom allows some of the constraints on the specific observables discussed in this section to be weakened significantly (although a combined fit to all datasets remains elusive).

3.2.1 Supernovae

As noted above, fitting the supernova data is a relatively simple matter, and void models can be constructed that fit any given $d_L(z)$ curve *exactly* [Mustapha *et al.*, 1997]. One should be aware, however, that reproducing the precise effects of Λ at low z requires an energy density profile that is 'cusped' at the centre [Clifton *et al.*, 2008; February *et al.*, 2010]. Generic smooth profiles produce qualitatively different behaviour, due to the Milne-like (vacuum FLRW) geometry near the origin[1], but can still be shown to be consistent with current data sets [Clifton *et al.*, 2008; February *et al.*, 2010].

3.2.2 The CMB and H_0

If the last scattering surface that we observe is located in a region of the Universe that is homogeneous and isotropic enough to be modelled as being approximately FLRW, then it is acceptable to use standard techniques to calculate the power spectrum of fluctuations on that surface. The CMB that is measured on the sky then depends on the initial spectrum, which can be calculated using an effective FLRW model, and the projection of fluctuations from the last scattering surface onto our sky. This projection depends on the spacetime geometry between us and the last scattering surface, and can be calculated from the angular diameter distance in Eq. 2.30. It is in this way that the CMB provides constraints on the geometry of the late Universe.

In general, voids and FLRW models with the same local geometry have different angular diameter distances to the last scattering surface, resulting in a relative shift in their observed CMB power spectra. The distance to last scattering can be adjusted by changing the width and depth of the void, but this typically produces relatively small shifts that are not enough to bring the peak positions of

---

[1] c.f. the difference between the observational and Kristian-Sachs acceleration measures defined in the previous chapter.

the CMB power spectrum in line with current observational constraints [Clifton *et al.*, 2009]. Changing the curvature of the FLRW region near the last scattering surface, however, produces much larger effects [Clifton *et al.*, 2009], and good fits to the small-scale CMB power spectrum can be found for void models that have positive asymptotic curvature. Such models require an anomalously low local Hubble rate ($H_0 \lesssim 50$ km s^{-1} Mpc^{-1}) in order to keep the expansion rate at last scattering low enough to be consistent with the data, however [Zibin *et al.*, 2008; Clifton *et al.*, 2009]. This is strongly inconsistent with recent observed values of $H_0 = 73.8 \pm 2.4$ km s^{-1} Mpc^{-1} [Riess *et al.*, 2011] and 67.3 ± 1.2 km s^{-1} Mpc^{-1} [Planck Collaboration, 2013]. The CMB+H_0 by themselves are therefore sufficient to effectively rule out simple void models with constant bang time.

One can attempt to avoid this conclusion by violating the assumptions that I set out at the start of the chapter. In particular, models with inhomogeneous last scattering surfaces have been considered by Yoo *et al.* [2010a] and Clarkson & Regis [2011], and a non-power law spectrum of initial fluctuations has been considered by Nadathur & Sarkar [2011]. If one is prepared to consider such additional freedoms then the CMB+H_0 constraints can be weakened considerably.

In Section 3.3, I will consider the consequences of CMB observational constraints for general void models where the bang time is allowed to vary. Clifton *et al.* [2009] have already suggested that the available constraints from the CMB+H_0 can be considerably weakened in this case, without any need to violate the assumptions introduced at the start of the chapter. In Section 3.3 I will quantify this result, finding best-fit models and confidence regions in parameter space.

3.2.3 The KSZ Effect

The kinematic Sunyaev-Zel'dovich (KSZ) effect (see Section 1.3.5) is a promising observable for testing large-scale homogeneity. As noted by Goodman [1995], and explicitly calculated by García-Bellido & Haugbølle [2008b], observers who are off-centre in a radially-inhomogeneous universe should expect to see a large fractional temperature change, $\Delta T/T$, in their observed CMB sky if they are comoving with the dust. This is because the distance-redshift relation becomes a function of direction in an inhomogeneous spacetime, so that the surface of last scattering will appear to be at different distances/redshifts in different directions on the sky of an off-centre observer. A large KSZ effect then follows, because most observers in the spacetime see a highly anisotropic CMB. Of course, this is not the case in an FLRW universe, where one should anticipate a low KSZ signal due only to the peculiar motions of the matter distribution on small scales. It is for this reason that the KSZ effect is expected to be a powerful probe of large-scale inhomogeneity.

In a void model, the dipole in the CMB is aligned in the radial direction due to spherical symmetry, and can be calculated from the relative velocity of an observer at the same point who would see an isotropic CMB. It is this dipole that can then, in principle, be measured using the KSZ effect. Using the *dipole approximation*, the magnitude of the dipole, β, can be calculated by finding the redshifts to last scattering when looking radially into and out of the void. The observer then sees an average temperature of $T = \frac{1}{2}(T_{\text{in}} + T_{\text{out}})$, where T_{in} and T_{out} are the temperatures of CMB photons seen when looking into and out from the centre of symmetry, respectively, and the relative velocity with respect to the CMB rest frame that causes this dipole is given by

$$\beta = \left.\frac{\Delta T}{T}\right|_{\text{C}} = \frac{z_{\text{in}} - z_{\text{out}}}{2 + z_{\text{in}} + z_{\text{out}}}. \tag{3.9}$$

Here, z_{in} and z_{out} are the redshifts to last scattering in the directions toward and away from the centre of the void, respectively, and $(\Delta T/T)_{\text{C}}$ is the temperature dipole evaluated on the sky of the scattering cluster. The redshifts can be calculated from Eq. 2.31, which is valid for off-centre observers [Clifton & Zuntz, 2009]. The KSZ effect can also be measured as an integrated quantity [Zhang &

Stebbins, 2011; Zibin & Moss, 2011],

$$\left.\frac{\Delta T(\hat{n})}{T}\right|_{\mathrm{KSZ}} = \int_0^{z_{\mathrm{re}}} \beta(z)\delta_e(\hat{n}, z)\frac{d\tau}{dz}dz, \tag{3.10}$$

where $\Delta T(\hat{n})/T$ is the temperature change due to the KSZ effect seen by the central observer in a direction $\hat{n}$, τ is the optical depth along the line of sight, δ_e is the density contrast of electrons, and z_{re} is the redshift back to reionisation. The autocorrelation of the integrated KSZ effect over the whole sky can be expanded in spherical harmonics to give an angular power spectrum, C_ℓ^{KSZ}. An expression for this will be given later, in Eq. 4.3.

Note that the calculation described above over-estimates β because the anisotropy seen by off-centre observers is not purely dipolar, especially far from the centre of the void [Alnes & Amarzguioui, 2006]. The dipole contribution, however, is the dominant one at low z, and so I expect the prescription outlined above to be accurate enough for current purposes. The dipole approximation was discussed previously in Section 2.3.3.

Observations of individual clusters have yielded upper limits of $\beta \lesssim 2000$ kms^{-1} [García-Bellido & Haugbølle, 2008b], and more recent observations from ACT and SPT have produced upper limits on the KSZ power spectrum at $\ell = 3000$ of around 8 μK^2 [Sievers *et al.*, 2013; Reichardt *et al.*, 2012]. This is consistent with the typical peculiar velocities expected in ΛCDM of order a few 100 kms^{-1}, but is strongly inconsistent with any large void with constant bang time that obeys the assumptions made at the start of the chapter [García-Bellido & Haugbølle, 2008b].

An example $\beta(z)$ profile that an observer at the centre of a large void with constant bang time could infer from observations of the KSZ effect is shown in Figure 3.3. Although this is only one example, the enormous magnitude of the effect is a generic result for observers located at the centre of such voids. This directly demonstrates the utility of the KSZ effect as a probe of inhomogeneity on

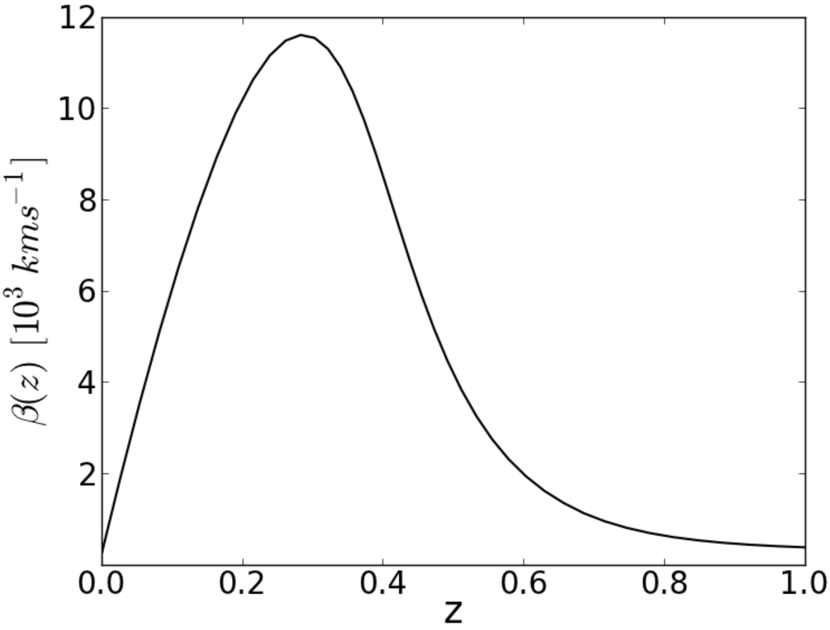

Figure 3.3: An example of the relative velocity of distant clusters with respect to the CMB 'rest frame', $\beta(z)$, that would be inferred by a central observer in a giant void with constant bang time.

large scales, and explains why current observational constraints on the KSZ effect by themselves are enough to rule out simple voids with constant bang time. In Section 3.3 I will consider the consequences of a varying bang time on observations of the KSZ effect, and show that there exist general giant void models that are consistent with constraints from current observations.

3.2.4 Other Observables

So far, I have discussed the supernova data, CMB+H_0, and the KSZ effect, and how the latter two of these provide constraints on simple void models with a constant bang time that are sufficient to effectively rule them out. I have chosen to discuss these particular observables as they are reasonably well defined in void models, easily calculable, and very constraining. There are, of course, other observables that one could also consider. These include Baryon Acoustic Oscillations (BAOs) [Biswas *et al.*, 2010; Zumalacarregui *et al.*, 2012; February *et al.*, 2012], the galaxy correlation function [February *et al.*, 2012], and the Integrated Sachs-Wolfe effect, to name just a few.

To understand these observables in the FLRW cosmological models one only needs linear perturbation theory about an FLRW background, which is very well understood (see Section 1.1.3). The observables in question can therefore be straightforwardly calculated. Linear perturbation theory in LTB cosmology, however, is significantly more complicated [Zibin, 2008; Clarkson *et al.*, 2009; Nishikawa *et al.*, 2012]. In Clarkson *et al.* [2009] a gauge invariant formalism for general perturbations in spherically symmetric spacetimes was applied to these models, where it was shown that scalar, vector and tensor modes no longer decouple (as they do to linear order in an FLRW background). This means that complicated effects can occur that are not present in FLRW cosmology. The full consequences of this behaviour have yet to be understood, and so here I have avoided the use of observables that rely on linear perturbation theory. This includes BAOs, galaxy correlation functions and the ISW effect. For treatments of some of these observables when t_B = constant, see Moss *et al.* [2011]; Zumalacarregui *et al.* [2012]; February *et al.* [2012]. For an attempt at performing Newtonian N-body simulations in an LTB background, see Alonso *et al.* [2010].

3.3 Results with varying bang time

In this section, I examine the constraints that can be imposed on general void models in which the bang time is allowed to vary. This generalizes the previous results that were summarized in Section 3.2.

As before, the observables I will use to constrain these models are the supernova distance moduli as functions of redshift, the CMB power spectrum on small scales, the local Hubble rate, and the KSZ effect. The specific data used for each observable will be explained in the subsections that follow. I use the parametrised LTB models of Section 3.1, and a Metropolis-Hastings Markov Chain Monte Carlo

(MCMC) method to explore parameter space. The likelihood function for each set of parameters is modelled as a chi-squared distribution, such that $-2\log\mathcal{L} \approx \chi^2$, and 'goodness of fit' is quantified by comparing to a ΛCDM model with WMAP 7-year best-fit parameters[1], $\Omega_\Lambda = 0.734$ and $h = 0.71$ [Komatsu *et al.*, 2011].

I will proceed by considering each observable individually, and will then go on to consider the constraints available from combinations of different observables. I find that the additional freedom allowed by varying the bang time significantly weakens the constraints that each observable imposes by itself, but that the combined power of all observables is still enough to effectively rule out these models as a possible explanation of dark energy. In particular, I show that neither the CMB+H_0 observations, nor the upper bounds on the KSZ effect for individual clusters, have the ability to rule out these models by themselves, as was the case when the bang time was assumed to be constant.

3.3.1 Supernovae

In the fits discussed below, I have used the Union2 compilation of 557 supernovae, which extends out to $z \approx 1.4$ [Amanullah *et al.*, 2010]. Other supernova datasets also exist, and void fitting procedures are known to exhibit some sensitivity to the dataset that is chosen [Clifton *et al.*, 2008; Nadathur & Sarkar, 2011]. I have chosen the Union2 data as it is one of the most extensive catalogues, and is the most widely used in the literature. The absolute magnitude of the supernovae in the Union2 data set is unknown, and is therefore fitted to each model as a nuisance parameter. I have used the published errors from the full Union2 "Covariance Matrix with Systematics", which includes an 'intrinsic error' that is added to minimize the reduced χ^2 with a ΛCDM model (and therefore assumes ΛCDM *a priori*).

---

[1] Note that the WMAP best-fit ΛCDM model is a somewhat poor fit to the data, due to a number of 'anomalies' in the temperature power spectrum at $\ell \lesssim 50$, and a rather low value for the low-ℓ polarisation likelihood [Bennett *et al.*, 2013].

The result I obtain here is predictable: as with $t_B =$ constant, the supernova data can be readily fitted by the more general LTB model.

3.3.2 The CMB and H_0

In FLRW cosmology, and for my current purposes, the CMB power spectrum can be efficiently specified on small scales with only three pieces of information[1]: (i) the acoustic horizon scale at decoupling, (ii) the acoustic scale at matter-radiation equality, and (iii) the projected scale of the CMB onto our sky. This information can be combined into three parameters in a number of different ways [Hu *et al.*, 2001; Wang & Mukherjee, 2007; Vonlanthen *et al.*, 2010; Clarkson & Regis, 2011], but here I choose to specify it as the 'shift parameter', S, the Hubble rate at last scattering, H_*, and the redshift of the last scattering surface, z_*. The shift parameter is defined as $S \equiv d_A(z_*)/\hat{d}_A(z_*)$, where $\hat{d}_A(z_*)$ is the angular diameter distance to the last scattering surface in a fiducial spatially-flat FLRW model with $\Omega_m \simeq 1$. This quantity corresponds to the change in scale of fluctuations on the sky that two observers in different spacetimes would see when looking at two identical last scattering surfaces.

Here, for simplicity, I take $z_* = 1090$, which is the redshift to the last scattering surface in ΛCDM and various other models [Vonlanthen *et al.*, 2010][2]. It now remains to impose constraints on S and H_*. To do this, I enforce the condition that the region of space in which the last scattering surface forms is well-approximated as being homogeneous and isotropic, so that standard results from FLRW cosmology can be applied in dealing with all of the physics up until the formation of the last scattering surface. It is then valid to use CAMB+CosmoMC [Lewis

---

[1] At least five pieces of information are required for a full, relatively model-independent specification of the CMB power spectrum [Vonlanthen *et al.*, 2010], but in what follows I will choose to marginalise over (or fix) the overall normalization of the power spectrum and the spectral index of the initial scalar power spectrum, as these quantities are not important for constraining the large-scale structure that is of interest here.

[2] Allowing z_* to be free would add an extra nuisance parameter to be fitted for in my MCMC runs, which would inevitably loosen the resulting constraints. As such, the CMB constraints derived here should be considered to be conservative.

& Bridle, 2002] to calculate H_* and $d_A(z_*)$ for an observer in a spatially flat and dust dominated FLRW universe looking at this surface. Using the spacetime geometry of the void models, I can then calculate S and H_0 for an observer at the centre of the void looking at an identical last scattering surface, with identical Hubble rate at last scattering, and at an identical redshift. This is the procedure followed in Clifton *et al.* [2009].

I use the WMAP 7-year data [Jarosik *et al.*, 2011], with a modified version of CosmoMC, to constrain the models. In this analysis I choose to only use data at $\ell \geq 100$, as the low-ℓ power spectrum is sensitive to the Integrated Sachs-Wolfe (ISW) effect, which is difficult to rigorously estimate in void models (see Section 3.2.4 for a brief discussion of this). This choice weakens the constraints that can be achieved on the scalar spectral index of the initial power spectrum, n_s. Conservatively, I fix $n_s = 0.96$ here[1]. The constraints imposed on S and H_* are shown in Fig. 3.4. The best fit values are found to be $S \simeq 0.875$ and $H_* \simeq 1.27 \times 10^6$ kms^{-1}Mpc^{-1}. These values are consistent with those found in Zibin *et al.* [2008] and Clifton *et al.* [2009]. Note that I did not perform the CosmoMC CMB fits jointly with the void model MCMC; instead, I ran them beforehand to get likelihoods for S and H_*, which I then used as priors for the void model MCMC.

As discussed in Section 3.2.2, it is possible to construct simple void models with $t_B =$ constant that satisfy the constraints on S displayed in Fig. 3.4. This can be achieved by simply changing the spatial curvature of the model at large z [Clifton *et al.*, 2009]. The constraints on H_*, however, are more difficult to satisfy. For simple Gaussian voids with $t_B =$ constant, under the assumptions I described above, the WMAP 7-year data and the Union2 supernova dataset are enough to show that $H_0 \lesssim 40$ kms^{-1}Mpc^{-1} is required, which is in strong disagreement with the value of $H_0 = 73.8 \pm 2.4$ kms^{-1}Mpc^{-1} measured by Riess *et al.* [2011].

---

[1] Modifying the form of the initial power spectrum can significantly weaken CMB constraints on void models [Nadathur & Sarkar, 2011].

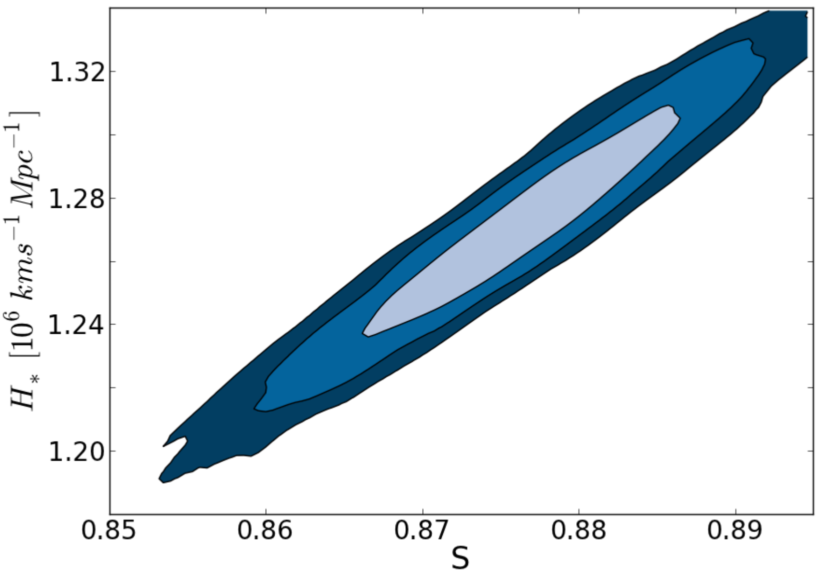

Figure 3.4: Marginalised likelihood for the parameters S and H_*, found using WMAP 7-year data and a modified version of CosmoMC. Shaded regions show the 68%, 95%, and 99.7% confidence regions.

Allowing z_* to vary can increase the upper bound on H_0 by around 5 kms^{-1}Mpc^{-1}, and changing the precise functional form of $k(r)$ can also marginally change H_0 (see Biswas *et al.* [2010]; Moss *et al.* [2011]). These are relatively small effects, though, and unless one is prepared to reject one or more of the assumptions given at the start of the chapter, models with $t_B =$ constant remain strongly inconsistent with recent measurements of H_0.

Allowing the bang time function to vary significantly improves the ability of void models to fit the CMB+H_0 data [Clifton *et al.*, 2009]. In Fig. 3.5 I plot the likelihoods for the parameters $(\Omega_k, \Omega_{k_1}, \lambda_k, A_{t_B}, \lambda_{t_B}, H_0)$ when constrained with the WMAP 7-year data, the Union2 dataset, and the measurement of $H_0 = 73.8 \pm 2.4$ kms^{-1}Mpc^{-1}. I obtained good fits to the data for models with a bang time fluctuation of width ~ 8000 Mpc that makes the Universe about 800 million years older in the centre than it is at large r. The curvature profile is narrower than this, with a width of 2500 Mpc, and a depth of 0.83 at the centre. The preferred spatial curvature at large radii is only $\Omega_{k,2} \sim +0.002$. It can be seen

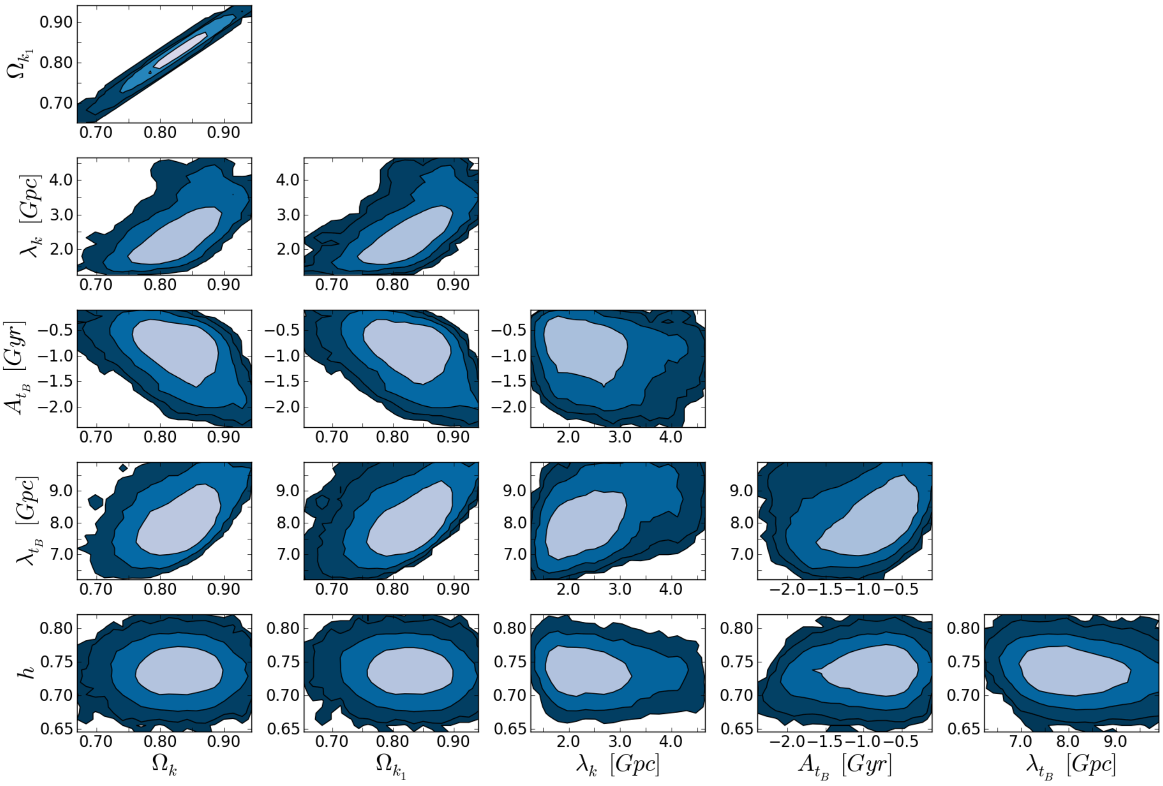

Figure 3.5: Marginalised likelihoods for a Gaussian void model with varying bang time. Shaded regions show the 68%, 95%, and 99.7% confidence regions. $H_0 = 100h$ kms^{-1}Mpc^{-1}; see the text for other definitions.

that in this case the model is able to produce an acceptably large value of H_0, with a best-fit value of 73.6 kms^{-1}Mpc^{-1}. When compared to the best-fit ΛCDM model I find that ΛCDM is slightly preferred, with $\Delta\chi^2$ =+4.5 for 560 degrees of freedom. Most of this difference is due to the void model having a poorer fit to the supernova data, even though it over-fits H_0 and the CMB data. Voids with slightly more complicated spatial curvature profiles produce fits to the data that are at least as good as ΛCDM.

In the best fitting models the curvature profile, $k(r)$, is largely responsible for shaping the void at low redshift ($z \lesssim 1$). In this region the bang time gradient is small, and so has little effect. In the region $1 \lesssim z \lesssim 2$ the curvature profile then flattens out and the bang time gradient begins to change more rapidly. This produces large fluctuations in $H_2(z)$ along our past null cone, such that H_2 can take lower values at large z. The low value of H_* required at last scattering can then be simultaneously accommodated with a large value of H_0 locally. The difference in profile widths therefore helps to explain how it is that a good fit to the data can be achieved.

3.3.3 The KSZ Effect

I will now consider the KSZ effect in void models with varying bang times. The void-induced dipole, β, can be calculated in an LTB model as follows:

1. On every point on our past null cone, solve the radial null geodesic equation for light rays travelling both into and out from the centre of the void.
2. Calculate the redshift to the last scattering surface along these geodesics using Eq. 2.31.
3. Calculate the dipole, β, using Eq. 3.9.

This procedure relies on knowing the location of the last scattering surface at different values of r. For models with a constant bang time, this surface occurs at a constant time, $t = t_{LS}$. In models with varying bang time, however, it will not occur at a hypersurface of constant t, as the presence of a bang time gradient changes the time evolution of the radial Hubble rate and density at a given r. I therefore approximate the location of the last scattering surface as a hypersurface of constant density, ρ, rather than time, t. The precise location of the last scattering surface will turn out to be important, and I will discuss the consequences of altering its position shortly.

I use the upper limits on β that have been measured from nine individual clusters [Holzapfel *et al.*, 1997; Benson *et al.*, 2003; Kitayama *et al.*, 2004], as collected in García-Bellido & Haugbølle [2008b]. These clusters span a redshift range of $0.18 \leq z \leq 0.55$. The data have asymmetric statistical errors, and are subject to large systematic errors of up to ~ 750 kms^{-1}. For further explanation of the uncertainties in this data, see García-Bellido & Haugbølle [2008b].

Void models with constant t_B have already been shown to be inconsistent with even this limited data set, as I discussed in Section 3.2.3. Within this class of models, and subject to the assumptions outlined at the beginning of the chapter, the best fitting voids are those that are either very shallow ($\Omega_{k_1} \ll 1$) or very narrow ($\lambda_k \ll 1$ Gpc), with the latter of these possibilities only working because it restricts the inhomogeneity to redshifts at which there is currently no data. I find that the extra freedom afforded by allowing the bang time to vary relaxes these tight constraints, and admits the possibility of allowing $\beta(z)$ to be small even in regions of the Universe that are strongly inhomogeneous, with Ω_{k_1} as large as 0.85.

Fig. 3.6 shows an example of a large void with varying bang time that produces small enough $\beta(z)$ to be compatible with the data discussed above. A model with the same curvature profile, $k(r)$, but a constant bang time is also displayed. It can be seen that the additional freedom allowed by the varying bang time has a considerable impact on $\beta(z)$. The energy density profile for this model is also displayed in the figure. Note, however, that the functional form of the bang time fluctuation required to produce this result is more complicated than the simple profile of Eq. 3.2. Instead, I used a sum of two (modified) Gaussian curves, of the form

$$\begin{aligned} t_B(r) = \;& A_1 \exp\left(-\left[(r-r_1)^2/\lambda_1^2 + (r-r_1)^6/\lambda_1^6\right]\right) \\ +\;& A_2 \exp\left(-\left[(r-r_2)^2/\lambda_2^2 + (r-r_2)^6/\lambda_2^6\right]\right) \end{aligned} \tag{3.11}$$

where $A_{1,2}$, $r_{1,2}$, and $\lambda_{1,2}$ are the amplitude, offset from the origin and width of the Gaussians respectively. Despite the greatly increased freedom in this bang time profile, I was unable to find a model consistent with the KSZ and supernova data simultaneously; the best-fit model had $\Delta\chi^2_{SN} = 44.1$ compared with ΛCDM. It is plausible that the situation could be improved by considering yet more

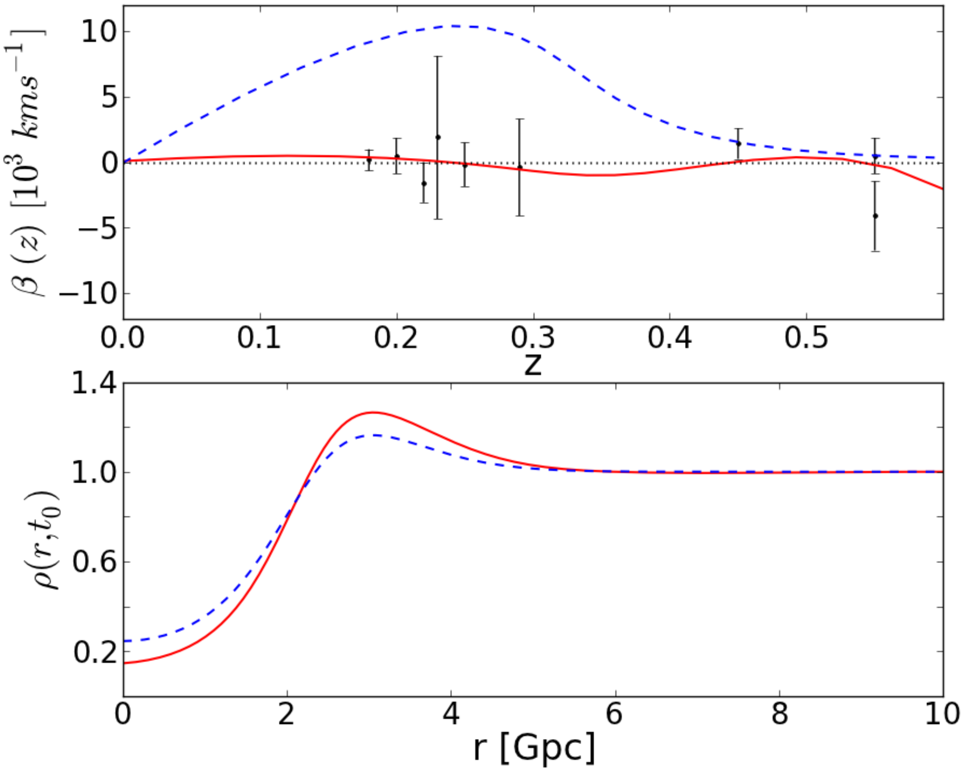

Figure 3.6: Upper panel: Velocity with respect to the CMB rest frame, $\beta(z)$, for models with constant bang time (dashed blue line) and non-constant bang time (solid red line). Both models have the same spatial curvature, $k(r)$. The datapoints are the upper limits for the nine clusters used in García-Bellido & Haugbølle [2008b]. The solid red curve has a bang time fluctuation that is the sum of two Gaussians. Lower panel: Normalised density as a function of r on a hypersurface of constant t for the same two models.

complicated functional forms for $k(r)$ and $t_B(r)$, a possibility that I investigate in Section 3.3.5. For simplicity, I have assumed in Fig. 3.6 that the offset caused by systematic errors in the data is zero. In reality, the data points would likely move slightly toward the curve to which they are being fitted, in order to improve the likelihood.

Finding models that agree with the upper limits on the KSZ angular power spectrum from ACT and SPT is a more difficult task. The KSZ effect integrated down a line of sight, given by Eq. 3.10, depends on an integral of $\beta(z)$ over redshift. Deviations from $\beta = 0$ at any redshift therefore accumulate, potentially producing a large KSZ signal. It is possible that $\beta(z)$ could be made to change sign so that negative contributions cancel the positive ones, but this would require a delicate balancing of the competing effects to satisfy the integrated and single-cluster KSZ data simultaneously. Furthermore, the angular power spectrum of KSZ fluctuations, which depends on β^2 (see Eq. 4.3), would not suffer such cancellations, and so would remain large in the presence of a void [Zhang & Stebbins, 2011; Zibin & Moss, 2011]. Bear in mind, though, that at large enough z, the effect of the void on the observed KSZ effect will decrease, as the angle subtended by the void on the distant observer's sky decreases, and the power in the dipole term of the anisotropy is shifted to higher multipoles [Alnes & Amarzguioui, 2006].

In summary, I find that large void models with varying bang times may have enough extra freedom available to alleviate the constraints that can currently be imposed from observations of the KSZ effect from individual clusters. As I discuss in the following section, however, it is unlikely that after doing this there will be enough remaining freedom to accommodate any other observables.

3.3.4 Combined Constraints (SN+CMB+H_0+KSZ)

I will now consider combining all of the observables that have been discussed so far. These are the Union2 supernova data, the WMAP 7-year data, local measurements of H_0, and the KSZ effect.

In Fig. 3.7 I show the value of β as a function of z that a central observer would measure from the KSZ effect in the models found in Section 3.3.2. These models have been shown to provide good fits to the supernova data, and the CMB and H_0 data sets simultaneously. In Fig. 3.8 I show this information as a function of H_0 for redshifts $z = 0.05$, 0.10, 0.15, and $z = 0.20$. At all redshifts considered the distribution was bimodal, with some models having $\beta \approx 1$. Such incredibly high velocities are completely inconsistent with the data, and so here I show only the models with lower β. The value of the KSZ signal that one would observe from the centre of these models is extremely large, even at low redshift. Such enormous KSZ signals are not compatible with the data displayed in Fig. 3.6, even with very large additional systematic uncertainties included.

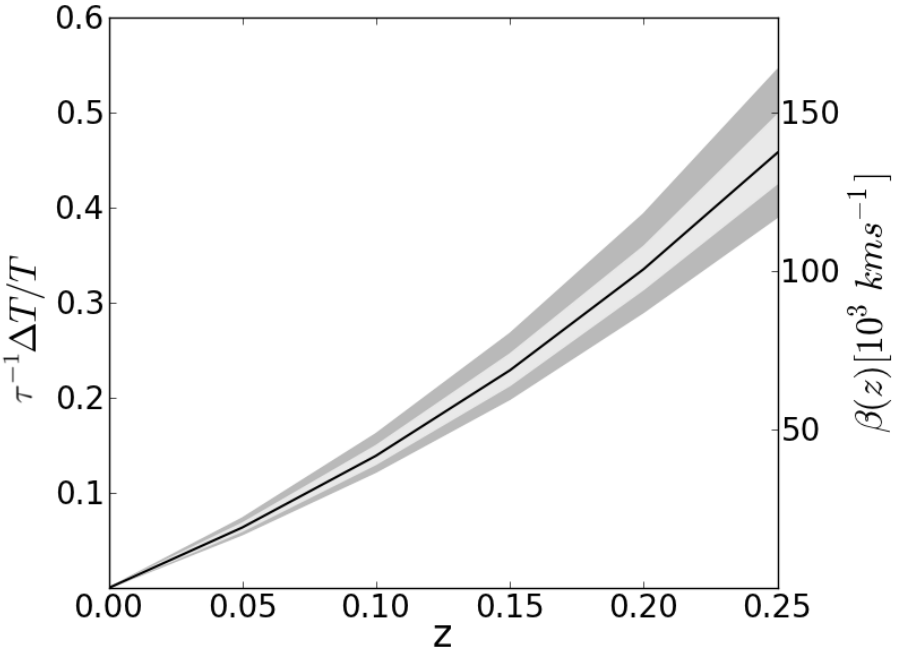

Figure 3.7: The observed value of $\tau^{-1}(\Delta T/T)_{\rm KSZ}$ as a function of redshift, for individual clusters of optical depth τ, for the best fitting models to the supernova, CMB and H_0 datasets from Section 3.3.2. The corresponding value of β is shown on the right-hand axis. The median and 68% and 95% confidence intervals are shown as the black line, and the light gray and dark gray bands, respectively. The actual distribution is bimodal, and here I show only the models with low β. Even for low redshifts, β is a large fraction of the speed of light.

The principal reason for this large effect appears to be the large width of bang time fluctuation that is favoured by the combination of supernova, CMB and H_0 datasets (see Fig. 3.5). Because of this, observers at $z \gtrsim 0.1$ look through regions in which the bang time gradient is large when they look through the void. As discussed in Section 3.1.2, these regions host shell crossings when $t'_B > 0$. This pushes the surface of last scattering to much later times, and causes significant modifications to the redshift that this surface is seen at when looking through the centre of the void. The redshift of the last scattering surface when looking away from the void experiences no such effect, as it is effectively fixed in position by the constraints on the CMB that we see, from the centre. As a result, the values of $z_{\rm in}$ and $z_{\rm out}$ in Eq. 3.9 differ significantly, and the value of β is therefore even larger than in the constant bang time case. Even at low z, this is far too high.

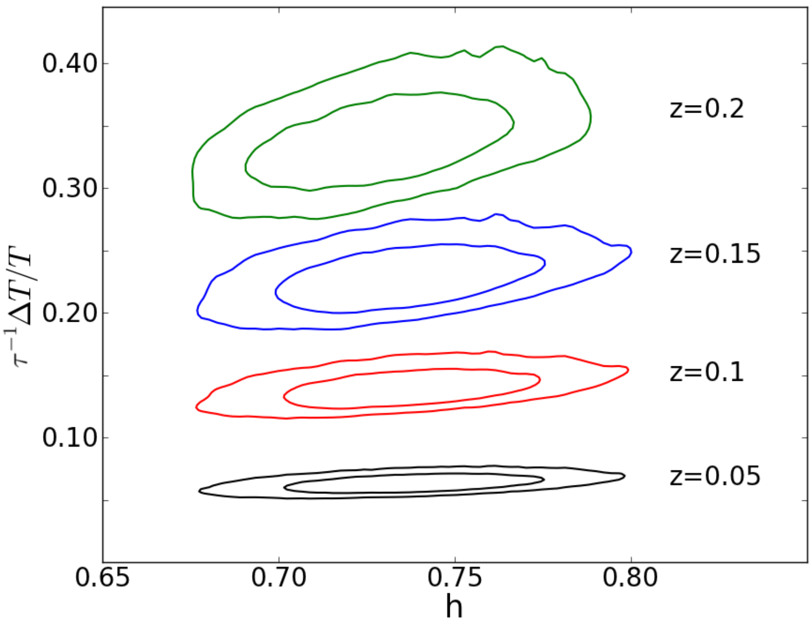

Figure 3.8: The 68% and 95% likelihood contours in the space of $\beta = \tau^{-1}(\Delta T/T)_{\rm KSZ}$ and $H_0 = 100h$ kms^{-1}Mpc^{-1}, for off-centre observers at $z = 0.05$, 0.10, 0.15 and $z = 0.2$, for the MCMC sample constrained by SN+CMB+H_0 data.

3.3.5 More Complicated Profiles

I will now question whether changing the specific forms of $t_B(r)$ and $k(r)$ that I have used so far affects these results. I showed in Section 3.3.4 that very poor agreement with the KSZ data is obtained for the models that best-fit the supernova, CMB, and H_0 data, but in Section 3.3.3 I found that a good fit to the KSZ data could be obtained if a more complicated bang time profile was used. To see if a good fit to all of the observables is possible with a more complicated model, I ran an MCMC simulation using the spatial curvature profile of Eq. 3.1 and the

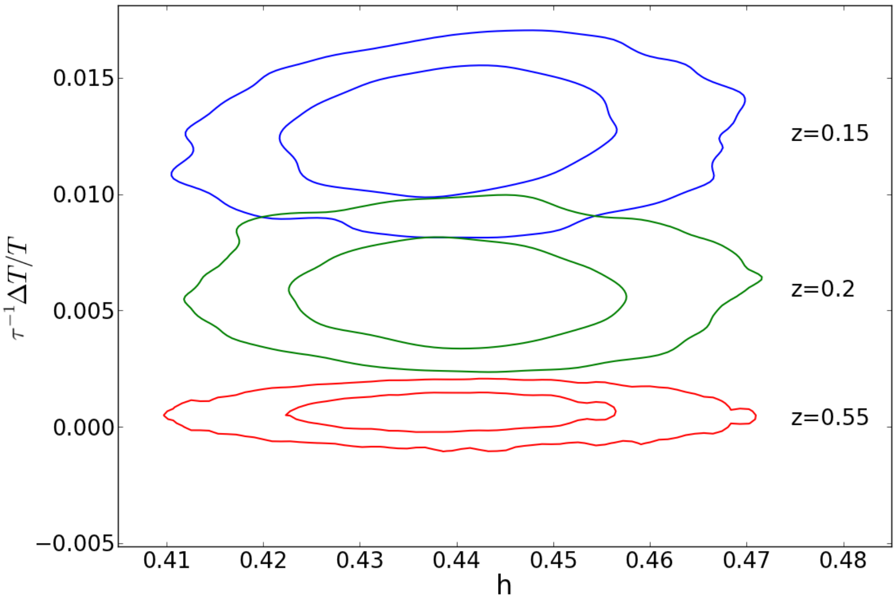

Figure 3.9: The 68% and 95% likelihood contours in the space of $\tau^{-1}(\Delta T/T)_{\rm KSZ}$ and $H_0 = 100h$ kms^{-1}Mpc^{-1}, for off-centre observers at $z = 0.15$, 0.20 and 0.55, for the MCMC sample constrained by SN+CMB+H_0+KSZ data. The $\Delta T/T$ are much lower than for the MCMC sample in Fig. 3.8, but the Hubble rate is too low to be considered consistent with observations.

extended bang time profile given by Eq. 3.11. The MCMC was constrained by the supernova, CMB, H_0, and KSZ data simultaneously.

A plot of β against H_0 for these models is shown in Fig. 3.9, and can be compared with Fig. 3.8. The models that maximize the likelihood have a $\beta(z)$ profile that is almost flat over the redshift range of interest (slightly larger at small z), and much less discrepant with the KSZ data. Relatively narrow spatial curvature and bang time profiles are preferred, extending out to only $z \sim 0.2-0.4$, and the bang time profiles are shifted towards the negative r direction (i.e. $r_{1,2} < 0$ in Eq. 3.11). A preferred H_0 of only 44.0 kms^{-1}Mpc^{-1} is obtained, and the fit to supernova and CMB data is also poor; the best-fit model is inconsistent with the data, with $\Delta\chi^2 \approx 270$ compared to ΛCDM. I conclude that this is because the fit is most sensitive to the KSZ data; it is easy to find models that are wildly inconsistent with the KSZ data, as evidenced by Fig. 3.8, and so models that minimize the χ^2 with the KSZ data above all else are preferred. These tend to

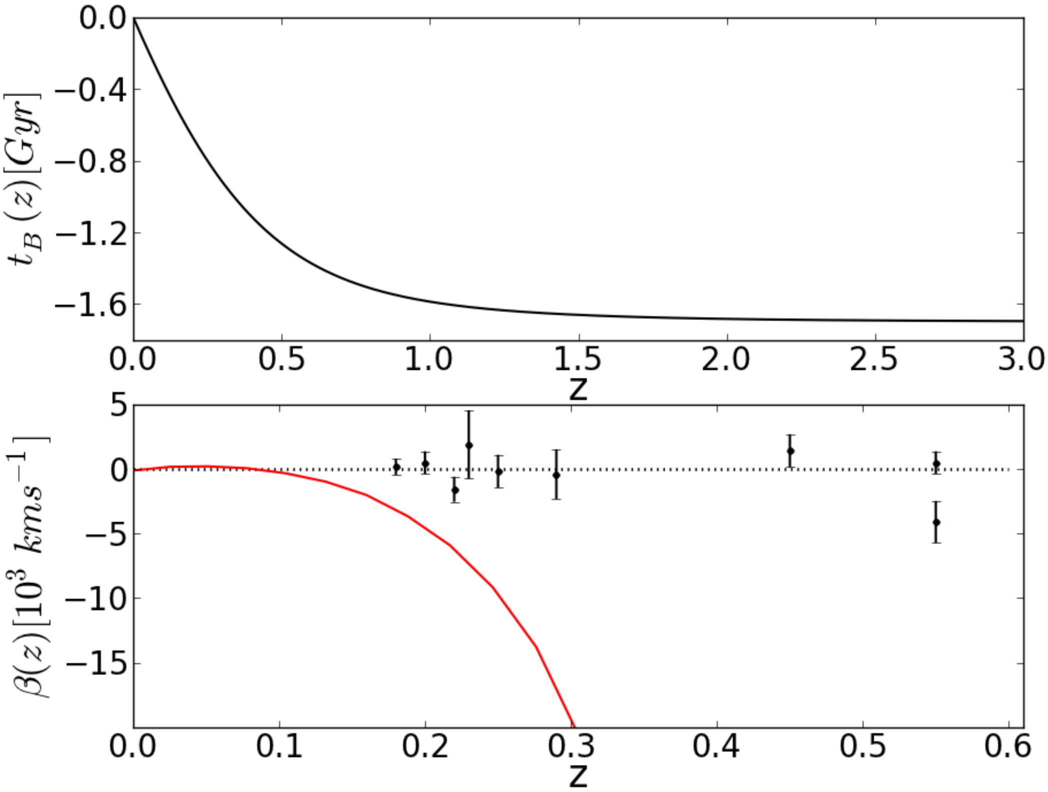

Figure 3.10: Upper panel: Bang time function, $t_B(r)$, of the LTB model found in Célérier *et al.* [2010] which reproduces the Hubble rate, $H(z)$, and luminosity distance, $d_L(z)$, of ΛCDM. Lower panel: Velocity with respect to the CMB rest frame, $\beta(z)$, for the same LTB model. $|\beta(z)|$ rapidly becomes very large ($\beta \approx -c$ for $z \gtrsim 0.6$), and produces a very poor fit to the KSZ data.

have low Hubble rates and narrow density profiles, features that are difficult to reconcile with the supernova and H_0 data. As such, it seems that even with the significantly more complex bang time profile, a good fit to all of the data simultaneously is not possible.

To further investigate the sensitivity of these results to the choice of profile parametrisation, I now consider the model found by Célérier *et al.* [2010] that was constructed to reproduce the ΛCDM values of luminosity distance and Hubble rate as a function of redshift, but without dark energy. The density profile on a hypersurface of constant t takes the form of a “hump” in this model, rather than a void, and the bang time gradient at low z is negative, so there are no shell crossings at early times. Instead, this model has double-valued redshifts at high

z (see Section 3.1.2), which almost always result in large β because z_{in} and z_{out} in Eq. 3.9 differ significantly. As such, this model is also strongly disfavoured by current KSZ data (see Fig. 3.10).

In fact, for large fluctuations in the bang time function I expect that there will *always* be a large dipole seen by off-centre observers at some range of redshifts, corresponding to lines of sight that pass near to regions with non-zero bang time gradient[1]. It therefore appears that one cannot simultaneously fit the supernova, CMB, H_0 and KSZ observations with a single LTB model unless one is prepared to violate the assumptions made at the start of the chapter.

3.4 Discussion

Recent advances in observational cosmology allow us to empirically test alternatives to the concordance model rather than relying on assumed symmetries of spacetime on the largest scales. In this chapter, I used the spherically-symmetric, dust-only LTB cosmological models, in their full generality, to test the radial homogeneity of the Universe on large scales. In particular, I considered the magnitude of the kinematic Sunyaev-Zel'dovich (KSZ) effect, which measures the dipole anisotropy of the CMB through a shift in the spectrum of CMB photons reflected from hot gas in clusters of galaxies. The KSZ effect is sensitive to large-scale inhomogeneity, as observers inhabiting an inhomogeneous universe would generically expect to see large anisotropies on their CMB skies.

In Section 3.1, I defined a simple parametrisation of the LTB radial function $k(r)$ that governs radial inhomogeneity at late times, and the function $t_B(r)$ that governs it at early times. This was used to investigate underdense 'voids' that have previously been shown to produce good fits to the supernova data. I have discussed potential problems with models that are inhomogeneous at early times

---

[1] While the model in Fig. 3.6 can be seen to fit current KSZ data, these data only extend out to $z \sim 0.6$. Even this model will have a large $\beta(z)$ for some $z > 0.6$.

(i.e. that have non-constant t_B), including the potential for disruptions around our observed surface of last scattering. In models with a positive radial derivative of the bang time, $t'_B > 0$, I found that shell crossing singularities form at early times, which push the surface of last scattering to later times. In models with negative bang time gradient, $t'_B < 0$, regions with a negative radial Hubble rate, $H_2 < 0$, form and the distance-redshift relation, $r(z)$, ceases to be monotonic. These features have observable effects that ultimately lead to predictions of a large CMB dipole anisotropy at low redshifts.

In Section 3.2 I reviewed some of the observational constraints that can be imposed on void models with constant bang time. I considered three key sets of observables: The distance moduli of supernovae, the small-angle CMB power spectrum plus local Hubble rate, and upper limits on the magnitude of the KSZ effect for individual clusters of galaxies. Voids can fit the supernova data easily, but are unable to fit recent measurements of the CMB and H_0 simultaneously (they predict a value of H_0 that is far too low). Similarly, voids that fit the supernova data predict a large CMB dipole at redshifts up to $z \sim 1$, which is inconsistent with current KSZ measurements [García-Bellido & Haugbølle, 2008b].

In Section 3.3 I considered the effect of allowing the bang time to vary on these constraints. This results in a significant increase in the freedom of the models, and allows the supernova and CMB+H_0 datasets to be fitted simultaneously, even with a simple parametrisation of the LTB radial functions. Models with small KSZ signals, consistent with the data, were also found, but these required more complex profiles and gave worse fits to the supernova data. I then proceeded to combine all of the observational constraints, and found that voids that are able to fit the supernovae, CMB and H_0 predict an extremely large KSZ effect which is orders of magnitude greater than the measured upper limits. A joint fit to the supernova, CMB, H_0, and KSZ data with a significantly more complicated bang time profile also failed to produce good agreement with the data.

I also argued that any void model with a significant bang time inhomogeneity will produce a large KSZ effect at *some* redshift. Given that a varying bang time is necessary to resolve the low-H_0 problem, it seems that the combination of supernovae, CMB+H_0 and KSZ data is enough to effectively rule out LTB void models that attempt to explain cosmological data without dark energy, subject to the assumptions made at the beginning of the chapter.

I used the dipole approximation to calculate the magnitude of the KSZ effect in my models, but this only holds if the dipole term dominates the anisotropy of an off-centre observer's sky [Alnes & Amarzguioui, 2006; García-Bellido & Haugbølle, 2008b]. Otherwise, higher multipoles become important, and the dipole approximation overestimates the KSZ effect. The dipole will dominate as long as most lines of sight on the observer's sky pass through the void, as will be the case if the observer is firmly inside it, for example. For the models in Section 3.3.3 and 3.3.4, and the Célérier *et al.* [2010] model in Section 3.3.5, the inhomogeneity extends out to $z \geq 2$, and so the dipole approximation will always be a good one for observers at $z < 0.6$, where the KSZ data lie. The models with more complicated bang time profiles considered in Section 3.3.5 have much narrower inhomogeneities, however, and so I would expect the dipole approximation to be worse. These models predict low KSZ magnitudes and are close to being consistent with the KSZ data, so any overestimate due to the dipole approximation will have little effect on their total χ^2, which is anyway dominated by the poor fits to the supernova, CMB and H_0 data. I therefore conclude that the dipole approximation is sufficient for my purposes here.

As I have tried to make clear throughout, my results are subject to several caveats that are summarised at the start of the chapter. The first, that we are exactly in the centre of a perfectly spherically symmetric void, serves to simplify the calculations but is clearly unrealistic as it fails to take into account angular variations in, for example, the galaxy distribution. This could affect observables such as the dipole anisotropy of the CMB seen by off-centre observers, potentially weakening the constraints I have derived using the KSZ effect. Allowing ourselves to be off-centre observers [Alnes & Amarzguioui, 2006; Foreman *et al.*, 2010] and introducing linear perturbations [Zibin, 2008; Clarkson *et al.*, 2009; February *et al.*, 2012] would produce more realistic models and allow more observational data to be used at the expense of a significant increase in complexity. A better understanding of linear perturbations would also go some way toward addressing my second caveat, that the formation of the last scattering surface must be in an approximately-FLRW region. In general, one could expect features such as the coupling of scalar and tensor modes in LTB perturbations to produce secondary effects such as large B-mode polarizations [Clarkson *et al.*, 2009]. This type of effect is completely absent in linear perturbation theory about FLRW backgrounds.

A particular limitation of LTB solutions as cosmological models is that they contain only dust, and cease to be applicable when radiation becomes important. If we want to approximate the Universe as an LTB model at late times, we must therefore match it to an appropriate solution containing radiation at early times. Solutions involving separate inhomogeneous matter and radiation fluids [Clarkson & Regis, 2011], spatially-varying physical quantities such as the photon-baryon ratio [Yoo *et al.*, 2010a], and scale-dependent initial power spectra [Nadathur & Sarkar, 2011] have been considered, and serve to give some idea of the extra freedom that might be obtained in more general models. Specifically, altering the location and properties of the surface of last scattering can have a profound effect on the predicted KSZ signal [Yoo *et al.*, 2010a] and the observed CMB [Nadathur & Sarkar, 2011; Clarkson & Regis, 2011], and if one is prepared to consider this additional freedom, then my present results should not strictly be expected to hold. Nevertheless, I conjecture that unless conditions at early times are rather fine-tuned, a sufficiently large inhomogeneity will generically result in a substantial KSZ signal (see Chapter 4 for further discussion).

Now consider LTB models in the context of general inhomogeneity. Rather than allowing spacetime to be described by a single LTB metric, it has been suggested that the LTB geometry should be used as an 'effective' geometry to model the scale dependence of inhomogeneity after some averaging procedure has been applied to the fine-grained structure of the actual inhomogeneous geometry of the real Universe [Célérier, 2012]. This is a considerable departure from the situation that I have been considering here. In particular, if other observers are able to construct similar effective spherically-symmetric geometries about their own locations then we should no longer expect distant clusters to see a large dipole in their CMB sky. This would completely relax the constraints that can be imposed from observations of the KSZ effect.

Finally, the effects of bang time fluctuations on another tracer of anisotropy in voids, Compton y-distortion, were studied by Zibin [2011] in a preprint that was made available soon after the work that this chapter is based upon was finished (and had itself been made available as a preprint). Its conclusions are in broad agreement with those presented here: fluctuations in the bang time that are large enough to have a significant effect on the geometry of the Universe at late times (and thus have any bearing on the low-H_0 problem) would result in Compton y-distortions many times larger than can be reconciled with current observational constraints.

My overall conclusion, then, is that significant departures from homogeneity in the radial direction are severely challenged by current observational data. It seems safe to conclude that void models based on the LTB spacetime with $\Lambda = 0$ no longer offer a viable explanation for the apparent acceleration of the Universe (up to the caveats set out at the start of the chapter).

Chapter 4

Large-scale inhomogeneity and deviations from flatness

Inflationary theory is a cornerstone of the concordance model. One of the key predictions of inflation is that the observable Universe should be extremely close to being spatially flat, typically to within $|\Omega_K| \lesssim 10^{-4}$. Current observations are consistent with flatness at around the percent level, with upper limits of $|\Omega_K| \lesssim 10^{-2}$ (95% CL) obtained from the WMAP 9-year data [Hinshaw *et al.*, 2012]. Forthcoming observations from the Planck mission are expected to yield a constraint at around the 10^{-3} level [Knox, 2006], improving to $\sim 10^{-4}$ when combined with future 21cm intensity mapping data [Mao *et al.*, 2008].

In this chapter, I consider what the possible detection of a deviation from flatness by Planck would mean for inflation (and by extension, the concordance model). In the first instance, one might take such an observation to be evidence for a genuine departure from flatness on superhorizon scales. This would have wide-ranging implications for a broad class of inflationary models; for example, a measurement of $\Omega_K < -10^{-4}$ would rule-out both slow-roll and false vacuum eternal inflation with high confidence [Kleban & Schillo, 2012; Guth & Nomura, 2012][1].

---

[1] A measurement of $\Omega_K > +10^{-4}$ would rule-out slow-roll eternal inflation only.

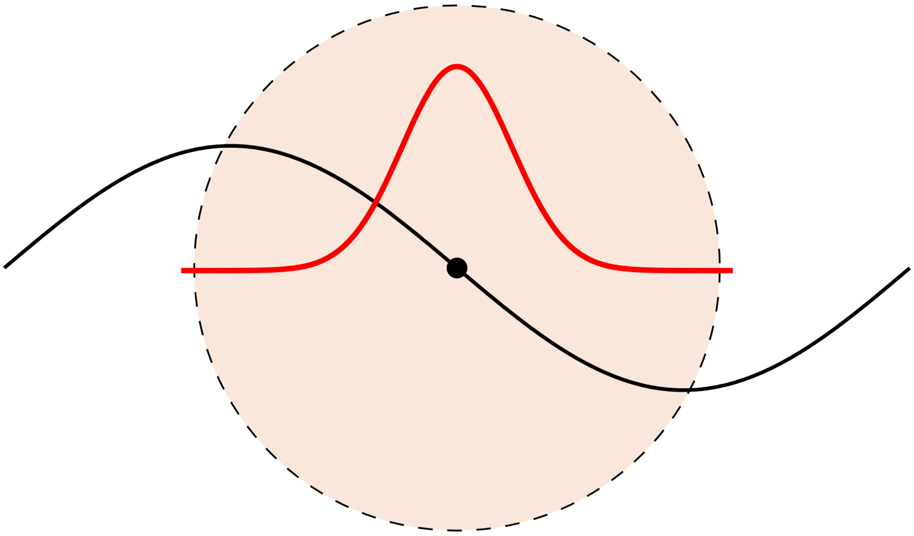

Figure 4.1: Schematic illustration of two possible ways of inducing an apparent deviation from spatial flatness: a subhorizon local inhomogeneity (red) and a superhorizon perturbation (black). The large dashed circle represents the horizon of an observer.

Another possibility is that the deviation could simply be the result of 'cosmic variance', of a sort – perhaps we live inside a local inhomogeneity that biases our determinations of cosmological parameters? I considered the effects of living at the centre if a large local inhomogeneity within the context of LTB models in Chapter 3. For a large enough amplitude inhomogeneity, it was shown that $\mathcal{O}(1)$ modifications to the FLRW quantities inferred from observations (e.g. Ω_Λ) could be obtained. As such, even the introduction of a significantly smaller-amplitude inhomogeneity should be expected to be able to produce biases in Ω_K at around the level that would apparently falsify eternal inflation. This would allow us to preserve flatness (and thus a relatively standard model for inflation) by explaining the discrepancy as the result of systematic distortions of (e.g.) the distance-redshift relation due to lensing by the inhomogeneity.

For a sufficiently large and smooth local inhomogeneity, it would be difficult to definitively distinguish between the two situations using standard cosmological tests and fitting to FLRW models. Purely geometric observables such as distance measures would be inhibited by degeneracies with evolving dark energy models, and the deviation from flatness would be too small to significantly affect the growth of structure, for example.

In this chapter, I will argue that a class of observables based on scattering processes which shift or distort the CMB frequency spectrum, including the KSZ effect discussed in the previous chapter, offer better prospects for disentangling the two scenarios than 'standard' observables. These exploit the strong relationship between spatial homogeneity and the isotropy of spacetime that was discussed in Section 1.1.4; by using them to measure the dipole anisotropy of the CMB about distant points, it is possible to place stringent constraints on the possible size of a local inhomogeneity [Goodman, 1995; Caldwell & Stebbins, 2008]. Furthermore, these observables unambiguously distinguish between subhorizon and superhorizon effects, owing to a cancellation of the dipole induced by superhorizon perturbations [Grishchuk & Zel'dovich, 1978; Erickcek *et al.*, 2008].

In this chapter, I will begin by showing how a local inhomogeneity would bias estimates of Ω_K under the simplifying assumption that it is isotropic about us, within the context of a linearly-perturbed FLRW spacetime. Although the physical situation being described is qualitatively similar to that considered for LTB models in Chapter 3, the inhomogeneity I am considering here is of a smaller amplitude, and is taken to have no significant dynamical effect on the background spacetime.

Following this, I will discuss why CMB spectral distortions/shifts are effective probes of local inhomogeneity, and derive constraints on three such observables for a simple spherically-symmetric inhomogeneity of the form $\Phi(r) = \Phi_0 \exp[-(r/r_0)^2]$, where Φ is a scalar perturbation to the FLRW metric. I will also discuss the constraints that can be expected from observations in the near future, and discuss how they relate to limits on the Grishchuk-Zel'dovich effect from the low-ℓ CMB.

For the rest of this chapter, I will adopt a fiducial flat ΛCDM cosmology with $[h, \Omega_m, \Omega_\Lambda, \sigma_8] = [0.71,\ 0.266,\ 0.734,\ 0.8]$. The redshifts of reionization and last scattering are fixed at $z_{\rm re} = 10$ and $z_* = 1090.79$ respectively. Following Zibin & Moss [2011], I take a simple model for the distribution of scatterers in the late Universe,

$$\frac{d\tau}{dr} = 1.15 \times 10^{-5} f_b (2 - Y_{He}) \frac{\Omega_m h^2 (1+z)^2}{\sqrt{1 - \Omega_k (H_0 r/c)^2}} \text{ Mpc}^{-1} \tag{4.1}$$

and model reionisation as an abrupt transition at $z_{\rm re}$. The time-dependent potential of the inhomogeneity is $\Phi(r,t) = D(t)\Phi(r)/a(t)$, where the linear growth factor is normalized to $D = 1$ at $z = 0$, and was given in Eq. 1.19.

4.1 Bias in Ω_K due to a local inhomogeneity

The presence of a large, local inhomogeneity modifies the apparent distance to last scattering through a combination of lensing, integrated Sachs-Wolfe, gravitational redshift and Doppler shift effects. Bonvin *et al.* [2006] have derived a full expression for the (subhorizon) luminosity distance perturbation, δd_L, up to linear order in perturbations, which I gave in Eq. 1.57. The observed distance $d_L(z) = \bar{d}_L(1 + \delta d_L)$, where the overbar denotes a background quantity. When considering the CMB, it is useful to rewrite this as a perturbation to the angular diameter distance, which I gave in Eq. 1.58.

As discussed in Chapter 3, an observer sitting at the centre of a spherically-symmetric inhomogeneity will measure a distance to last scattering which deviates from the background quantity by a uniform amount over the whole sky. This has the effect of introducing a shift in angular scale of the entire CMB power spectrum. The value of Ω_K inferred from observations depends primarily on the angular scale of the first few CMB acoustic peaks, and will therefore be biased away from its background value.

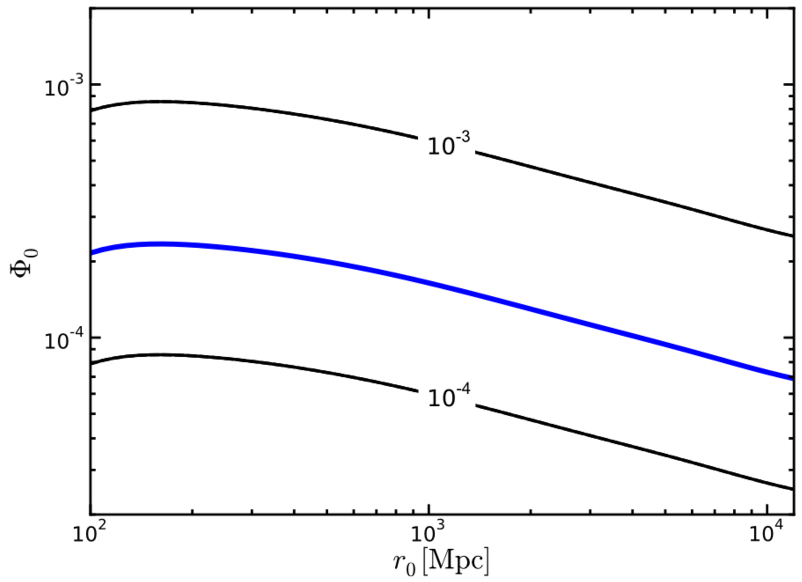

Figure 4.2: Change in the distance to last scattering, δd_A, as a function of the width and depth of the inhomogeneity. The thick blue line plots the difference in distance (in background) between models with $|\Omega_K| = 10^{-3}$ and $\Omega_K = 0$ (with identical h and Ω_m), equivalent to $\delta d_A = 2.7 \times 10^{-4}$.

Fig. 4.2 shows the distance perturbation as a function of the depth and width of a local inhomogeneity, compared with the change in (background) distance between a flat FLRW model and a FLRW model with $|\Omega_K| = 10^{-3}$. Based on the distance to last scattering alone, an inhomogeneity with $\Phi_0 \sim 10^{-3}$ would induce an apparent shift in Ω_K of order 10^{-3} for a wide range of widths.

The inhomogeneity will also cause the observed redshift of the surface of last scattering, z_*, to differ from its background value, $\bar{z}_* = z_* - \delta z_*$, where [Bonvin *et al.*, 2006]

$$\delta z = (1 + z_S) \left[\Phi_S - \Phi_O + (\mathbf{v}_O - \mathbf{v}_S) \cdot \mathbf{n} \ + 2 \int_{\eta_S}^{\eta_O} d\eta \ \mathbf{n} \cdot \nabla \Phi \right], \tag{4.2}$$

and $\mathbf{n}$ is a unit vector along the line of sight. For the central observer, the effect of the redshift perturbation is to change the inferred conformal time (and thus expansion rate) of last scattering, which will bias the estimation of parameters such as Ω_m. For an observer who is *off-centre* in the inhomogeneity, however, an additional anisotropy will also be induced in the CMB. This is because the redshift perturbation (Eq. 4.2) depends on direction; a line of sight looking towards the centre of the inhomogeneity will experience a different change in redshift to one looking away from it, and thus there will be a direction-dependent change in temperature.

In general, anisotropies will be induced over a range of angular scales, but at least for observers close to the centre of a large (wide) inhomogeneity, the dipole, β, will dominate. While there is also a dipole contribution due to the peculiar velocity of the observer, velocity perturbations due to the matter distribution on smaller scales are expected to be Gaussian random distributed with mean zero, whereas the dipole due to a large inhomogeneity will generally present a *systematic* trend in redshift and angle on the sky. This allows us to distinguish between the two contributions. For a spherical inhomogeneity, axial symmetry dictates that the dipole will be aligned in the radial direction, and that all spherical harmonic modes of the induced anisotropy with $m \neq 0$ on the sky of the observer will be zero, so that $\beta \propto \int \delta z_*(\theta) \cos\theta \sin\theta d\theta$.

4.2 Distortions caused by the inhomogeneity

There is a close relationship between homogeneity and the isotropy of spacetime (see Section 1.1.4). A number of observational tests that are sensitive to CMB anisotropies about distant points can be used to exploit this link and detect local inhomogeneities of the kind that would cause a systematic bias in measurements of Ω_K. Indeed, this was done in Chapter 3 for the KSZ effect in giant void models.

The Compton scattering of CMB radiation by ionised gas provides a way of detecting anisotropy about remote points. The scattered radiation spectrum consists of a weighted superposition of spectra from all directions on the scatterer's sky, $I'_\nu \sim \int \tau(1+\cos^2\theta) I_\nu(\theta,\phi) d\Omega$. If the scatterer's sky is a perfectly isotropic blackbody of uniform temperature, the scattered spectrum is simply a blackbody of the same temperature, plus spectral distortions due to the random thermal motions of the electrons in the scattering medium (the thermal Sunyaev-Zel'dovich effect, see Section 1.3.5). If its sky is anisotropic, however, the resulting spectrum is a combination of blackbodies of different temperatures. This has the effect of inducing additional blackbody spectral distortions, and shifting the temperature of the 'base' blackbody spectrum as seen by an observer [Goodman, 1995; Chluba & Sunyaev, 2004; Stebbins, 2007; Caldwell & Stebbins, 2008]. In the case where the dipole anisotropy dominates, these are called the Compton y-distortion and the kinematic Sunyaev-Zel'dovich (KSZ) effect, respectively.

By measuring the Compton y-distortion and KSZ effects for many scattering regions on our own sky, we can build up a picture of the degree of anisotropy, and thus inhomogeneity, within our past lightcone. I will now outline three observational tests based on these effects, and estimate what sort of constraints on a local inhomogeneity could be expected from them.

4.2.1 Kinematic SZ signal of galaxy clusters

Galaxy clusters contain a significant amount of ionized gas. Since they are effectively individual collapsed objects, they can be used to sample the dipole anisotropy induced by a local inhomogeneity at discrete points in space. This is useful for reconstructing the systematic trend in dipole anisotropy as a function of redshift that a local inhomogeneity would be expected to produce (see, for example, Fig. 3.3). Each cluster has a characteristic integrated optical depth of $\tau \sim 10^{-3} - 10^{-2}$. The KSZ signal due to a single galaxy cluster at redshift z is $\Delta T/T = -\beta(z)\tau$, and can be extracted from CMB sky maps given a sufficiently accurate component separation method and low-noise data.

The KSZ effect from individual clusters is difficult to measure owing to the smallness of the signal, confusion with primary CMB anisotropies, and other dominant systematic errors [Benson *et al.*, 2003]. Currently, only upper limits

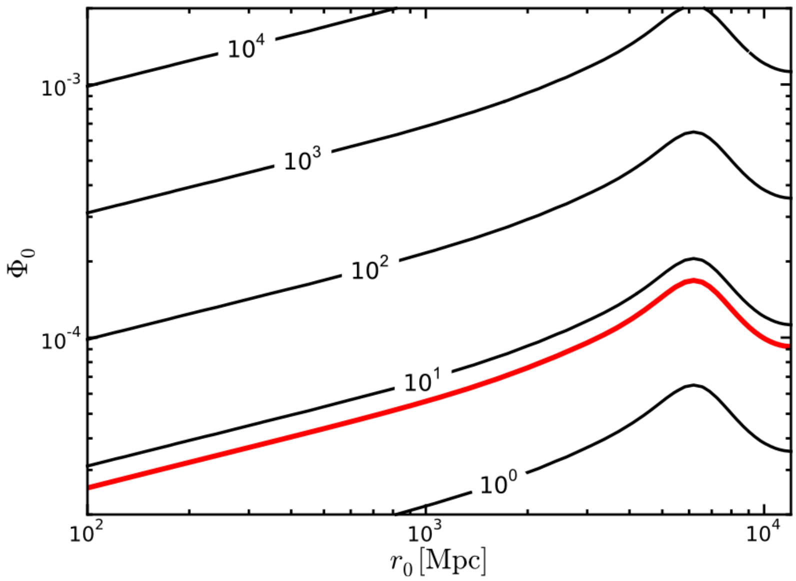

Figure 4.3: The KSZ power $D_\ell = \ell(\ell+1)C_\ell T_0^2/2\pi$ at $\ell = 3000$, in μK^2. The thick red line is the SPT upper limit of $D_{3000} < 6.7\mu K^2$ (95% CL).

are available, but this may soon change as data from Planck and small-scale CMB experiments such as ACT and SPT become available. Current data have nevertheless been used to constrain inhomogeneous relativistic cosmological models for dark energy, as I discussed in Chapter 3.

4.2.2 Kinematic SZ angular power spectrum

The angular power spectrum of the KSZ effect is easier to measure than individual cluster KSZ because it is an integrated quantity and has additional contributions from the diffuse intergalactic medium that is not associated with clusters (sometimes called the Ostriker-Vishniac effect [Ostriker & Vishniac, 1986; Jaffe & Kamionkowski, 1998]). I adapt the expression for the KSZ power spectrum from a large-scale inhomogeneity that was derived by Zibin & Moss [2011] to obtain

$$C_\ell \approx 8\pi^3 \int_0^{r_{\rm re}} dr\; r^{-3} \left[\beta(z)\frac{d\tau}{dr}\right]^2 P(k(r), z(r)). \tag{4.3}$$

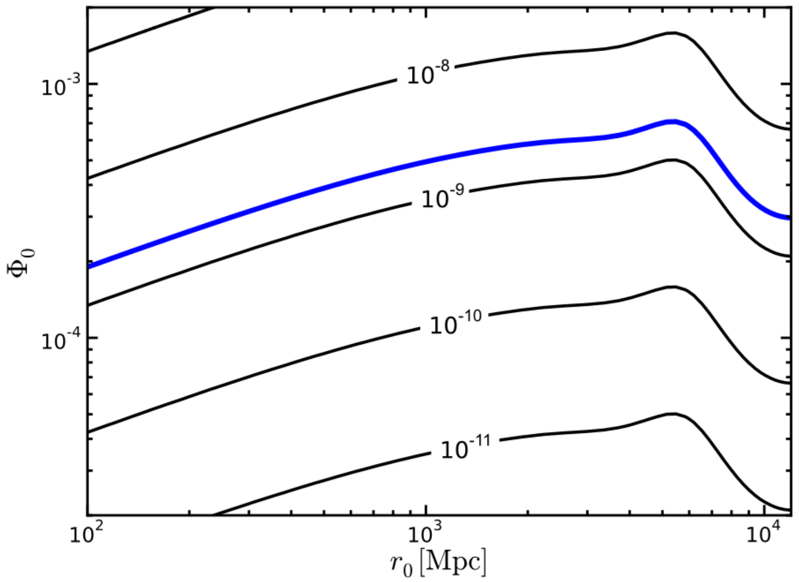

Figure 4.4: The y-distortion induced by a spherically-symmetric inhomogeneity. Also plotted is the projected upper limit from PIXIE (thick blue line).

The Limber approximation has been used, giving $k(r) = (2\ell + 1)/2r(z)$, so that all quantities are evaluated on the past lightcone. At high-ℓ, the KSZ signal is strongly dependent on the nonlinear matter power spectrum, $P(k, z)$, which I modelled using HaloFit/CLASS [Blas *et al.*, 2011]. Results for the simple spherically-symmetric model are shown in Fig. 4.3.

At a characteristic angular scale of $\ell \sim 3000$ (where the primary CMB signal becomes subdominant), the signal is dominated by contributions from matter inhomogeneities at lower redshifts, where the induced anisotropy is mostly dipolar. These scales are accessible to CMB experiments such as ACT and SPT, which have recently put stringent upper limits on the combined TSZ+KSZ power [Reichardt *et al.*, 2012; Sievers *et al.*, 2013]. Accessing the bare KSZ signal is complicated by difficulties in modelling the distribution of extragalactic point sources, and contains a theoretical uncertainty due to the unknown 'patchiness' of reionisation, which also contributes a KSZ effect [Santos *et al.*, 2003].

4.2.3 Compton y-distortion

Spectral distortions arising from the Compton scattering of an anisotropic CMB can be parametrized as a y-type blackbody distortion. In the case where the dipole dominates, the observed y-distortion is a monopole [Zibin & Moss, 2011],

$$y = \frac{7}{10} \int_0^{r_{\rm re}} dr \, \frac{d\tau}{dr} \beta^2(r). \tag{4.4}$$

Results for my model are shown in Fig. 4.4. Measurement of the y-distortion requires an instrument for which an absolute calibration of the spectral response can be obtained. This excludes most recent CMB experiments, and so the best current constraints come from COBE/FIRAS, which found $y < 1.5 \times 10^{-5}$ (95% CL) [Fixsen *et al.*, 1996]. The planned PIXIE mission [Kogut *et al.*, 2011] could improve the determination of y by some four orders of magnitude if realised.

4.3 Constraints on deviations from flatness

My calculations for this simple model give some sense of the effectiveness of the different CMB scattering tests in constraining the size of a local inhomogeneity. A depth of $\Phi_0 \sim 3 \times 10^{-4}$ is sufficient to induce a bias in the inferred spatial curvature of $\Delta\Omega_K \approx 10^{-3}$ for a wide range of r_0 (Fig. 4.2). Existing upper limits on the KSZ power at $\ell = 3000$ from SPT are sufficient to rule out an inhomogeneity of this depth with a width less than around 8 Gpc, although larger r_0 are still allowed (Fig. 4.3). The Compton y-distortion, on the other hand, provides much weaker constraints even with the great increase in precision that would be possible with PIXIE (Fig. 4.4). Part of the reason for the relative effectiveness of the KSZ power spectrum is its density weighting, which enhances the signal at the high-ℓ probed by precision CMB experiments.

The above calculations are only intended to be illustrative, and more detailed modelling would be required to produce firmer constraints if a deviation from flatness was detected. For example, the KSZ angular power spectrum is sensitive to the nonlinear contributions to $P(k)$ [Zibin & Moss, 2011], and the form of $\beta(z)$ to the shape of the potential, $\Phi(r)$, so uncertainties in these functions should be treated carefully. For wider inhomogeneities, there is also a (relatively minor) dependence on the details of reionisation. Finally, the assumption that the inhomogeneity is perfectly spherically symmetric, and that we are exactly at its centre, should also be relaxed. (A realistic inhomogeneity cannot be too asymmetric, or place us too far from the centre, however; otherwise, it would fail to match the smallness of deviations from isotropy and moderate size of the CMB dipole that are observed locally [Foreman *et al.*, 2010].)

Why should we expect to find ourselves near to the centre of a large inhomogeneity in the first place? Although such a situation may seem unlikely (e.g. Foreman *et al.* [2010] estimate around a 10^{-8} chance that we should find ourselves sufficiently close to the centre of a giant void to match constraints from the observed local CMB dipole), there are inflationary mechanisms known in the literature which preferentially place observers near the centre of large underdensities [Linde *et al.*, 1995]. Furthermore, Ellis [2011] has argued that it would be inconsistent to rule-out such inhomogeneities on strictly *a priori* probabilistic grounds, since we currently accept features in our cosmological models that are substantially less probable anyway. As such, observations should be the final arbiter in deciding whether a large inhomogeneity exists or not.

Wouldn't its presence have already been discovered through other observations? Inhomogeneities of the kind considered here modify the low-ℓ CMB, causing alignment of low-ℓ multipoles [Alnes & Amarzguioui, 2006], and changes in the ISW signal, temperature-polarization cross-spectrum, and associated modifications to the reionisation history [Moss *et al.*, 2011]. The induced effects tend either to be smaller than cosmic variance at the relevant scales, or strongly depend on the details of the model, however, rendering these tests inconclusive.

Superhorizon perturbations also produce fluctuations in the low-ℓ CMB. Despite having wavelengths larger than the horizon, such perturbations still lead to spatial variations in the potential on very large (but still sub-horizon) scales, as illustrated in Figure 4.1. This contributes to the temperature anisotropy of the CMB on large angular scales, and is known as the Grishchuk-Zel'dovich effect [Grishchuk & Zel'dovich, 1978].

In a number of cosmological models (including ΛCDM), it has been shown that there is a cancellation between the anisotropy and peculiar velocity induced by such perturbations, resulting in no net dipole to first order [Erickcek *et al.*, 2008]. Constraints from the low-ℓ CMB are therefore complementary to CMB scattering tests of the sort outlined above: A deviation from spatial flatness caused by a local inhomogeneity results in a net dipole about many locations within our horizon, which can be measured using (e.g.) the KSZ effect, whereas a superhorizon deviation from flatness will produce no such signal, instead causing an enhancement of the quadrupole and higher moments of our local CMB.

In conclusion, an observation of $|\Omega_K| > 10^{-4}$ is not sufficient to rule-out eternal inflation – it would also have to be shown that the inferred deviation from flatness was not caused by the effects of a local inhomogeneity instead. Observations of the KSZ effect and Compton y-distortion, taken with constraints on the size of the Grishchuk-Zel'dovich effect from the low-ℓ CMB power spectrum, present a viable method of determining the source of such a discrepancy.

4.4 Testing the Cosmological Principle

So far, I have only considered the effects of a dipole anisotropy in distorting the CMB blackbody spectrum. As mentioned previously, the dipole contribution is expected to dominate the anisotropy in the CMB caused by large, spherically-symmetric inhomogeneities of the types considered in this chapter and the one previous. By considering general anisotropies about distant observers, however, one can show that spectral distortions arise from *arbitrary* deviations from homogeneity and isotropy [Clifton *et al.*, 2012a]. In this section, I will briefly discuss how this can, in principle, be used to empirically test the Cosmological Principle.

Consider a universe that is filled with scattering regions of optical depth τ at every redshift. The total intensity of CMB radiation along a given line of sight is

$$I_{\rm tot} = \mathcal{B}(\nu, \bar{T}_c) + \int I_r(\nu, \bar{T}_i, z) dz - \int I_r(\nu, \bar{T}_c, z) dz, \qquad (4.5)$$

where $\mathcal{B}$ is the intensity of unscattered CMB radiation, which I assume to have been produced as a pure, isotropic blackbody, and $\bar{T} = (1+z)T$ is the temperature of the unscattered CMB at a given redshift. The second term on the right hand side accounts for CMB photons that have now been scattered down the line of sight, but otherwise would not have travelled towards the observer. The third term accounts for the photons that would have reached the observer had they not been scattered. The intensity of Compton-scattered radiation from an individual scattering object is (see Section 1.3.5)

$$I_r(\nu, T_i, z) = \frac{3}{16\pi} \int \tau (1 + \cos^2\theta) \mathcal{B}(\nu, T_i) \sin\theta d\theta d\phi, \qquad (4.6)$$

where $T = T(\theta, \phi, z)$ is the CMB temperature field on the sky of the scatterer (which I take to be comoving). If the Universe is perfectly homogeneous and isotropic, the temperature field about every scatterer will be constant over the whole of the scatterer's sky (i.e. pure monopole). In this case, the second and third terms in Eq. 4.5 cancel, and so the radiation remains blackbody. If there were an angular variation in the temperature about the scatterer (which would necessarily occur in an inhomogeneous universe, according to the Ehlers-Geren-Sachs theorem discussed in Section 1.1.4.3), the second and third terms would no longer be proportional to a blackbody spectrum, and so they will contribute a spectral distortion to $I_{\rm tot}$. If these spectral distortions could be measured and separated from other sources of distortion (such as the thermal Sunyaev-Zel'dovich effect), observational constraints could be placed on deviations from perfect homogeneity and isotropy.

This is not yet enough to satisfy the EGS theorem, however, which requires that the CMB is isotropic around *all* points in a spacetime patch, and not just the ones lying down our past light cone (i.e. the scattering regions that we can observe directly). There are two ways that enough information might be collected to fully satisfy the EGS theorem, and thus empirically prove the Cosmological Principle:

- Observe the CMB for a finite interval of time [Quercellini *et al.*, 2012]. This would allow us to receive information about the CMB sky of all observers in the 4-dimensional region of spacetime swept out by our past null cone over this interval. If no spectral distortion effect is measured at any time, then one can infer that the entire region is filled with clusters that see isotropic CMB radiation. The region must therefore have FLRW geometry, and taking any surface within it as an initial Cauchy surface, we can establish that our entire causal past must also be FLRW.
- Observe CMB radiation that has been scattered more than once [Dolgov *et al.*, 2001; Itoh *et al.*, 2001], as was suggested in the original paper by Sunyaev and Zel'dovich [Sunyaev & Zel'dovich, 1980]. This situation is illustrated by the existence of the 'second scatterer' in Figure 3.1. If such scattering is observable, the CMB sky of the second scatterers must also be isotropic if we are still to observe the re-scattered CMB photons as being a blackbody. Only two scatterings are required, as this is sufficient to show that the CMB must be isotropic around every point in our causal past.

Neither of these methods is immediately practical with current technology. A second scattering would have an amplitude of $\tau \sim 10^{-3}$ relative to the first scattering, which is difficult to observe in the first place, and the interval of time between CMB observations required to reconstruct the geometry on an initial Cauchy surface accurately enough is likely to be very long, on the order of $10^{-5}H_0^{-1}$ (for assumed metric fluctuations of order 10^{-5}). I therefore conclude that a rigorous observational proof of the Cosmological Principle should be possible in principle using the spectral distortion test I have just outlined, but a practical measurement is likely to be some way off.

Chapter 5

Extracting Sunyaev-Zel'dovich signals from CMB sky maps

In the last two chapters, I concentrated on the question of how the kinematic Sunyaev-Zel'dovich effect (and similar scattering effects) can be used to test homogeneity on large scales. The full range of cosmological information encoded by the KSZ effect is much broader than this, however. In particular, it can be used to probe the peculiar velocity field on intermediate scales (above a few Mpc), which in linear theory is closely related to cosmological quantities that describe the matter distribution, such as the matter power spectrum (see Section 1.1.3). Since the peculiar velocity is weighted by a factor of $1/k$ with respect to the matter density [Dodelson, 2003][1],

$$\vec{v}(k,a) = i f(a) a H(a) \delta(k,a) \vec{k}/k^2, \tag{5.1}$$

and is relatively unbiased with respect to the underlying density field, it is less sensitive to difficult-to-model nonlinear effects that crop up in the matter distribution on small scales. As such, observations of the KSZ effect can in principle be used to determine the matter power spectrum without suffering from the

---

[1] Note that Eq. 5.1 is only strictly valid on scales well within the horizon.

nonlinear modelling uncertainties that plague direct tracers of the density field like galaxy redshift surveys. A KSZ peculiar velocity survey would therefore be strongly complementary to existing probes of large scale structure.

Accessing this information is far from easy, however. The KSZ signal is small, and despite the current abundance of data from high-sensitivity CMB experiments, the first accepted positive detection of the effect was made only very recently [Hand *et al.*, 2012]. Previous claims of a significant detection in the WMAP data by Kashlinsky *et al.* [2009] were met with scepticism; the claimed signal was much larger than the ΛCDM prediction, and attempts to reproduce the result either failed, or pointed out methodological errors in the original analysis [Keisler, 2009; Song *et al.*, 2010; Osborne *et al.*, 2011] (although see Atrio-Barandela *et al.* [2012] for a rebuttal). Unmodelled contributions to the sky signal and correlations and degeneracies between sky components proved to be problematic, as did incorrect estimates of statistical uncertainty. A correlation between the TSZ effect and the Cosmic Infrared Background is known to be degenerate with the KSZ signal in small-angle CMB experiments, for example [Addison *et al.*, 2012], and the frequency spectrum of KSZ is degenerate with that of the primary CMB. Since the typical KSZ signal from an individual cluster is so small (and contaminated with other effects), ways of stacking or summing contributions from many clusters are required to produce a significant detection. Several peculiar velocity statistics that should be suitable for this purpose are reviewed in Section 5.1.3.

While simply detecting the KSZ effect is a necessary first step, a method for *accurately* characterising the signal will be required if we are to use it to do cosmology. In Section 5.1.2, I have reviewed a number of methods for extracting the KSZ effect, but it is not obvious that any of these will be any more effective than the method of Kashlinsky *et al.* [2009] in accurately determining the signal. What is needed is an extraction method that is capable of accurately modelling all relevant components of the sky simultaneously, and propagating uncertainty in a well-defined, statistically-rigorous way. It must also use a signal 'stacking' procedure with a clear theoretical interpretation if meaningful cosmological constraints are to be derived.

I will discuss a proposal for such a method in Section 5.2. It is an extension of the Commander CMB component separation code [Eriksen *et al.*, 2004], which uses a Gibbs sampling scheme to extract various sky components (primary CMB anisotropies, galactic foregrounds, etc.) from multi-frequency CMB data by calculating the full joint posterior probability distribution for all of them. For a given signal, marginalising over all other contributions results in an estimate of the signal that automatically takes into account degeneracies and correctly propagates statistical uncertainties – properties that will be very necessary for accurate KSZ extraction. This method also makes it easy to directly estimate various peculiar velocity statistics, simply by adding an appropriate term into the likelihood. It can also be extended to other types of localised signal on the sky, including the thermal SZ effect from clusters, and hypothesised exotic features in the CMB.

5.1 Cosmology with the SZ effect

I will now briefly review the cosmological information content of both the kinematic *and* thermal SZ effects, and discuss methods for their extraction that have been proposed in the literature. The TSZ effect will turn out to be an important part of the KSZ extraction procedure, as it is easier to detect than KSZ and provides additional information on the physical properties of the galaxy cluster. I will also survey a number of peculiar velocity statistics; since $(\Delta T/T)_{\rm KSZ} \propto v$, these provide a natural basis for statistically summing the KSZ signals of many individual clusters. They can also be calculated directly in perturbation theory, and so are useful for producing constraints on the background cosmology.

5.1.1 Thermal SZ effect

The current generation of high-sensitivity CMB temperature mapping experiments have made it possible to reliably detect and characterise secondary CMB anisotropies for the first time [Aghanim *et al.*, 2008; Shirokoff *et al.*, 2011]. Principal among these is the Sunyaev-Zel'dovich (SZ) effect from clusters of galaxies, which I first discussed in Section 1.3.5.

The *thermal* SZ effect is of particular interest as a probe of large scale structure, since its integrated amplitude appears to be a direct tracer of cluster mass [Motl *et al.*, 2005; Reid & Spergel, 2006], and its surface brightness is almost independent of redshift. This means that, in principle, SZ surveys can be used to reconstruct the number density of clusters, $n(M, z)$, out to high redshift.

The abundance of massive clusters is sensitive to key cosmological parameters such as Ω_m and σ_8 (the RMS fluctuation in matter density in a sphere of radius $8\ h^{-1}$ Mpc) [Battye & Weller, 2003; Sehgal *et al.*, 2011; Benson *et al.*, 2013], and the extreme high-mass tail of this distribution can be used to put constraints on modifications to gravity [Jain & Zhang, 2008] and the degree of non-Gaussianity of the cosmological density field [Matarrese *et al.*, 2000]. Since the SZ effect traces intra-cluster gas, it can be used to probe the gas distribution in both observed and simulated clusters [Nagai, 2006; Reid & Spergel, 2006]. SZ observations of clusters have also been used as a cosmological distance measure [Reese *et al.*, 2002]. The detection and characterisation of large samples of clusters using the SZ effect is therefore an exciting prospect for cosmology (see Carlstrom *et al.* [2002] for a review).

In order to make such studies possible, large cluster surveys with a high degree of completeness (up to some mass limit) and accurate mass estimates are required. These have been difficult to construct in practise, and blind SZ surveys have only recently started to yield appreciable samples of clusters [Vanderlinde *et al.*, 2010; Marriage *et al.*, 2011; Planck Collaboration, 2011a]. Detections are typically made using map filtering techniques to remove the contaminating primary CMB and foreground signals and estimate the amplitude and size of the cluster SZ profiles (e.g. Leach *et al.* [2008]; Herranz *et al.* [2012]). Such techniques tend to be optimised for detection efficiency rather than accurate amplitude estimation however, and so cluster masses derived from these methods have limited accuracy [Schäfer *et al.*, 2006; Planck Collaboration, 2012b,a]. Once a detection has been made, more specialised SZ signal extraction methods can be applied to the individual clusters.

Unfortunately, the fact that most clusters are barely resolved by current CMB experiments leads to a degeneracy between SZ amplitude and cluster radius which hampers more sophisticated mass estimation methods [Planck Collaboration, 2011a]. As a result, cluster masses can currently be determined only to within an accuracy of around 30% using observations of the SZ effect alone. This is insufficiently precise for many cosmological applications given the small samples that are currently available, and so auxiliary datasets must be used to help break the degeneracies and provide better determinations of the mass. Fortunately, large, detailed catalogues of clusters detected through X-ray observations exist (e.g. Böhringer *et al.* [2007]; Piffaretti *et al.* [2010]), for which a relatively low-scatter scaling relation between X-ray luminosity and cluster radius makes improved cluster size determination possible [Planck Collaboration, 2011b].

Contamination also poses a problem for SZ observations. At low frequencies, radio point sources are the main contaminant, and tend to 'fill-in' the SZ decrement, causing a systematic underestimate of its amplitude [White & Majumdar, 2008]. This signal is spatially correlated with cluster positions, and is presumably caused by radio emission from galaxies embedded in the cluster. Such sources tend to have relatively steep spectra, and so can be removed by an appropriate component separation procedure if maps are available at multiple frequencies [Tegmark & de Oliveira-Costa, 1998; Planck Collaboration, 2011c].

At higher frequencies, unresolved dusty (IR) galaxies and galactic dust emission are more problematic [White & Majumdar, 2008]. These are typically expected to be uncorrelated with the positions of clusters, and so are treated as a diffuse component to be removed (see, however, Addison *et al.* [2012] for an estimate of the thermal SZ/cosmic IR background cross-correlation). Finally, primary CMB anisotropies can be confused with clusters, and must therefore also be removed. If multi-frequency observations are available, distinguishing the thermal SZ effect from the primary CMB is relatively straightforward, owing to their different spectral dependences. This is not the case for the kinematic SZ effect [Aghanim *et al.*, 2001], and rather more sophisticated methods must be used to separate the signals.

As SZ observations become more sensitive, other clusters themselves will become an important contaminant. At the moment, it is sufficient to treat most clusters as being independent, isolated objects, and to simply discard or flag those which overlap. In order to construct catalogues which number in the thousands of objects, however, a robust method of disentangling the contributions from many partially-overlapping clusters, with a range of masses, angular sizes and redshifts, will be required. Even in existing catalogues, a few nearby clusters cover large regions of the sky, and thus contaminate the signals of objects behind them.

5.1.2 Extracting the KSZ effect signal

The kinematic SZ effect provides a way of measuring peculiar velocities out to high redshift. Other methods of reconstructing the cosmic velocity field rely on distance indicators, such as the Tully-Fisher or Faber-Jackson relations for galaxies. Observational errors on these measurements scale poorly with distance, effectively limiting this type of peculiar velocity survey to low redshift [Watkins *et al.*, 2008]. The KSZ effect has no such problem, as a distance measurement is not required to estimate the velocity.

Still, extraction of the KSZ effect from CMB maps is a far from trivial task. As discussed in Section 1.3.5, the temperature change induced by the KSZ effect has a flat spectral dependence, and so it cannot be separated from the primary CMB signal (which is also spectrally flat) using multi-frequency data, as the thermal SZ effect can. The different angular scalings of the CMB and KSZ power can be used to separate them in a statistical sense (i.e. by measuring their angular power spectra, c.f. Eq. 4.3 and Dunkley *et al.* [2013]), but this cannot be done for individual clusters. Furthermore, there is an absolute degeneracy between peculiar velocity and optical depth, τ, which must be broken somehow by an independent measurement of τ [Sehgal *et al.*, 2005].

In the following, I will briefly summarise a number of methods for statistically extracting the KSZ effect.

Harmonic-space template fitting: CMB analyses can jointly fit a KSZ template along with other templates in harmonic (ℓ) space (e.g. Dunkley *et al.* [2013]). The KSZ angular power spectrum, $\ell(\ell+1)C_\ell$, appears to be relatively flat at high ℓ, where the thermal SZ spectrum is also relatively flat [Dunkley *et al.*, 2013]. Experiments with multiple frequency channels are therefore required to definitively distinguish between the TSZ and KSZ effects.

Correlation with galaxy clusters: The gas distribution in galaxy clusters can be modelled, to an approximation, by a smooth, spherical electron density profile. This can be used to derive a projected KSZ template. The CMB sky signal can then be correlated with cluster pointings using this template. Some studies do not use templates, instead assuming that the clusters are unresolved and the whole cluster SZ contribution is integrated into a single pixel [Kashlinsky *et al.*, 2009; Hand *et al.*, 2012]. A number of different types of cluster catalogue can be used to provide the cluster pointings (and, potentially, the parameters for their individual KSZ profiles):

- *X-ray catalogues*: These contain relatively large samples of clusters (the biggest have 300–500) and have good estimates of cluster mass/radius, but are typically X-ray flux/luminosity limited, so a range of cluster masses are probed, and not just the most massive. Larger compilation catalogues exist (e.g. Piffaretti *et al.* [2010]), but these have inhomogeneous selection functions.

- *SZ catalogues*: Small-scale CMB experiments are now able to make blind detections of SZ clusters, resulting in mass-limited samples. However, only around 200 clusters have been detected in this way to date, most of them at the very high mass end of the halo mass function [Planck Collaboration, 2011a; Reichardt *et al.*, 2013; Hasselfield *et al.*, 2013]. Their mass/radius can be determined from follow-up observations using various scaling relations, depending on the follow-up method. Some of these scaling relations are discrepant with one another, or poorly calibrated (e.g. Rodriguez-Gonzalvez *et al.* [2012]).

- *Luminous galaxy cluster catalogues*: Luminous galaxies (e.g. Brightest Cluster Galaxies or Luminous Red Galaxies) can be used to trace clusters and galaxy groups. Large samples of these (tens of thousands) have been found in galaxy redshift surveys, over a wide range of redshift and cluster/group mass [Eisenstein *et al.*, 2001; Koester *et al.*, 2007]. The number and separation of neighbouring galaxies can also be used to provide cluster mass and radius information through cluster richness scaling relations [Draper *et al.*, 2012].

Correlation with large galaxies: Galaxies are thought to be surrounded by coronae of ionised gas, the Warm-Hot Intergalactic Medium (WHIM). Though the gas is not in galaxies themselves, the WHIM should nevertheless be correlated with large galaxies [Lavaux *et al.*, 2012]. By correlating galaxy positions (plus an appropriate template for the KSZ profile of each galaxy) with a CMB map, the KSZ signal can be extracted.

Pairwise correlations: Clusters/galaxies can be cross-correlated with a CMB sky map in a pairwise manner. This is a simple extension of the correlation methods listed above, except rather than attempting to measure the peculiar velocities of single objects, the relative velocities of pairs of objects is estimated, providing a more or less direct measurement of pairwise velocity statistics such as $v_{12}(r)$ [Hand *et al.*, 2012].

KSZ tomography: Shao *et al.* [2011] propose a KSZ/galaxy redshift cross-correlation method to extract the KSZ signal tomographically. Spectroscopic galaxy redshift surveys can be used to reconstruct the 3D density field, which can then be used to reconstruct the 3D velocity field by using the continuity equation in linear perturbation theory, Eq. 1.17. By cross-correlating CMB maps with a density-weighted estimator of the 3D velocity field, it should then be possible to extract the KSZ contribution in a given redshift bin.

5.1.3 Peculiar velocity statistics

In this section, I will summarise a number of statistics of the velocity field. Most of the methods listed in the previous section depend on such statistics to reliably extract the KSZ signal; an appropriate choice of statistic can be used to remove uncorrelated, non-KSZ contributions, and enhance the signal-to-noise ratio of a detection, for example.

Bulk flows: Most studies of coherent large-scale (bulk) flows consider only the dipole moment of the velocity field (e.g. Strauss & Willick [1995]; Kashlinsky *et al.* [2009]). This can be found simply by fitting a dipole to the velocity distribution over the sky while accounting for the peculiar velocity of the observer. Failing to include higher multipole moments of the velocity field in the fit can lead to incorrect estimation of the dipole [Macaulay *et al.*, 2012].

Moments of the velocity field: The velocity field can be expanded in a series of multipole moments about the observer, $v_i(\vec{r}) = U_i + U_{ij}r_j + U_{ijk}r_ir_j + ...$ (dipole, shear, octupole, etc.). Each moment consists of a number of independent components (labeled p, q), with the covariance between them given by [Macaulay *et al.*, 2012]

$$\sigma^{(v)}_{pq} = \frac{f^2}{2\pi^2} \int_0^\infty P(k) W^2_{pq}(k) dk, \tag{5.2}$$

where W_{pq} is a window function that depends on the geometry of the peculiar velocity survey. Given weighted measurements of the line-of-sight velocities in a catalogue, the moments of the measured velocity field can be computed and compared with theory to produce cosmological constraints (mainly on the matter power spectrum).

RMS peculiar velocity: The RMS peculiar velocity, σ_v, is an integral of the matter power spectrum convolved with a window function that smooths out power below cluster scales [Watkins, 1997],

$$\sigma^2_v = \frac{1}{3} \frac{H_0^2 \Omega_0^{1.2}}{2\pi^2} \int_0^\infty P(k) W^2(k, R) dk. \tag{5.3}$$

A likelihood for a catalogue of velocity measurements can be written down using this statistic [Watkins, 1997]. Since σ^2_v is a function of the matter power spectrum, sampling from the likelihood will give constraints on the cosmological parameters that $P(k)$ depends on.

Full velocity covariance matrix: Peculiar velocities are correlated over large distances. The velocity covariance for a pair of objects n, m is given in linear theory by [Macaulay *et al.*, 2012]

$$\sigma^{(v)}_{mn} = \frac{\kappa(z_m)\kappa(z_n)}{2\pi^2} \int_0^\infty P(k) f_{nm}(k) dk, \tag{5.4}$$

where f_{nm} is a window function that depends on the separation and orientation of the pair [Ma *et al.*, 2011], and $\kappa(z) = H(z)f(z)/(1+z)$. As before, one can write down a likelihood for a given survey using this statistic [Macaulay *et al.*, 2012],

$$\log \mathcal{L} \sim -S_m \left[(\sigma^{(v)}_{mn})^2 + (\sigma^{(e)}_{mn})^2 \right]^{-1} S_n, \tag{5.5}$$

where $\sigma^{(e)}_{mn}$ is the error covariance matrix, and $S = \hat{r} \cdot \vec{v}$ is the line-of-sight velocity.

Pairwise streaming velocity/momentum: The pairwise velocity $\vec{v}_{12}(r)$ quantifies the fact that overdensities in the matter field will tend to fall towards one another [Peebles, 1980]. It is a function of object separation r, and is related to the matter correlation function $\xi(r)$ by

$$\begin{aligned} \vec{v}_{12} &= \frac{\langle (\vec{v}_1 - \vec{v}_2)(1+\delta_1)(1+\delta_2) \rangle}{1 + \xi(r)} \qquad (5.6) \\ &\propto \langle v_1 \delta_2 - v_2 \delta_1 \rangle \qquad (5.7) \end{aligned}$$

Nonlinear effects become important at small r, which have been modelled using an analytic approximation as [Ferreira *et al.*, 1999],

$$\begin{aligned} v_{12}(r) &= -\frac{2}{3} H r f \bar{\xi}(r) [1 + \alpha \bar{\xi}(r)] \qquad (5.8) \\ \bar{\xi}(r) &= (3/r^3)[1 + \xi(r)]^{-1} \int_0^r \xi(x) x^2 dx. \qquad (5.9) \end{aligned}$$

An estimator using only line-of-sight velocities was given by Ferreira *et al.* [1999]. This statistic can be measured from catalogues with position, velocity and mass/density information [Hand *et al.*, 2012], and the shape and normalisation of v_{12} can be used to constrain cosmological parameters. An example of v_{12} for a standard ΛCDM cosmology is plotted in Fig. 5.1.

Pairwise velocity dispersion: Bhattacharya & Kosowsky [2007] give an expression for the dispersion about the mean pairwise velocity v_{12},

$$\sigma^2_{12}(r) = 2 \frac{\langle \sigma^2_v(R) \rangle + \xi^{\rm lin}(r) \langle b \sigma^2_v(R) \rangle}{1 + b^2 \xi^{\rm lin}}, \tag{5.10}$$

where R is the characteristic smoothing scale for clusters (down to some lower

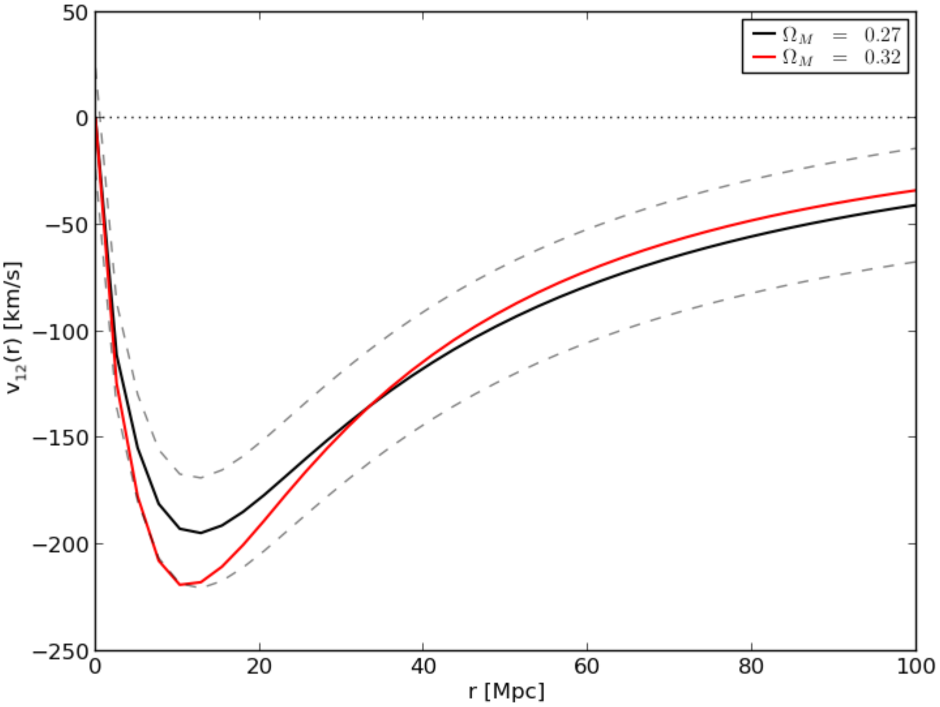

Figure 5.1: Pairwise velocity statistic, $v_{12}(r)$, for two different values of Ω_m (all other parameters are the standard WMAP7 best-fit values). The dashed lines are theoretical cosmic variance intervals from linear theory, $\sigma_{12}(r)$.

mass limit). This can be measured from the same datasets as the mean pairwise velocity, and is essentially the cosmic variance for $v_{12}(r)$ in each r bin.

Line-of-sight velocity pdf: An expression for the redshift-dependent pdf of the line-of-sight peculiar velocity is given by [Bhattacharya & Kosowsky, 2007]

$$f(v,z) = \frac{\int dM M n(M|\delta) p(v|M,\delta)}{\int dM M n(M|\delta)}. \tag{5.11}$$

This expression can be rewritten in terms of the halo mass function $n(M)$ and a Gaussian model for the velocities [Bhattacharya & Kosowsky, 2007],

$$p(v|M,\delta) \sim \frac{1}{\sigma_v(M)} \exp\left(-\frac{(3v)^2}{\sigma_v^2(M)}\right). \tag{5.12}$$

$f(v,z)$ can be measured from a velocity catalogue by plotting the relative frequency of catalogue objects in bins of velocity and redshift. For high-mass cluster samples, this statistic should inherit some of the sensitivity of $n(M)$ to (e.g.) σ_8 and Ω_m due to its exponential cut-off at high masses.

5.1.4 Effective KSZ extraction

I will now suggest a set of properties that a successful KSZ method is likely to require, in light of the discussion in the previous sections. These are:

1. Correlation of the CMB signal with large galaxy/cluster catalogues that provide information about cluster properties.
2. A realistic model of the KSZ signal from clusters that depends on basic cluster properties.
3. Accurate and complete modelling of contaminating signals.
4. Accurate statistical error estimation.
5. Use of a peculiar velocity statistic that uses as much information as possible from the data, and which does not depend on a complicated selection function.

Property (1) ensures that adequate prior information on the position and size of a cluster is available. If the position and size can be fixed, computational resources can be wholly devoted to accurately characterising the signal from the cluster rather than trying to find where it is on the sky. Prior information on cluster mass, temperature, and/or pressure are is also necessary to break the strong degeneracy with cluster optical depth described by Sehgal *et al.* [2005].

Property (2) is related to (1). Because prior information on the clusters tends to be sparse or poor in quality, it is often necessary to construct a model that takes only basic cluster properties and uses them to infer required (but unavailable) information. A particularly useful derived quantity is the spatial profile of the

KSZ effect from a cluster. This describes the expected spatial correlation of the KSZ signal between nearby pixels, which makes it possible to distinguish it from other effects with different or no spatial correlation. By using a simple parametric model with few parameters, stronger constraints can be obtained; if a completely arbitrary spatial model was used instead, the signal would be poorly constrained as there would be too much model freedom.

Property (3) is necessary to ensure that other signals are not mistaken for the KSZ effect. As discussed above, various known signals are spatially or spectrally correlated with KSZ, and so a failure to properly model them could result in their being erroneously folded into the estimated KSZ signal. Similarly, property (4) is required to mitigate the risk of accidentally overestimating the significance of a KSZ detection (as may have been the case in Kashlinsky *et al.* [2009]), which could lead to incorrect physical conclusions being drawn.

Property (5) acknowledges that detections of the KSZ effect due to single clusters are unlikely to be possible for the time being, on account of the weakness of the KSZ signal. As such, a successful extraction method will need to combine the signals from many clusters in a well-defined, statistical manner if a significant detection is to be obtained. It makes sense to base these methods on a peculiar velocity statistic, since these are directly related to interesting cosmological quantities.

A number of statistics mentioned above are functions of density-weighted velocities, because the KSZ signal itself is approximately density-weighted (as it depends on the optical depth, $\tau \propto \int n_e dl$, and $n_e \propto \delta$). Other signals are also density-weighted (e.g. the TSZ effect), but should be uncorrelated with the velocity. These statistics are useful for *detecting* the KSZ effect (e.g. Hand *et al.* [2012]), but are more difficult to extract cosmological information from because they depend on the selection function of a cluster survey. The selection function for big X-ray compilation catalogues like MCXC is typically very inhomogeneous, and so will be difficult to model accurately. The Planck TSZ cluster sample [Planck Collaboration, 2011a] could be used instead, as it has a more homogeneous selection function, but it contains far fewer clusters making it more difficult to gain enough statistical power to even detect the KSZ signal.

Of the statistics that are not density-weighted, some are only one-point statistics, and so effectively throw away useful information about correlations between the velocities of different clusters. Others are defined with respect to the position of the observer rather than being directly linked to the broader statistical properties of the matter field, and so are more difficult to connect with theory. The 'full velocity correlation matrix' statistic avoids most of these problems, and so it is this that I will concentrate on in later sections.

With this list of desirable properties in hand, I will now describe an extraction method that attempts to satisfy all of them to some extent.

5.2 SZ extraction with a CMB Gibbs sampler

In this section, I outline a fully Bayesian approach to the problem of extracting accurate SZ amplitudes from a generic set of foreground-contaminated CMB temperature maps at multiple frequencies, given prior information about the position of the clusters and a model for the spatial distribution of their SZ signal.

Simply stated, the idea behind this method is to: (a) model every contribution to the sky maps; (b) estimate the joint posterior distribution for all parameters of this full model; and then (c) exactly marginalise over everything but the SZ amplitudes to produce estimates of the SZ signal. This automatically takes into account the effects of parameter degeneracies, and provides statistically rigorous estimates of uncertainty. Additionally, by explicitly writing down the 'full model', we can most clearly see where various velocity statistics should be inserted.

While in outline this 'comprehensive' approach to modelling the sky may first appear complicated and computationally challenging, the fundamental method

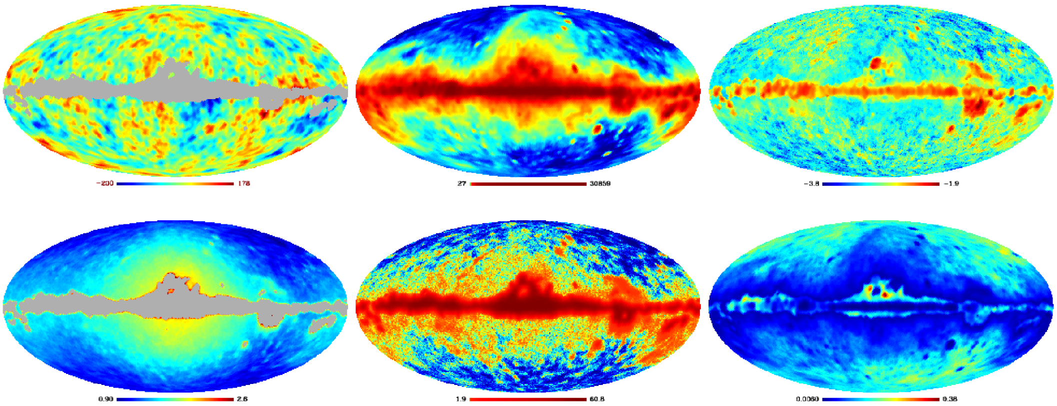

Figure 5.2: An example of CMB sky map components separated using Commander, taken from Dickinson *et al.* [2009]. Shown are the primary CMB, galactic foregrounds, and foreground spectral indices (top), and RMS error maps for each of these (bottom).

has been successfully applied to CMB component separation before, using a Gibbs sampling code called *Commander* [Eriksen *et al.*, 2004] (see Fig. 5.2 for an example set of marginalised maps of various components made by Commander.) Furthermore, I argue that a comprehensive treatment is *necessary* to avoid some of the problems with existing extraction methods that were discussed above; while the use of a model with many parameters will necessarily increase the error bars on individual cluster SZ measurements, it will help to prevent biases due to contaminating signals and overestimates of detection significance.

5.2.1 The sky model

In this section, I will describe the basic sky model used by Commander [Jewell *et al.*, 2004; Wandelt *et al.*, 2004; Eriksen *et al.*, 2004, 2008]. The value of each pixel on the sky, **d**, is taken to have the form

$$\begin{aligned}\mathbf{d}(\nu) &= \mathbf{s} + \mathbf{n} \\ &= \mathbf{B}(\nu) \sum_{i=1}^{N} \mathbf{G}_i(\nu) \mathbf{T}_i \mathbf{a}_i + \mathbf{n}(\nu), \end{aligned} \tag{5.13}$$

where $\mathbf{s}$ is the signal and $\mathbf{n}$ is the noise. The sum is over individual physical components of the sky model, which include the primary CMB, the SZ effect, galactic synchrotron emission, and so forth. The meanings of each of the terms in this expression are as follows:

Beam, B: The sky signal is convolved with an instrumental beam. The form of the beam convolution operator depends on the experiment in question, and will typically be a function of frequency. In what follows, symmetric beams are assumed, as these make efficient harmonic space (de-)convolution possible.

Frequency spectrum, G: Each component has a characteristic frequency dependence, $\mathbf{G}_i(\nu)$, that can be either a fixed function of frequency, or a parametrised spectral model with parameters $\boldsymbol{\theta}$. The way that $\mathbf{G}_i$ is modelled depends on the component; some have spatially-varying frequency spectra, for example, so spectral model parameters may be sampled per-pixel.

Amplitude, a: The component amplitudes are the quantities which we are primarily interested in sampling. What is meant by 'component amplitude' depends on how the projection operator is defined; for example, if a component is allowed to vary per-pixel, then each pixel will have its own amplitude. If the spatial variation of a component is instead defined in harmonic space, as the CMB's is, then the amplitudes will be spherical harmonic coefficients instead. If the component is defined by a map template, then there will only be one overall amplitude for the whole template. In what follows, the amplitudes $\mathbf{a}_i$ are assumed to be Gaussian. Optionally, a signal covariance matrix $\mathbf{S}_i$ may also be defined. This is usually done in cases where the signal covariance contains useful information, such as for the CMB (where it gives the CMB power spectrum, C_ℓ).

Projection operator, T: This projects the amplitudes for a component onto pixels on the sky, depending on how the spatial variation of the component is modelled. If the component model defines an amplitude per pixel, the projection operator is, trivially, the identity matrix – there is a one-to-one correspondence between pixel and amplitude. If the amplitudes given are for the spherical harmonic coefficients of the component, $a_{\ell m}$, the projection operator will consist of a set of pixelised spherical harmonics, $Y_{\ell m}(\hat{n}_p)$ (where $\hat{n}_p$ is the direction of each pixel on the sky). If the amplitude is for a map template, then the projection operator will be the template itself.

Noise, n: This depends on the noise properties of the experiment. The noise in each pixel is typically modelled as a Gaussian random variable with covariance, $\mathbf{N}$, that depends on the scan strategy of the experiment (i.e. pointings on the sky that are observed more frequently should have lower noise).

I conclude this section with a brief note on notation. It will often be convenient to bundle together quantities for all sky components into one object. For example, the individual component amplitude vectors, $\mathbf{a}_i$, can be put into a single symbolic 'block' vector, $\mathbf{a} = (\mathbf{a}_0, \mathbf{a}_1, \ldots, \mathbf{a}_N)^{\mathrm{T}}$, and the component covariance matrices $\mathbf{S}_i$ (if defined) into a symbolic block diagonal matrix, $\mathbf{S} = \mathrm{diag}(\mathbf{S}_0, \mathbf{S}_1, \ldots, \mathbf{S}_N)$.

5.2.2 Sampling scheme

The problem now is to estimate the amplitudes for all of the components (and any auxiliary parameters, $\boldsymbol{\theta}$, such as spectral model parameters) from data. As discussed in Section 1.4.3, Gibbs sampling provides a way of obtaining samples from the full joint posterior distribution for all of the model parameters, $P(\mathbf{a}, \mathbf{S}, \boldsymbol{\theta}|\mathbf{d})$, by successively sampling from their conditional distributions.

The detailed derivation of a Gibbs scheme for a sky model consisting of primary CMB anisotropies and foregrounds is given in Eriksen *et al.* [2004] and Eriksen *et al.* [2008]. The scheme has three main steps:

$$\begin{aligned} \mathbf{a}^{k+1} &\leftarrow P(\mathbf{a} \mid \mathbf{S}^k, \boldsymbol{\theta}^k, \mathbf{d}) \\ \mathbf{S}^{k+1} &\leftarrow P(\mathbf{S} \mid \mathbf{a}^{k+1}, \boldsymbol{\theta}^k, \mathbf{d}) \\ \boldsymbol{\theta}^{k+1} &\leftarrow P(\boldsymbol{\theta} \mid \mathbf{a}^{k+1}, \mathbf{S}^{k+1}, \mathbf{d}) \end{aligned} \tag{5.14}$$

The first samples the component amplitudes, the second samples the component covariances, and the third samples non-amplitude sky model parameters (which would be broken up into multiple sub-steps in practise).

To see how these conditional distributions can be sampled from in practise, take as an example the problem of estimating the CMB power spectrum from foreground-contaminated data. In this case, the only signal covariance that we are interested in is the CMB power spectrum itself, $S_{\mathrm{CMB}} = C_\ell \delta_{\ell\ell'} \delta_{mm'}$. By applying Bayes' theorem, each conditional distribution can be rewritten as a likelihood multiplied by a number of conditional/prior factors, most of which do not depend on the data, or act only as normalisation constants. This results in the following proportionality relations [Eriksen *et al.*, 2008]:

$$\begin{aligned}
P(\mathbf{a}|C_\ell, \boldsymbol{\theta}, \mathbf{d}) &\propto P(\mathbf{d}|\mathbf{a}, C_\ell, \boldsymbol{\theta}) P(\mathbf{a}|C_\ell) \\
&\propto \exp\left(-\frac{1}{2}(\mathbf{d}-\mathbf{s})^T N^{-1} (\mathbf{d}-\mathbf{s})\right) P(\mathbf{a}|C_\ell) \qquad (5.15) \\
P(C_\ell|\mathbf{a}, \boldsymbol{\theta}, \mathbf{d}) &\propto P(C_\ell|\mathbf{a}_{\mathrm{CMB}}) \\
&\propto \exp\left(-\frac{1}{2}\mathbf{s}_{\mathrm{CMB}}^{\mathrm{T}} S_{\mathrm{CMB}}^{-1} \mathbf{s}_{\mathrm{CMB}}\right) \Big/ \sqrt{|S_{\mathrm{CMB}}|} \\
&\propto \prod_\ell \exp\left(-\frac{2\ell+1}{2}\frac{\sigma_\ell^2}{C_\ell}\right) \Big/ C_\ell^{\frac{2\ell+1}{2}} \qquad (5.16) \\
P(\boldsymbol{\theta}|\mathbf{a}, C_\ell, \mathbf{d}) &\propto P(\mathbf{d}|\mathbf{a}, C_\ell, \boldsymbol{\theta}), \qquad (5.17)
\end{aligned}$$

where $\mathbf{d}$ is the data, $\mathbf{s}$ is the total sky signal (from the model given by Eq. 5.13), N is the noise covariance matrix, and

$$\sigma_\ell = \frac{1}{2\ell+1} \sum_{m=-\ell}^{\ell} |a_{\ell m}|^2 \qquad (5.18)$$

is the angular power spectrum of the current realisation of the CMB sky signal [Eriksen *et al.*, 2008]. The first proportionality in Eq. 5.16 comes from the fact that if $\mathbf{a}_{\mathrm{CMB}}$ (which is part of the block vector $\mathbf{a}$) is given, the CMB signal $\mathbf{s}_{\mathrm{CMB}}$ is given, and so no further information is required to determine C_ℓ.

Sampling from these conditional distributions is computationally tractable. Eq. 5.15 is a multivariate Gaussian, which one can sample from by solving the linear equation [Eriksen *et al.*, 2008]

$$[S^{-1} + N^{-1}]\mathbf{s} = N^{-1}\mathbf{d} + S^{-\frac{1}{2}}\omega_0 + N^{-\frac{1}{2}}\omega_1 \tag{5.19}$$

for $\mathbf{s}$, where (ω_0, ω_1) are vectors of Gaussian random numbers with zero mean and unit variance, and $\mathbf{s}$ is a single sample of the full sky signal. Eq. 5.13 can be used to rewrite Eq. 5.19 in terms of the component amplitudes, $\mathbf{a}$, rather than the full sky signal, so the amplitudes can be sampled directly and then used to reconstruct $\mathbf{s}$ [Eriksen *et al.*, 2008]. Since the dimensionality of the problem is typically high for CMB analysis (full-sky CMB maps usually have millions of pixels), solving this equation can be computationally intensive. Commander uses the *conjugate gradient* method to solve the system in Eq. 5.19, which can be made relatively efficient by preconditioning the system [Eriksen *et al.*, 2004].

Eq. 5.16 is the inverse Gamma distribution, which can also be directly sampled from in a relatively simple manner. The way in which Eq. 5.17 is sampled from will depend on the number and form of the additional model parameters $\boldsymbol{\theta}$. Inversion sampling (where the cumulative distribution is found directly by integrating the likelihood, and then used to draw samples) may be efficient if there is only one parameter; for multi-dimensional problems, a Metropolis-Hastings MCMC method may be used instead.

5.2.3 Adding an SZ component

In this section, I outline the additions to the Commander Gibbs sampling scheme defined above that are required to also extract cluster TSZ and KSZ signals from CMB sky maps.

5.2.3.1 TSZ/KSZ spatial templates

A spatial template for the SZ signal is required in order to define a projection operator for the SZ component. Expressions for the TSZ and KSZ emission from a single cluster were given in terms of line-of-sight integrals of the electron pressure and density profiles in Eqs. 1.66 and 1.67. While these profiles can in principle be measured, or at least estimated, using auxiliary data, in reality only a few basic properties of the cluster gas are likely to be known from observations. As such, it is necessary to construct a simplified model that depends on these properties to make progress.

Fortunately, the pressure and temperature of cluster gas appear to follow 'universal' scalings with radius, at least to a first approximation [Komatsu & Seljak, 2001]. I adopt the universal pressure profile of Arnaud *et al.* [2009][1],

$$P_e(x) = \bar{P}_{500}(z) \frac{P_0 (M_{500}/M_\star)^{\alpha_p(x)}}{(c_{500}x)^\gamma [1 + (c_{500}x)^\alpha]^{\frac{\beta-\gamma}{\alpha}}}, \tag{5.20}$$

where $x = r/R_{500}$ and $M_\star = 3 \times 10^{14} h^{-1} M_\odot$. The pressure at R_{500} in a fiducial (gravity-only) self-similar model is defined as [Nagai *et al.*, 2007]

$$\bar{P}_{500}(z) = 1.65 \times 10^{-3} h(z)^{\frac{8}{3}} (M_{500}/M_\star)^{\frac{2}{3}} h^2 \text{ keVcm}^{-3}, \tag{5.21}$$

and the running of the mass scaling with radius is well-fit by

$$\alpha_p(x) = 0.22 \left(1 - \frac{8x^2}{1 + 8x^3} \right). \tag{5.22}$$

The profile normalization and shape parameters have best-fit values of

$$[P_0, c_{500}, \gamma, \alpha, \beta] = [8.403 h^{-\frac{3}{2}}, 1.177, 0.3081, 1.0510, 5.4905]. \tag{5.23}$$

---

[1] Quantities with subscript 500 are evaluated at the radius where the cluster density is 500× the background cosmological density.

These were calibrated using the REXCESS sample of 33 local X-ray clusters at small radii [Böhringer *et al.*, 2007], and the results of hydrodynamic simulations at large radii [Arnaud *et al.*, 2009]. The pressure profile is assumed spherically symmetric, and effects due to the relativistic motions of electrons have been neglected[1].

The profile is fully specified once the characteristic mass, radius, and redshift of a cluster have been determined. Arnaud *et al.* [2009] show that the universal pressure profile fits all clusters in the REXCESS sample to better than 25% at radii greater than 0.2 R_{500}. At smaller radii, inside the cluster core, they find the dispersion to be greater, deviating from the universal relation by up to a factor of four, depending on how morphologically disturbed the cluster is. This is likely to lead to a sizeable scatter in the recovered SZ amplitude, but given the lack of more detailed auxiliary data on the clusters, it is the best we can do.

The KSZ effect depends on the electron number density, n_e, rather than the electron pressure. It would be possible to use a standard dark matter halo profile (such as the NFW profile of Navarro *et al.* [1997]) as a proxy for n_e, but these often have divergences in mass or central density that can be awkward to deal with. Instead, I will use the universal temperature profile given by Loken *et al.* [2002],

$$T(r) = 11.2 \left(\frac{R_{500} h}{\text{Mpc}} \right)^2 \left(1 + 0.75 \frac{r}{R_{500}} \right)^{-1.6} \text{ keV}, \tag{5.24}$$

in combination with the ideal gas law to estimate $n_e = P_e / k_B T_e$. This has the virtue of directly linking the TSZ and KSZ profiles through a dependence on a common electron distribution model, and gives a smooth profile that is simple to work with numerically, but again introduces some scatter.

Example TSZ and KSZ profiles are plotted in Fig. 5.3. TSZ typically dominates KSZ at the centre of the cluster by around an order of magnitude, but the

---

[1] Relativistic corrections to the electron energy distribution can cause $\sim 1-10\%$ corrections to the thermal SZ intensity in the hottest clusters [Itoh *et al.*, 1998; Challinor & Lasenby, 1999].

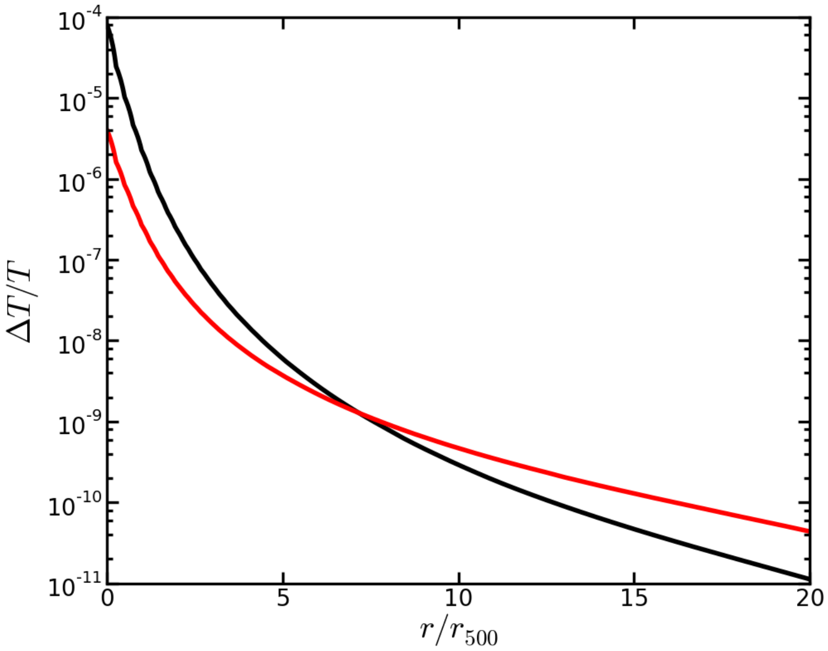

Figure 5.3: Thermal (black) and kinematic (red) SZ radial profiles calculated using the model described in Section 5.2.3.1. I have used illustrative values of $v = 200$ kms^{-1} and $\nu = 150$ GHz here.

KSZ profile falls off less rapidly with radius. As a result, the KSZ flux integrated over the whole cluster can be of a similar size to the TSZ, depending on the cluster's peculiar velocity.

5.2.3.2 TSZ/KSZ amplitudes

Separate amplitudes, $a_{\rm TSZ}$ and $a_{\rm KSZ}$, are defined for the TSZ and KSZ effects for each cluster, introducing $2 \times N_{\rm cl}$ new amplitudes into the block amplitude vector $\mathbf{a}$ that was defined at the end of Section 5.2.1. Each amplitude represents an overall scaling of the expected TSZ or KSZ profile defined in Section 5.2.3.1, and is sampled as part of the joint amplitude sampling step (step 1 of Eq. 5.14).

5.2.3.3 SZ frequency spectrum

The spectral functions for the TSZ and KSZ signals (given in Eqs. 1.66 and 1.67) are fixed and constant over the whole sky, so $\mathbf{G}$ for the two effects is trivial.

5.2.3.4 KSZ covariance matrix

Because the KSZ effect is proportional to peculiar velocity, the KSZ signals of clusters are correlated over the sky, since the velocities themselves are correlated. The correlation can be modelled by adding a signal covariance matrix for the KSZ effect, based on the linear theory expression that was given in Eq. 5.4. This covariance matrix can be used as the 'velocity statistic' that I argued is necessary for a successful KSZ extraction method (see Section 5.1.4). It depends on an integral over the matter power spectrum, as well as factors of the linear growth rate and expansion rate. It is possible to constrain these quantities by sampling the covariance matrix using Commander. All that is required is a suitable parametrisation of these functions (e.g. in terms of cosmological parameters like Ω_m), and a Gibbs step to obtain samples of the matrix (which would be a sub-step of the second Gibbs step in Eq. 5.14, where the block signal covariance matrix **S** is sampled).

As an example, consider a very basic parametrisation that has only the overall amplitude of the matter power spectrum, $A_{\rm PS}$, as a free parameter. This can be written down by replacing $P(k) \mapsto A_{\rm PS} P_{\rm fid}(k)$ in Eq. 5.4, where $P_{\rm fid}(k)$ is a fiducial power spectrum. In the case where only the CMB and KSZ signal covariances are of interest, step 2 of the Gibbs scheme defined in Eq. 5.14 becomes

$$\begin{aligned} C_\ell^{k+1} &\leftarrow P(C_\ell \mid \mathbf{a}^{k+1}, A_{\rm PS}^k, \boldsymbol{\theta}^k, \mathbf{d}) && (5.25)\\ A_{\rm PS}^{k+1} &\leftarrow P(A_{\rm PS} \mid \mathbf{a}^{k+1}, C_\ell^{k+1}, \boldsymbol{\theta}^k, \mathbf{d}). && (5.26)\end{aligned}$$

As with the other conditional distributions, Eq. 5.26 can be rewritten in terms of the likelihood and some conditional/prior factors, and reduces to

$$\begin{aligned} P(A_{\rm PS} \mid \mathbf{a}, C_\ell, \boldsymbol{\theta}, \mathbf{d}) &\propto P(A_{\rm PS} | \mathbf{a}_{\rm KSZ}) && (5.27)\\ &\propto \exp\left(-\frac{1}{2}\mathbf{s}_{\rm KSZ}^{\rm T} S_{\rm KSZ}^{-1} \mathbf{s}_{\rm KSZ}\right) \Big/ \sqrt{|S_{\rm KSZ}|}\,, && (5.28)\end{aligned}$$

where the KSZ signal $\mathbf{s}_{\mathrm{KSZ}}$ is proportional to the cluster velocity, and S_{KSZ} is proportional to Eq. 5.4 and A_{PS}. This can be rewritten as an inverse gamma distribution in A_{PS}, for which a simple numerical sampling method exists. The extension to more complicated parametrisations of the KSZ signal covariance proceeds analogously.

5.2.3.5 Additional model parameters

The SZ profiles defined in Section 5.2.3.1 are functions of a number of parameters that could also be sampled. For example, the profile shape parameters could be allowed to vary rather than being fixed to the best-fit values given by Arnaud *et al.* [2009]. Spectral parameters that depend on relativistic corrections to the electron energy distribution could also be added [Itoh *et al.*, 1998; Challinor & Lasenby, 1999].

5.3 Applications to simulated data

In this section, I apply the method discussed above to simulated data. The implementation of the method that I used is based on the Commander code described in Eriksen *et al.* [2008]. The modifications set out in Section 5.2.3 were added to this code by Ingunn Wehus, myself and Hans Kristian Eriksen.

The simulations that I consider here are restricted to the TSZ effect alone, without KSZ or galactic foregrounds, and should be considered a first step in validating the SZ extraction method set out in Section 5.2. Some of the modifications to the code that are required to properly extract the KSZ effect have not yet been fully tested, whereas those for the TSZ effect have, hence the restriction to the TSZ-only case here. More detailed (and more realistic) cases, including a validation using simulations of both the TSZ and KSZ effects, will be considered in a future paper.

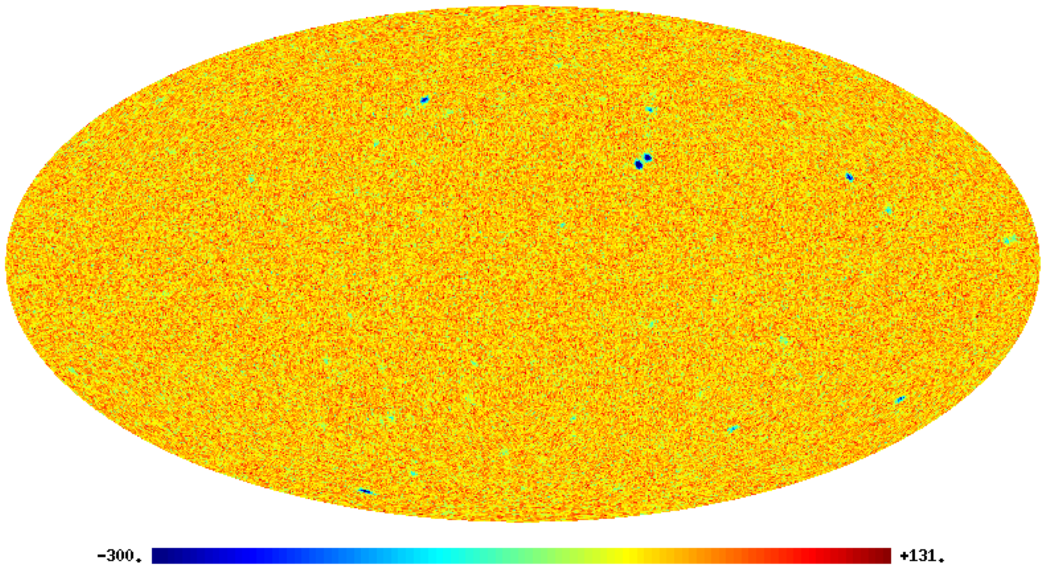

Figure 5.4: Simulated map of the TSZ effect from 314 clusters in the WMAP W band, with WMAP-7 noise characteristics. The TSZ signal is always a temperature decrement at these frequencies, so the clusters show as blue spots. The TSZ flux has been boosted by a factor of 50 here.

Each simulated sky map requires the following to be specified:

- Frequency bands, and bandpasses, for the simulated instrument
- An instrumental beam in each of these bands
- A definition of the noise in each pixel, in each band
- A catalogue of cluster locations, properties, and signal profiles
- An input CMB power spectrum

The cluster SZ profiles are taken to be of the form described in Section 5.2.3.1. The locations and basic properties of the clusters are provided by the MCXC X-ray meta-catalogue [Piffaretti *et al.*, 2010]. The catalogue has been trimmed to remove duplicate entries and some clusters which cover a very large angle on the sky. The latter has been done to reduce computational time; as per Eq. 5.13, part of the sampling process involves a beam convolution with the cluster profiles (given by **T**), which can take a long time for the largest clusters as these have a

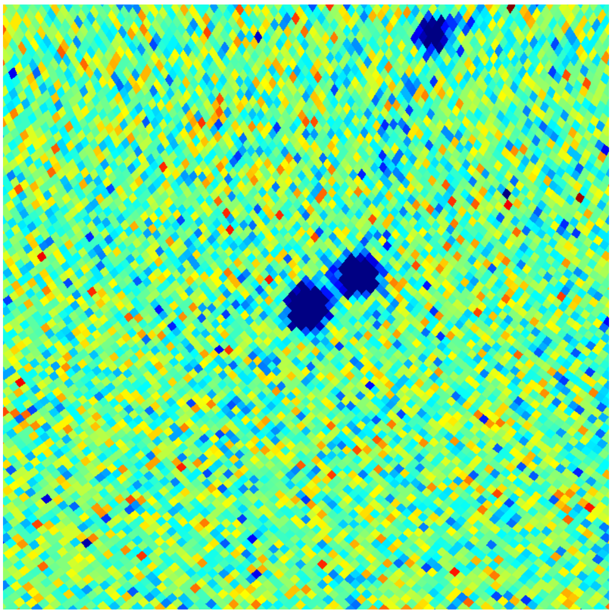

Figure 5.5: A close-up (in a Gnomonic projection) of some of the simulated clusters shown in Fig. 5.4.

large number of pixels. The catalogue used for my tests here contains 314 clusters in total; these are shown in Fig. 5.4

The instrument specification is taken to be the same as that given for the WMAP 7-year data release [Jarosik *et al.*, 2011]. Band specifications, beam profiles, and noise maps are available from the WMAP LAMBDA server [WMAP Collaboration, 2013]; only the Q (40 GHz), V (60 GHz) and W (90 GHz) bands have been used, since the K and Ka bands would be expected to be dominated by galactic synchrotron/free-free emission. In these bands, the WMAP beam has FWHM of between 0.2 – 0.5 degrees, and is approximately Gaussian [Jarosik *et al.*, 2011].

Simulated sky maps are created by first constructing an empty pixel grid on the sphere for each band, using Healpix [Górski *et al.*, 2005]. A Healpix map resolution of $N_{\rm side} = 128$ is used in these simulations. This has been chosen to be lower than the maximum map resolution provided by WMAP ($N_{\rm side} = 512$) for the sake of computational speed – higher resolution maps take considerably longer to process. The CMB signal – a Gaussian random realisation of the WMAP 7-

year best-fit angular power spectrum from Larson *et al.* [2011] – is then added to the maps, as are individual SZ profiles, appropriately scaled with frequency, and with positions and other parameters given by the MCXC catalogue. Galactic foregrounds are not added to the maps, as the purpose here is to provide only a simple validation of the method. The maps are then smoothed using the appropriate instrumental beam, and noise added. A simulated map (without CMB) is shown in Fig. 5.4, and a close-up of several clusters is shown in Fig. 5.5.

The simulated maps that I produced are summarised in Table 5.1. For the purposes of validation, the different contributions to the signal are switched on and off in various combinations, and the SZ signal enhanced by various factors to make up for the relatively low sensitivity and poor frequency coverage of WMAP for SZ extraction (Planck is expected to perform significantly better).

Sim.	**Noise**	**CMB**	**TSZ**
A	✓	–	50×
B	✓	–	10×
C	✓	–	1×
D	✓	✓	50×
E	✓	✓	500×

Table 5.1: Components included in the simulated maps.

I used Commander to produce 3000 samples of the TSZ amplitude, a_i, for all 314 clusters in the simulated maps listed in Table 5.1. Diagnostics showed that the samples were only weakly correlated, and that the chains converged rapidly. In order to assess whether the amplitudes extracted by Commander are biased with respect to the input amplitudes in the simulations, $\hat{a}_i$, I calculated the 'Z scores' (normalised scores), $Z_i = (a_i - \hat{a}_i)/\sigma_i$, for each cluster i, where a_i is the mean TSZ amplitude over 3000 samples, and σ_i is its standard deviation. If Commander is correctly estimating the cluster TSZ amplitudes (to within statistical error), the Z scores should be Gaussian distributed with zero mean and unit variance, $G(0, 1)$. Fig. 5.6 shows a histogram of the Z scores for simulation C, along with a best-fit Gaussian. The mean over all clusters, $\langle Z \rangle$, is slightly biased (by 6.6%),

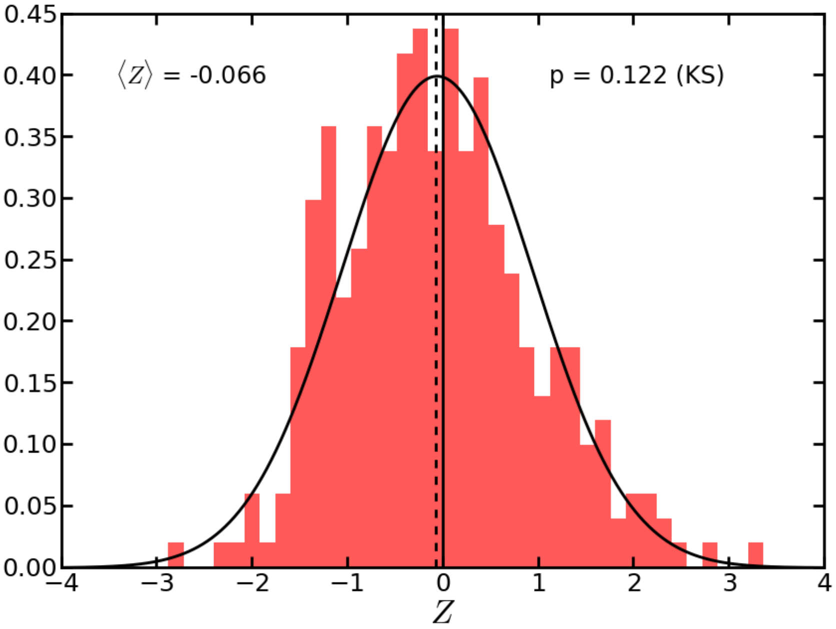

Figure 5.6: Histogram of Z scores for simulation C. The sample mean deviates from its expected value by 6.6% here, but a Kolmogorov-Smirnov test reveals that this is consistent with the method being unbiased.

but this could be due to statistical fluctuations; a Kolmogorov-Smirnov test for similarity with $G(0, 1)$ finds a probability of $p = 0.122$ that the sample is from this distribution, which is consistent with the Commander procedure being unbiased [Nikulin, 2001]. The same result was found for simulations A and B.

Fig. 5.7 shows the distribution of fractional errors, $f_i = \sigma_i/\hat{a}_i$, for simulations A–C (which have noise but no CMB component). The fractional error can be thought of as the reciprocal of the signal-to-noise ratio; $f_i < 1$ is a detection of the SZ signal for a cluster at greater than 68% confidence. For low-resolution WMAP data, it can be seen from Fig. 5.7 that the percentage of high-significance detections is quite low; $\sim 30\%$ of clusters were not detected in simulation A (for which the TSZ signal has been boosted by $50\times$), and only $\sim 1\%$ of clusters were even marginally detected in simulation C (where no boost has been applied).

I will now briefly examine the performance of the method in the presence of a CMB component. Figure 5.8 shows the fractional difference between the best-fit

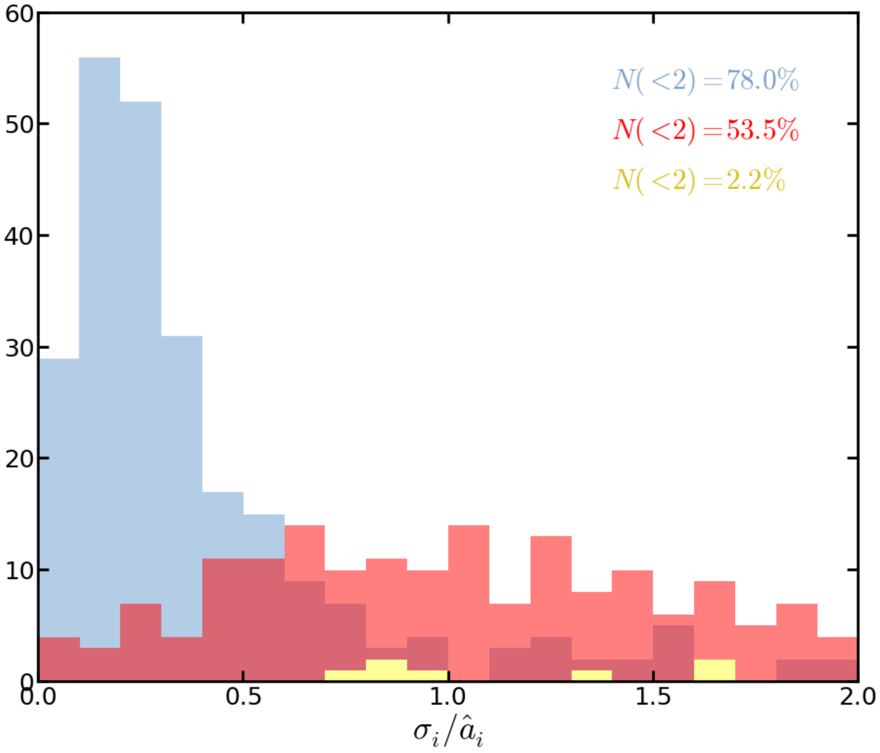

Figure 5.7: The fractional errors, f_i, for the simulations A (blue), B (red), and C (yellow). The coloured labels show the percentage of clusters in each simulation that have $f_i < 2$ (higher f_i are not shown). Only clusters with $f_i \ll 1$ can be considered to have definitely been detected.

TSZ amplitude, a_i, and the input amplitude, $\hat{a}_i$, for simulations A, D and E. The amplitudes for simulation A, which has only noise, are recovered much more reliably than for simulation D, which has a CMB component as well as noise. The recovery for simulation E is comparable to that for simulation A, but E has had its TSZ signal boosted by a factor of ten relative to A and D. The confusion due to the presence of the CMB is therefore a serious effect here. Nevertheless, Fig. 5.8 shows that the deviations are approximately symmetrically-distributed about zero, and so the CMB has not systematically biased the results to any great extent.

There are a number of reasons for this relatively poor performance, both with and without a CMB component. First of all, WMAP is not sensitive enough to

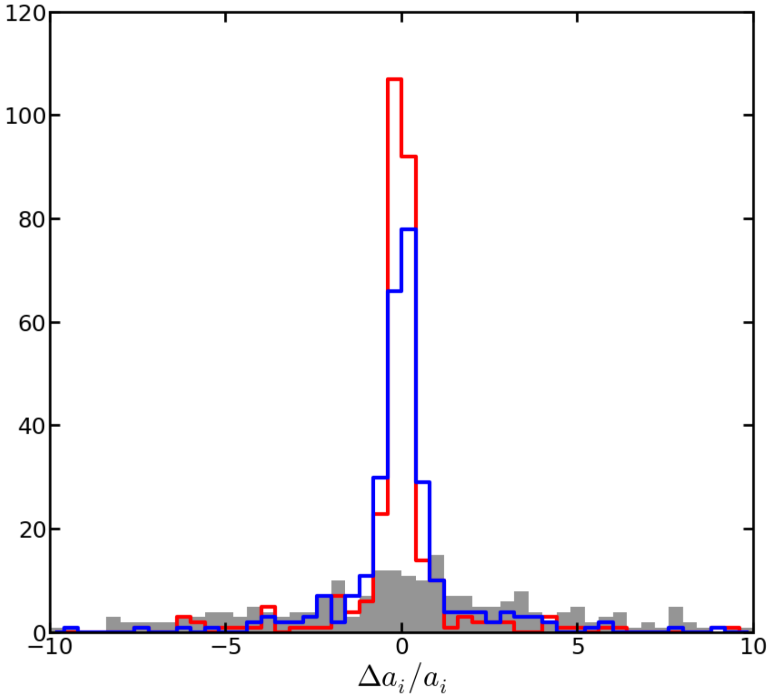

Figure 5.8: Comparison of the deviation of the best-fit TSZ amplitude from the input amplitude, $(a_i - \hat{a}_i)/\hat{a}_i$, for simulations A (red, no CMB), D (grey), and E (blue).

detect the TSZ effect from individual clusters with high confidence; only statistical detections have been made [Hinshaw *et al.*, 2012]. Secondly, its frequency coverage is relatively poor for SZ extraction, with only the initial (low frequency) part of the TSZ spectrum being observed (see Fig. 1.1). An experiment with better frequency coverage would allow the extraction method to exploit distinctive features of the TSZ spectrum such as the null at 217 GHz, and the fact that the TSZ signal is a temperature decrement below the null and an increment above it. Finally, the X-ray catalogue used to locate the clusters has a very different selection function to the TSZ effect, and so many of the clusters in the catalogue are simply not massive enough to be detected via the TSZ effect with current CMB experiments. (As discussed in Section 5.1.1, the amplitude of the TSZ signal is closely related to cluster mass.)

The method's performance can be expected to improve greatly with Planck. The Planck experiment has around an order of magnitude higher sensitivity than WMAP [Lamarre *et al.*, 2010], a greater number of frequency channels over a range of frequencies better suited to SZ extraction, and its own SZ-selected cluster sample [Planck Collaboration, 2011a]. More realistic simulations, with a Planck instrumental set-up, higher-resolution maps, foreground contamination, and an untrimmed cluster catalogue, will be required to provide a full and rigorous validation of the method; these are left for future work.

5.4 Generalization to other localized signals

The method presented above is quite general, and can be easily modified to extract a wide range of other types of information from sky maps besides the SZ effect. All that is required is a parametric spatial profile for the signal and (optionally) information on the positions, amplitudes, or other parameters of the profiles in the form of a catalogue.

Owing to a number of novel properties of the method (discussed above), it is ideally suited to situations where there is a strong sensitivity to the correct handling of uncertainties due to manipulations such as the subtraction of foregrounds and the primary CMB. In the following sections, I will briefly outline a number of situations in which the method can be usefully applied.

5.4.1 Integrated Sachs-Wolfe effect

The integrated Sachs-Wolfe (ISW) effect is a temperature change in the CMB along a line of sight, caused by the time-variation of the gravitational potential as photons pass through regions where structures are forming [Sachs & Wolfe, 1967; Rees & Sciama, 1968]. The expected amplitude of the ISW effect is predicted to be small compared with the primary anisotropies, and so it is generally necessary to cross-correlate CMB sky maps with tracers of large-scale structure in order to pick out the signal.

One such method uses a Voronoi tessellation technique to identify super-voids or clusters in galaxy redshift surveys [Granett *et al.*, 2008]. These are cross-correlated with CMB maps, assuming some profile for the ISW contribution from each void/cluster, and the results stacked in order to increase signal-to-noise. A number of claims have been made with respect to this method, including a significant detection of ISW which is inconsistent with ΛCDM predictions [Hunt & Sarkar, 2010; Papai *et al.*, 2011]. Nadathur *et al.* [2012] (also Flender *et al.* [2013]) argue that the result depends on a more sophisticated treatment of the predicted ISW temperature profile, derived from linear theory, but still conclude that the data are inconsistent with the standard model prediction.

5.4.2 Topological defects

Phase transitions associated with spontaneous symmetry breaking in the early universe should give rise to topological defects – the inhomogeneous boundaries between regions of different vacuum states [Durrer, 1999]. Defects leave discontinuities and other characteristic non-Gaussian patterns in the CMB, with shapes that depend on the type of underlying symmetry that was broken. Most theories predict that only of order a few defects can be expected to be visible in the CMB, and so they have been invoked as possible explanations of the handful of apparent CMB anomalies, such as the cold spot [Cruz *et al.*, 2005].

A number of authors have searched for evidence of various types of defect in the CMB, with varying degrees of apparent success (e.g. Jeong & Smoot [2005]; Cruz *et al.* [2008]; Feeney *et al.* [2012]). In order to claim that a detected anomaly is in fact the result of a topological defect, a number of other potential explanations must first be ruled out; for example, a claimed detection of a cosmic texture may also be plausibly explained by the existence of an intervening cluster or void. In order to distinguish between the different options, the measured temperature profile of the anomaly can be compared with various model profiles, and the significance of detection with each compared [Cruz *et al.*, 2008].

5.4.3 Signatures of pre-inflationary physics

A number of proposed models of pre-inflationary physics contain processes that imprint patterns into the CMB that are not expected in the standard (Gaussian and isotropic) picture. These patterns typically take the form of circles, concentric rings, or other simple geometric shapes in the CMB temperature field or its variance, superimposed on anisotropies that are otherwise well-described as a Gaussian random field. Examples of models which predict such effects include [Wehus & Eriksen, 2011]: bubble collisions in multiverse scenarios [Feeney *et al.*, 2011]; cyclic cosmologies where primordial black holes collide [Gurzadyan & Penrose, 2010]; and models in which massive particles exist before inflation [Fialkov *et al.*, 2010]. A closed spacetime topology would also give similar effects [Cornish *et al.*, 1998]. Such theories normally predict a characteristic shape for the patterns, and often impose other constraints such as pairing of the shapes, or fixed concentricities. This makes it possible to construct well-defined model profiles for the expected signal in the CMB, which can then be plugged into Commander.

Chapter 6

Conclusions

In this thesis, I have considered the relativistic effects of matter inhomogeneities on the accelerating expansion of the Universe, and used spectral distortions such as the kinematic Sunyaev-Zel'dovich (KSZ) effect to constrain deviations from homogeneity on large scales. I also demonstrated a method for extracting the thermal and kinematic SZ signals of galaxy clusters from CMB sky maps. In this chapter, I review my key findings and the conclusions that may be drawn from them, and suggest directions for future research.

6.1 Summary of key findings

In Chapter 2, I investigated the relationship between several different measures of cosmic acceleration, each of which corresponded to a theoretical or observational procedure that has previously been used in the literature. While the measures all converge to give the same result in a perfectly homogeneous and isotropic FLRW spacetime, I showed that they could behave very differently to one another in an inhomogeneous spacetime. In statistically homogeneous and isotropic spacetimes, I found that the acceleration inferred from observations of the distance-redshift relation is closely related to the acceleration of the spatially averaged universe, but does not necessarily bear any resemblance to the average of the local acceleration of spacetime itself. The local acceleration was closely related to the acceleration of local observables defined using the Kristian-Sachs formalism, however.

For inhomogeneous spacetimes that do not display statistical homogeneity and isotropy, I found little correlation between acceleration inferred from observations and the acceleration of the averaged spacetime. This throws into question the physical significance of attempts to show that LTB spacetimes can demonstrate average acceleration, since the LTB models that would appear to observers to be accelerating do not seem to be the same ones that have accelerating averages, and vice versa.

These results suggest that we should use non-local averages of the geometry to interpret observations made over large distances, and local geometry to interpret observations made locally. Interpreting observations within the wrong framework can lead to incorrect inferences about what is causing the acceleration – for statistically-homogeneous models at least, observations made in an inhomogeneous universe can, in principle, imply acceleration without the existence of dark energy. This constitutes a concrete demonstration of backreaction and its observable effects.

In Chapter 3, I considered whether the apparent acceleration of the Universe could instead be explained by relaxing the assumption of homogeneity and isotropy on large scales. I used the spherically-symmetric, radially-inhomogeneous Lemaître-Tolman-Bondi (LTB) models to derive strong constraints on the commonly-studied scenario of a giant underdense void. After discussing how observations of the KSZ effect are sensitive to large scale inhomogeneity, I reviewed previous studies that have used this effect, plus observations of Type Ia supernovae, the CMB power spectrum, and the local Hubble rate, to constrain void models.

Most of these studies set the LTB ‘bang time’ function to be constant, neglecting an important freedom of the general solutions. I examined dust-only LTB models in their full generality by relaxing this assumption, and found that although the extra freedom allowed by varying the bang time is sufficient to account for some observables individually, it is not enough to simultaneously explain the supernova observations, the small-angle CMB, the local Hubble rate, and the KSZ effect. I have therefore shown that existing cosmological datasets effectively rule out simple LTB models, which were hitherto the most successful conventional, relativistic attempt to explain the cosmic acceleration without recourse to new matter fields, a cosmological constant, or modifications to gravity.

In Chapter 4, I showed how the presence of a local inhomogeneity would bias the determination of cosmological parameters, and in particular the spatial curvature, Ω_K. Inflationary theory predicts that the observable Universe should be very close to being spatially flat, so if a forthcoming experiment detected curvature at a level of $|\Omega_K| \gtrsim 10^{-4}$, this would have serious ramifications for a range of inflationary models. I showed that certain secondary anisotropies that distort or shift the CMB frequency spectrum (such as the KSZ effect) provide an effective way of testing whether a detection of non-zero spatial curvature is due to a genuine superhorizon departure from the critical density, or parameter bias due to a local inhomogeneity. Current observations of the KSZ angular power at $\ell = 3000$ from ACT and SPT are sufficient to rule out the local inhomogeneity explanation for curvature greater than around $|10^{-3}|$, so a detection of Ω_K at this level in forthcoming Planck CMB data would put stringent constraints on a variety of inflationary scenarios.

I also discussed a method for using more general types of CMB blackbody distortion to test the Cosmological Principle. In a perfectly homogeneous and isotropic FLRW spacetime, CMB radiation that has been Compton scattered necessarily retains its blackbody form (except for a distortion due to the thermal SZ effect, which I assumed could be removed perfectly). In an inhomogeneous spacetime, however, anisotropies about scatterers result in additional blackbody distortions. If CMB radiation that has been scattered twice, or which has been observed over an extended period of time, could be measured to be pure blackbody, this would empirically prove the Cosmological Principle through an application of the Ehlers-Geren-Sachs theorem. While this is a highly idealised situation, it at least suggests that it might be possible to construct more practical tests of the Cosmological Principle.

In Chapter 5, I reviewed a number of methods for extracting the thermal and kinematic SZ signal from CMB sky maps, and discussed how TSZ and KSZ observations of galaxy clusters can be used to constrain cosmology. In the case of the KSZ effect, the signal is weak and has the same frequency spectrum as primary CMB anisotropies, making it particularly difficult to extract. I noted how detections of the effect could be made using peculiar velocity statistics calculated in linear theory, and listed some of the statistics that are known in the literature.

Following this, I outlined a fully Bayesian approach to the characterisation of the SZ signal from galaxy clusters. This method is a direct extension of a CMB component separation method based on Gibbs sampling, implemented in a code called ‘Commander’. This can be used to find the full joint posterior distribution of all components of the CMB sky, which can then be exactly marginalised over to produce accurate estimates of the SZ signal and its accompanying statistical uncertainty. The method relies on a parametrised model for the SZ signal from clusters, and allows for the inclusion of prior information on cluster positions and shapes from X-ray catalogues (and elsewhere) in a natural way. Peculiar velocity statistics can also be added into the analysis framework and estimated directly, greatly enhancing the prospects of successfully extracting the weak KSZ signal from forthcoming data.

In summary, I have shown how relativistic effects associated with matter inhomogeneities can be important in discovering the true nature of the apparent acceleration of the cosmos. Furthermore, I have shown that the KSZ effect is a stringent probe of inhomogeneity on large scales, and discussed how the SZ signal due to galaxy clusters can be reliably extracted from CMB data.

6.2 Future directions

The question of whether backreaction is important in our Universe remains unresolved, as evidenced by the variety of competing claims in the literature that were discussed in Section 1.2.4. In Chapter 2, I demonstrated a clear link between observables and the behaviour of an averaged model, showing that backreaction from spatial averaging is not simply a mathematical construct with no observational consequences, counter to claims made by Ishibashi & Wald [2006]. This was a necessary step in understanding backreaction in the real world, as it opens up the possibility of testing for these effects observationally (see e.g. Clarkson *et al.* [2012], or my suggestion to probe mismatches between quantities measured both locally and non-locally in Section 2.4). Nevertheless, a convincing theoretical demonstration of non-trivial backreaction in a realistic relativistic model is still required.

So far this has proved elusive, for the reasons discussed in the introduction to Section 1.2.1. To move forward will require more sophisticated calculations that may include: (a) more realistic exact solutions that have less symmetry, such as Szekeres solutions [Meures & Bruni, 2012]; (b) alternative or higher-order perturbative expansions, such as the 'gradient expansion' of Enqvist *et al.* [2012] that claims non-trivial backreaction effects; or (c) fully-relativistic numerical simulations[1] (see Bentivegna & Korzyński [2012] for an early application to the backreaction problem).

The status of large-scale inhomogeneities as explanations of the apparent acceleration is rather more certain. LTB void models are undoubtedly the most observationally successful inhomogeneous cosmological exact solutions that have been studied to date, but in Chapter 3 I showed that they are not supported by the available data even in their most general dust-only form. It is possible to

---

[1] Standard Newtonian N-body simulations cannot be used because backreaction necessarily vanishes in Newtonian gravity (for periodic boundary conditions) [Räsänen, 2010].

construct more sophisticated (and less symmetric) exact solutions that are inhomogeneous on large scales (e.g. quasi-spherical Szekeres solutions [Mishra *et al.*, 2013]), but I conjecture that they are also unlikely to be supported by observations. As I have discussed at length in Chapters 3 and 4, large inhomogeneous structures cause anisotropies in the CMB about distant galaxy clusters, which give rise to a detectable KSZ effect. My expectation is that for inhomogeneities large enough to mimic dark energy, the resulting KSZ signal will necessarily be large, as in Chapter 3. It could be the case that spherically-symmetric matter distributions (as considered in previous chapters) enhance the signal, and that less symmetric distributions might produce a smaller effect, but it would be difficult to get such anisotropic structures to match constraints on the isotropy of the CMB about us. Nevertheless, this is only conjecture, and would need to be confirmed before any firm conclusions can be drawn.

Alternatively, an observational test of the Cosmological Principle may be able to provide a definitive answer. The spectral distortion test outlined in Section 4.4, though promising, is currently impractical. An extension of the theorem to the 'almost'-EGS case, where small deviations from isotropy could be shown to imply only small deviations from homogeneity, would be required in order to sensibly apply it to the real universe. It would also have to be shown that spectral distortions due to anisotropy of the CMB could be distinguished from the TSZ effect, and that twice-scattered photons are observable (or alternatively, that it is practical to observe the CMB for a long enough time).

Investigations into the distribution of matter on extremely large scales would become more pressing if forthcoming Planck data showed a deviation from flatness at the levels considered in Chapter 4. While I showed that existing KSZ constraints from ACT and SPT are sufficient to rule out a simplified, spherically-symmetric local inhomogeneity that could cause an $\mathcal{O}(10^{-3})$ bias in the curvature parameter, an actual detection of curvature would required more careful modelling to be able to say anything concrete about the nature of the deviation. Inhomogeneities that are not exactly spherical symmetry about us would have to be considered, as would modelling uncertainties in the distribution of ionised gas out to high redshift, and the nonlinear matter power spectrum at low redshift.

Finally, the SZ extraction method described in Chapter 5, though promising, requires more extensive validation. The WMAP simulations in Section 5.3 were enough to show that the basic method works, but more realistic simulations with Planck instrumental specifications, galactic foregrounds, the KSZ effect, and higher-resolution maps also need to be performed. The method will ultimately be applied to the publicly-released Planck data, and the cosmological implications of the results will need to be analysed.

Beyond the SZ effect, one can also consider the extensions to Commander that were discussed in Section 5.4. Each extension differs in its details, and so further changes to the Commander code would be required to support, for example, spatial templates with a varying size (which are needed to search for concentric circles). More ambitious extensions of the framework to new applications such as HI intensity mapping [Peterson *et al.*, 2009] would also be an interesting prospect.

References

Abramo, L.R., Batista, R.C., Liberato, L. & Rosenfeld, R. (2009). Physical approximations for the nonlinear evolution of perturbations in inhomogeneous dark energy scenarios. *Phys. Rev. D*, **79**, 023516.

Addison, G.E., Dunkley, J. & Spergel, D.N. (2012). Modelling the correlation between the thermal Sunyaev Zel'dovich effect and the cosmic infrared background. *Mon. Not. Roy. Astron. Soc.*.

Afshordi, N., Slosar, A. & Wang, Y. (2011). A theory of a spot. *JCAP*, **01**, 019.

Aghanim, N., Gorski, K.M. & Puget, J.L. (2001). How accurately can the SZ effect measure peculiar cluster velocities and bulk flows? *A&A*.

Aghanim, N., Majumdar, S. & Silk, J. (2008). Secondary anisotropies of the CMB. *Rept. Prog. Phys.*, **71**, 066902.

Albrecht, A., Bernstein, G., Cahn, R. *et al.* (2006). Report of the dark energy task force. *ArXiv e-print*, **astro-ph/0609591**.

Alnes, H. & Amarzguioui, M. (2006). CMB anisotropies seen by an off-center observer in a spherically symmetric inhomogeneous universe. *Phys. Rev. D*, **74**, 103520.

Alonso, D., García-Bellido, J., Haugbølle, T. & Vicente, J. (2010). Large scale structure simulations of inhomogeneous Lemaître-Tolman-Bondi void models. *Phys. Rev. D*, **82**, 123530.

Amanullah, R., Lidman, C., Rubin, D. *et al.* (2010). Spectra and Hubble Space Telescope light curves of six Type Ia supernovae at $0.511 < z < 1.12$ and the UNION2 compilation. *ApJ*, **716**, 712.

Andersson, L. & Coley, A. (2011). Inhomogeneous cosmological models and averaging in cosmology: overview. *Class. Quant. Grav.*, **28**, 160301.

Arkani-Hamed, N., Hall, L.J., Kolda, C.F. & Murayama, H. (2000). A New perspective on cosmic coincidence problems. *Phys. Rev. Lett.*, **85**, 4434–4437.

Arnaud, M., Pratt, G.W., Piffaretti, R., Boehringer, H., Croston, J. *et al.* (2009). The universal galaxy cluster pressure profile from a representative sample of nearby systems (REXCESS) and the $Y_{SZ} - M_{500}$ relation. *A&A*.

Atrio-Barandela, F., Kashlinsky, A., Ebeling, H. & Kocevski, D. (2012). Cosmic Microwave Background filters and the Dark-Flow measurement. *ArXiv e-prints*, **1211.4345**.

Bardeen, J.M. (1980). Gauge Invariant Cosmological Perturbations. *Phys. Rev. D*, **D22**, 1882–1905.

Battye, R.A. & Weller, J. (2003). Constraining cosmological parameters using Sunyaev-Zel'dovich cluster surveys. *Phys. Rev. D D*, **68**, 083506.

Baumann, D., Nicolis, A., Senatore, L. & Zaldarriaga, M. (2012). Cosmological non-linearities as an effective fluid. *JCAP*, **1207**, 051.

Bennett, C.L., Larson, D., Weiland, J.L. *et al.* (2013). Nine-Year Wilkinson Microwave Anisotropy Probe (WMAP) Observations: Final Maps and Results. *ArXiv e-prints*, **1212.5225**.

Benson, B.A., de Haan, T., Dudley, J.P. *et al.* (2013). Cosmological Constraints from Sunyaev-Zel'dovich-Selected Clusters with X-ray Observations in the First 178 Square Degrees of the South Pole Telescope Survey. *ApJ*, **763**, 147.

Benson, B.A. *et al.* (2003). Peculiar velocity limits from measurements of the spectrum of the Sunyaev-Zel'dovich effect in six clusters of galaxies. *ApJ*, **592**, 674.

Bentivegna, E. & Korzyński, M. (2012). Evolution of a periodic eight-black-hole lattice in numerical relativity. *Class. Quant. Grav.*, **29**, 165007.

Bertone, G., Hooper, D. & Silk, J. (2005). Particle dark matter: evidence, candidates and constraints. *Phys. Rep.*, **405**, 279–390.

Bhattacharya, S. & Kosowsky, A. (2007). Cosmological Constraints from Galaxy Cluster Velocity Statistics. *ApJ*, **659**, L83–L86.

Bhattacharya, S. & Kosowsky, A. (2008). Dark Energy Constraints from Galaxy Cluster Peculiar Velocities. *Phys. Rev. D*, **77**, 083004.

Birkinshaw, M. (1999). The Sunyaev-Zel'dovich effect. *Phys. Rep.*, **310**, 97–195.

Biswas, T., Notari, A. & Valkenburg, W. (2010). Testing the Void against Cosmological data: fitting CMB, BAO, SN and H0. *JCAP*, **11**, 030.

Blas, D., Lesgourgues, J. & Tram, T. (2011). The Cosmic Linear Anisotropy Solving System (CLASS). Part II: Approximation schemes. *JCAP*, **07**, 034.

Böhringer, H., Schuecker, P., Pratt, G.W., Arnaud, M., Ponman, T.J. *et al.* (2007). The Representative XMM-Newton Cluster Structure Survey (REXCESS) of an X-ray Luminosity Selected Galaxy Cluster Sample. *A&A*, **469**, 363–377.

Bolejko, K. (2011). The effect of inhomogeneities on the distance to the last scattering surface and the accuracy of the CMB analysis. *JCAP*, **1102**, 025.

Bolejko, K. & Andersson, L. (2008). Apparent and average accelerations of the Universe. *JCAP*, **10**, 003.

Bolejko, K. & Célérier, M.N. (2010). Szekeres Swiss-cheese model and supernova observations. *Phys. Rev. D*, **82**, 103510.

Bolejko, K. & Ferreira, P.G. (2012). Ricci focusing, shearing, and the expansion rate in an almost homogeneous Universe. *JCAP*, **05**, 003.

Bolejko, K. & Lasky, P. (2008). Pressure gradients, shellcrossing singularities and acoustic oscillations – application to inhomogeneous cosmological models. *Mon. Not. Roy. Astron. Soc.*, **391**, L59.

Bolejko, K. & Wyithe, J. (2009). Testing the copernican principle via cosmological observations. *JCAP*, **02**, 020.

Bolejko, K., Krasiński, A., Hellaby, C. & Célérier, M.N. (2009). *Structures in the Universe by exact methods: formation, evolution, interactions*, vol. 1. Cambridge University Press.

Bolejko, K., Célérier, M.N. & Krasiński, A. (2011a). Inhomogeneous cosmological models: exact solutions and their applications. *Class. Quant. Grav.*, **28**, 164002.

Bolejko, K., Hellaby, C. & Alfedeel, A.H.A. (2011b). The metric of the cosmos from luminosity and age data. *JCAP*, **09**, 011.

Bondi, H. (1947). Spherically symmetrical models in general relativity. *Mon. Not. Roy. Astron. Soc.*, **107**, 410.

Bonvin, C., Durrer, R. & Gasparini, M.A. (2006). Fluctuations of the luminosity distance. *Phys. Rev. D*, **73**, 023523, erratum: *Phys. Rev. D* **85**, 029901 (2012).

Bousso, R. (2008). TASI Lectures on the Cosmological Constant. *Gen. Rel. Grav.*, **40**, 607–637.

Brouzakis, N., Tetradis, N. & Tzavara, E. (2007). The effect of large scale inhomogeneities on the luminosity distance. *JCAP*, **02**, 013.

Buchert, T. (2000). On average properties of inhomogeneous fluids in general relativity: dust cosmologies. *Gen. Rel. Grav.*, **32**, 105.

Buchert, T. & Räsänen, S. (2012). Backreaction in Late-Time Cosmology. *Annual Review of Nuclear and Particle Science*, **62**, 57–79.

Buchert, T., Kerscher, M. & Sicka, C. (2000). Back reaction of inhomogeneities on the expansion: The Evolution of cosmological parameters. *Phys. Rev. D*, **D62**, 043525.

Caldwell, R.R. & Stebbins, A. (2008). A test of the Copernican principle. *Phys. Rev. Lett.*, **100**, 191302.

Carlstrom, J.E., Holder, G.P. & Reese, E.D. (2002). Cosmology with the Sunyaev-Zel'dovich effect. *Ann. Rev. A&A*, **40**, 643–680.

Carroll, S.M. (2001). The Cosmological constant. *Living Rev. Rel.*, **4**, 1.

Célérier, M.N. (2000). Do we really see a cosmological constant in the supernovae data? *A&A*, **353**, 63.

Célérier, M.N. (2012). Some clarifications about Lemaître-Tolman models of the Universe used to deal with the dark energy problem. *A&A*, **543**, A71.

Célérier, M.N. & Schneider, J. (1998). A solution to the horizon problem: a delayed big bang singularity. *Phys. Lett.*, **A249**, 37.

Célérier, M.N., Bolejko, K. & Krasiński, A. (2010). A (giant) void is not mandatory to explain away dark energy with a Lemaître-Tolman model. *A&A*, **518**, A21.

Challinor, A. & Lasenby, A. (1999). Comptonization of an Isotropic Distribution in Moving Media: Higher Order Effects. *ApJ*, **510**, 930.

Chluba, J. & Sunyaev, R.A. (2004). Superposition of blackbodies and the dipole anisotropy: A possibility to calibrate CMB experiments. *A&A*, **424**, 389–408.

Chuang, C.H., Gu, J.A. & Hwang, W.Y.P. (2008). Inhomogeneity-induced cosmic acceleration in a dust universe. *Class. Quant. Grav.*, **25**, 175001.

Clarkson, C. & Maartens, R. (2010). Inhomogeneity and the foundations of concordance cosmology. *Class. Quant. Grav.*, **27**, 124008.

Clarkson, C. & Regis, M. (2011). The cosmic microwave background in an inhomogeneous universe. *JCAP*, **02**, 013.

Clarkson, C. & Umeh, O. (2011). Is backreaction really small within concordance cosmology? *Class. Quantum Grav.*, **28**, 164010.

Clarkson, C., Clifton, T. & February, S. (2009). Perturbation theory in Lemaître-Tolman-Bondi cosmology. *JCAP*, **06**, 025.

Clarkson, C., Ellis, G.F.R., Larena, J. & Umeh, O. (2011). Does the growth of structure affect our dynamical models of the universe? The averaging, backreaction and fitting problems in cosmology. *Rept. Prog. Phys.*, **74**, 112901.

Clarkson, C., Clifton, T., Coley, A. & Sung, R. (2012). Observational constraints on the averaged universe. *Phys. Rev. D*, **85**, 043506.

Clarkson, C.A. & Barrett, R.K. (1999). Does the isotropy of the CMB imply a homogeneous universe? Some generalized EGS theorems. *Class. Quant. Grav.*, **16**, 3781.

Clifton, T. (2011). Cosmology without averaging. *Class. Quant. Grav.*, **28**, 164011.

Clifton, T. & Ferreira, P.G. (2009). Archipelagian cosmology: Dynamics and observables in a universe with discretized matter content. *Phys. Rev. D*, **80**, 103503.

Clifton, T. & Zuntz, J. (2009). Hubble diagram dispersion from largescale structure. *Mon. Not. Roy. Astron. Soc.*, **400**, 2185.

Clifton, T., Ferreira, P.G. & Land, K. (2008). Living in a void: testing the Copernican principle with distant supernovae. *Phys. Rev. Lett.*, **101**, 131302.

Clifton, T., Ferreira, P.G. & Zuntz, J. (2009). What the small angle CMB really tells us about the curvature of the Universe. *JCAP*, **07**, 029.

Clifton, T., Clarkson, C. & Bull, P. (2012a). The isotropic blackbody CMB as evidence for a homogeneous universe. *Phys. Rev. Lett.*, **109**, 051303.

Clifton, T., Ferreira, P.G., Padilla, A. & Skordis, C. (2012b). Modified gravity and cosmology. *Phys. Rep.*.

COLGATE, S.A. (1979). Supernovae as a standard candle for cosmology. *ApJ*, **232**, 404–408.

COPERNICUS, N. (1543). *De revolutionibus orbium coelestium.* Johannes Petreius, Nuremburg.

CORNISH, N.J., SPERGEL, D.N. & STARKMAN, G.D. (1998). Circles in the sky: Finding topology with the microwave background radiation. *Class. Quant. Grav.*, **15**, 2657–2670.

COWLES, M.K. & CARLIN, B.P. (1996). Markov chain Monte Carlo convergence diagnostics: a comparative review. *J. Am. Stat. Assoc.*, **91**, 883–904.

CRUZ, M., MARTINEZ-GONZALEZ, E., VIELVA, P. & CAYON, L. (2005). Detection of a non-gaussian spot in wmap. *Mon. Not. Roy. Astron. Soc.*, **356**, 29–40.

CRUZ, M., MARTINEZ-GONZALEZ, E., VIELVA, P. *et al.* (2008). The CMB cold spot: texture, cluster or void? *Mon. Not. Roy. Astron. Soc.*.

DAWSON, K.S., SCHLEGEL, D.J., AHN, C.P. *et al.* (2013). The Baryon Oscillation Spectroscopic Survey of SDSS-III. *ApJ*, **145**, 10.

DE SITTER, W. (1917). Einstein's theory of gravitation and its astronomical consequences, Third Paper. *Mon. Not. Roy. Astron. Soc.*, **78**, 3–28.

D'EATH, P.D. (1976). On the existence of perturbed robertson-walker universes. *Annals of Physics*, **98**, 237 – 263.

DI DIO, E., VONLANTHEN, M. & DURRER, R. (2012). Back reaction from walls. *JCAP*, **1202**, 036.

DICKE, R.H. & PEEBLES, P.J.E. (1979). The big bang cosmology - enigmas and nostrums. In *General relativity: an Einstein centenary survey*, vol. 1, 504–517.

DICKINSON, C., ERIKSEN, H.K., BANDAY, A.J. *et al.* (2009). Bayesian component separation and CMB estimation for the 5-year WMAP temperature data. *ApJ*, **705**, 1607–1623.

DODELSON, S. (2003). *Modern Cosmology*. Academic Press.

DOLGOV, A.D., HANSEN, S.H., PASTOR, S. & SEMIKOZ, D.V. (2001). Spectral Distortion of Cosmic Microwave Background Radiation by Scattering on Hot Electrons: Exact Calculations. *Ap.J*, **554**, 74–84.

DRAPER, P., DODELSON, S., HAO, J. & ROZO, E. (2012). Sunyaev-Zel'dovich signal of the maxBCG SDSS galaxy clusters in WMAP. *Phys. Rev. D*, **85**, 023005.

DUNKLEY, J., CALABRESE, E., SIEVERS, J., ADDISON, G.E., BATTAGLIA, N. *et al.* (2013). The Atacama Cosmology Telescope: likelihood for small-scale CMB data. *ArXiv e-prints*, **1301.0776**.

DURRER, R. (1994). Gauge Invariant Cosmological Perturbation Theory. *Fund. Cosmic Phys.*, **15**, 209–339.

DURRER, R. (1999). Topological defects in cosmology. *New Astron. Rev.*, **43**, 111–156.

Durrer, R. (2011). What do we really know about Dark Energy? *Phil. Trans. Roy. Soc. Lond.*, **A369**, 5102–5114.

Durrer, R. & Maartens, R. (2008). Dark Energy and Dark Gravity. *Gen. Rel. Grav.*, **40**, 301–328.

Dyer, C.C. & Oliwa, C. (2001). Matching of Friedmann-Lemaître-Robertson-Walker and Kasner cosmologies. *Class. Quant. Grav.*, **18**, 2719.

Ehlers, J., Geren, P. & Sachs, R.K. (1968). Isotropic Solutions of the Einstein-Liouville Equations. *J. Math. Phys.*, **9**, 344.

Einstein, A. (1917). Cosmological Considerations in the General Theory of Relativity. *Sitzungsber. Preuss. Akad. Wiss. Berlin (Math. Phys.)*, **1917**, 142–152.

Eisenstein, D.J. *et al.* (2001). Spectroscopic target selection for the Sloan Digital Sky Survey: The Luminous red galaxy sample. *Astron. J.*, **122**, 2267.

Ellis, G.F.R. (1971). Relativistic Cosmology. In R.K. Sachs, ed., *General Relativity and Cosmology, Proc. Int. School of Physics "Enrico Fermi" (Varenna), Course XLVII*, Academic Press, New York, reprinted in *Gen. Rel. Grav.* **41**, 581 (2009).

Ellis, G.F.R. (1984). Relativistic Cosmology: Its Nature, Aims and Problems. In B. Bertotti, F. de Felice & A. A. Pascolini, eds., *General Relativity and Gravitation*, Dordrecht: Reidel.

Ellis, G.F.R. (2006). The Bianchi models: Then and now. *Gen. Rel. Grav.*, **38**, 1003–1015.

Ellis, G.F.R. (2009). Dark energy and inhomogeneity. In *Journal of Physics: Conference Series*, vol. 189, 012011, IOP Publishing.

Ellis, G.F.R. (2011). Inhomogeneity effects in cosmology. *Class. Quant. Grav.*, **28**, 164001.

Ellis, G.F.R. & Buchert, T. (2005). The Universe seen at different scales. *Phys. Lett. A*, **347**, 38–46.

Ellis, G.F.R. & Jaklitsch, M.J. (1989). Integral constraints on perturbations of Robertson-Walker cosmologies. *ApJ*, **346**, 601.

Ellis, G.F.R. & Stoeger, W. (1987). The 'fitting problem' in cosmology. *Class. Quant. Grav.*, **4**, 1697–1729.

Ellis, G.F.R. & van Elst, H. (1998). Cosmological Models (Cargèse Lectures 1998) Preprint. *arXiv e-print*, **gr-qc/9812046**.

Ellis, G.F.R., Maartens, R. & MacCallum, M.A.H. (2012). *Relativistic cosmology*. Cambridge University Press.

Enqvist, K., Hotchkiss, S. & Rigopoulos, G. (2012). A Gradient expansion for cosmological backreaction. *JCAP*, **1203**, 026.

Erickcek, A.L., Carroll, S.M. & Kamionkowski, M. (2008). Superhorizon perturbations and the cosmic microwave background. *Phys. Rev. D*, **78**, 083012.

Eriksen, H.K., O'Dwyer, I.J., Jewell, J.B. *et al.* (2004). Power spectrum estimation from high-resolution maps by Gibbs sampling. *ApJS*, **155**, 227–241.

Eriksen, H.K., Jewell, J.B., Dickinson, C. *et al.* (2008). Joint Bayesian component separation and CMB power spectrum estimation. *ApJ*, **676**, 10–32.

Etherington, I.M.H. (1933). On the definition of distance in general relativity. *Phil. Mag.*, **15**, 761, reprinted in *Gen. Rel. Grav.* **39**, 1047 (2007).

February, S., Larena, J., Smith, M. & Clarkson, C. (2010). Rendering dark energy void. *Mon. Not. Roy. Astron. Soc.*, **405**, 2231.

February, S., Clarkson, C. & Maartens, R. (2012). Galaxy correlations and the BAO in a void universe: structure formation as a test of the Copernican Principle. *ArXiv e-prints*, **1206.1602**.

Feeney, S.M., Johnson, M.C., Mortlock, D.J. & Peiris, H.V. (2011). First Observational Tests of Eternal Inflation: Analysis Methods and WMAP 7-Year Results. *Phys. Rev. D*, **84**, 043507.

Feeney, S.M., Johnson, M.C., Mortlock, D.J. & Peiris, H.V. (2012). A robust constraint on cosmic textures from the cosmic microwave background. *Phys. Rev. Lett.*, **108**, 241301.

Ferrando, J.J., Morales, J.A. & Portilla, M. (1992). Inhomogeneous spacetimes admitting isotropic radiation: Vorticity-free case. *Phys. Rev. D*, **46**, 578–584.

Ferreira, P.G., Juszkiewicz, R., Feldman, H.A., Davis, M. & Jaffe, A.H. (1999). Streaming velocities as a dynamical estimator of omega. *ApJ*, **515**, L1–L4.

Fialkov, A., Itzhaki, N. & Kovetz, E.D. (2010). Cosmological Imprints of Pre-Inflationary Particles. *JCAP*, **1002**, 004.

Fixsen, D.J. (2009). The Temperature of the Cosmic Microwave Background. *ApJ*, **707**, 916–920.

Fixsen, D.J., Cheng, E.S., Gales, J.M. *et al.* (1996). The Cosmic Microwave Background spectrum from the full COBE FIRAS data set. *ApJ*, **473**, 576.

Flanagan, E.E. (2005). Can superhorizon perturbations drive the acceleration of the Universe? *Phys. Rev. D*, **71**, 103521.

Flender, S., Hotchkiss, S. & Nadathur, S. (2013). The stacked ISW signal of rare superstructures in Lambda CDM. *JCAP*, **1302**, 013.

Foreman, S., Moss, A., Zibin, J.P. & Scott, D. (2010). Spatial and temporal tuning in void models for acceleration. *Phys. Rev. D*, **82**, 103532.

Fornengo, N. (2008). Status and perspectives of indirect and direct dark matter searches. *Adv. Space Res.*, **41**, 2010–2018.

Fosalba, P. & Gaztañaga, E. (1998). Cosmological perturbation theory and the spherical collapse model – I. Gaussian initial conditions. *Mon. Not. Roy. Astron. Soc.*, **301**, 503.

FRIEDMANN, A. (1922). Über die Krümmung des Raumes. *Zeitschrift fur Physik*, **10**, 377–386, reprinted in *General Relativity and Gravitation* **31**, 1991 (1999).

FUTAMASE, T. (1988). Approximation scheme for constructing a clumpy universe in general relativity. *Physical Review Letters*, **61**, 2175–2178.

GARCÍA-BELLIDO, J. & HAUGBØLLE, T. (2008a). Confronting Lemaître-Tolman-Bondi models with Observational Cosmology. *JCAP*, **04**, 003.

GARCÍA-BELLIDO, J. & HAUGBØLLE, T. (2008b). Looking the void in the eyes - the kSZ effect in LTB models. *JCAP*, **09**, 016.

GESHNIZJANI, G., CHUNG, D.J.H. & AFSHORDI, N. (2005). Do large-scale inhomogeneities explain away dark energy? *Phys. Rev. D*, **72**, 023517.

GOODMAN, J. (1995). Geocentrism reexamined. *Phys. Rev. D*, **52**, 1821.

GÓRSKI, K.M., HIVON, E., BANDAY, A.J. *et al.* (2005). HEALPix – A Framework for high resolution discretization, and fast analysis of data distributed on the sphere. *ApJ*, **622**, 759–771.

GRANETT, B.R., NEYRINCK, M.C. & SZAPUDI, I. (2008). An Imprint of Super-Structures on the Microwave Background due to the Integrated Sachs-Wolfe Effect. *ApJ*, **683**, L99–L102.

GREEN, S.R. & WALD, R.M. (2011). New framework for analyzing the effects of small scale inhomogeneities in cosmology. *Phys. Rev. D*, **83**, 084020.

GRISHCHUK, L.P. & ZEL'DOVICH, Y.B. (1978). Long-wavelength perturbations of a Friedmann universe, and anisotropy of the microwave background radiation. *Soviet Astronomy*, **22**, 125–129.

GUNN, J.E. & GOTT, I., J. R. (1972). On the infall of matter into clusters of galaxies and some effects on their evolution. *ApJ*, **176**, 1.

GURZADYAN, V.G. & PENROSE, R. (2010). Concentric circles in WMAP data may provide evidence of violent pre-Big-Bang activity. *ArXiv e-prints*, **1011.3706**.

GUTH, A.H. & NOMURA, Y. (2012). What can the observation of nonzero curvature tell us? *Phys. Rev. D*, **86**, 023534.

HAND, N., ADDISON, G.E., AUBOURG, E. *et al.* (2012). Evidence of Galaxy Cluster Motions with the Kinematic SZ Effect. *Phys. Rev. Lett.*, **109**, 041101.

HARRISON, E. (2000). Cosmology after Newton and before Einstein. In *Cosmology: the science of the universe*, Cambridge University Press.

HASSE, W. & PERLICK, V. (1999). On spacetime models with an isotropic Hubble law. *Class. Quant. Grav.*, **16**, 2559.

HASSELFIELD, M. *et al.* (2013). The Atacama Cosmology Telescope: Sunyaev-Zel'dovich Selected Galaxy Clusters at 148 GHz from Three Seasons of Data. *ArXiv e-prints*, **1301.0816**.

HELLABY, C. & LAKE, K. (1984). The redshift structure of the big bang in inhomogeneous cosmological models. I-Spherical dust solutions. *ApJ*, **282**, 1.

HELLABY, C. & LAKE, K. (1985). Shell crossings and the Tolman model. *ApJ*, **290**, 381.

HERRANZ, D., ARGUESO, F. & CARVALHO, P. (2012). Compact source detection in multi-channel microwave surveys: from SZ clusters to polarized sources. *Adv.Astron.*, **2012**, 410965.

HETHERINGTON, N.S. & MCCRAY, W.P. (2013). Cosmic Journey: A History of Scientific Cosmology. `http://www.aip.org/history/cosmology/index.htm`.

HINSHAW, G., LARSON, D., KOMATSU, E. *et al.* (2012). Nine-Year Wilkinson Microwave Anisotropy Probe (WMAP) Observations: Cosmological Parameter Results. *ArXiv e-prints*, **1212.5226**.

HIRATA, C.M. & SELJAK, U. (2005). Can superhorizon cosmological perturbations explain the acceleration of the universe? *Phys. Rev. D*, **72**, 083501.

HOLZAPFEL, W.L., ADE, P.A.R., CHURCH, S.E. *et al.* (1997). Limits on the Peculiar Velocities of Two Distant Clusters Using the Kinematic Sunyaev-Zeldovich Effect. *ApJ*, **481**, 35.

HU, W., FUKUGITA, M., ZALDARRIAGA, M. & TEGMARK, M. (2001). CMB Observables and Their Cosmological Implications. *ApJ*, **549**, 669.

HUBBLE, E. (1929). A relation between distance and radial velocity among extra-galactic nebulae. *Proc. Nat. Acad. Sci.*, **15**, 168–173.

HUNT, P. & SARKAR, S. (2010). Constraints on large scale inhomogeneities from WMAP-5 and SDSS: confrontation with recent observations. *Mon. Not. Roy. Astron. Soc.*, **401**, 547.

ISAACSON, R.A. (1968). Gravitational Radiation in the Limit of High Frequency. II. Nonlinear Terms and the Effective Stress Tensor. *Phys. Rev. D*, **166**, 1272–1279.

ISHIBASHI, A. & WALD, R.M. (2006). Can the acceleration of our universe be explained by the effects of inhomogeneities? *Class. Quant. Grav.*, **23**, 235.

ITOH, N., KOHYAMA, Y. & NOZAWA, S. (1998). Relativistic Corrections to the Sunyaev-Zel'dovich Effect for Clusters of Galaxies. *ApJ*, **502**, 7–15.

ITOH, N., KAWANA, Y., NOZAWA, S. & KOHYAMA, Y. (2001). Relativistic corrections to the multiple scattering effect on the Sunyaev-Zel'dovich effect in the isotropic approximation. *Mon. Not. Roy. Astron. Soc.*, **327**, 567–576.

JAFFE, A.H. & KAMIONKOWSKI, M. (1998). Calculation of the Ostriker-Vishniac effect in cold dark matter models. *Phys. Rev. D*, **58**, 043001.

JAIN, B. & ZHANG, P. (2008). Observational Tests of Modified Gravity. *Phys. Rev. D*, **78**, 063503.

JAROSIK, N., BENNETT, C.L., DUNKLEY, J. *et al.* (2011). Seven-year Wilkinson Microwave Anisotropy Probe (WMAP) observations: sky maps, systematic errors, and basic results. *ApJS*, **192**, 14.

JEONG, E. & SMOOT, G.F. (2005). Search for cosmic strings in CMB anisotropies. *ApJ*, **624**, 21–27.

JEWELL, J., LEVIN, S. & ANDERSON, C.H. (2004). Application of Monte Carlo algorithms to the Bayesian analysis of the cosmic microwave background. *ApJ*, **609**, 1–14.

KAI, T. *et al.* (2007). Can inhomogeneties accelerate the cosmic volume expansion? *Prog. Theor. Phys.*, **117**, 229.

KANTOWSKI, R., VAUGHAN, T. & BRANCH, D. (1995). The Effects of Inhomogeneities on Evaluating the Deceleration Parameter q_0. *ApJ*, **447**, 5.

KASAI, M., ASADA, H. & FUTAMASE, T. (2006). Toward a no-go theorem for an accelerating universe through a nonlinear backreaction. *Prog. Theor. Phys.*, **115**, 827.

KASHLINSKY, A., ATRIO-BARANDELA, F., KOCEVSKI, D. & EBELING, H. (2009). A measurement of large-scale peculiar velocities of clusters of galaxies: results and cosmological implications. *ApJ*, **686**, L49–L52.

KASHLINSKY, A., ATRIO-BARANDELA, F. & EBELING, H. (2012). Measuring bulk motion of X-ray clusters via the kinematic Sunyaev-Zeldovich effect: summarizing the 'dark flow' evidence and its implications. *ArXiv e-prints*, **1202.0717**.

KEISLER, R. (2009). The statistical significance of the "dark flow". *ApJL*, **707**, L42.

KITAYAMA, T., KOMATSU, E., OTA, N. *et al.* (2004). Exploring Cluster Physics with High-Resolution Sunyaev-Zel'dovich Effect Images and X-Ray Data: The Case of the Most X-Ray-Luminous Galaxy Cluster RX J1347-1145. *Publ. Astron. Soc. Jap.*, **56**, 17.

KLEBAN, M. & SCHILLO, M. (2012). Spatial curvature falsifies eternal inflation. *JCAP*, **1206**, 029.

KNOX, L. (2006). Precision measurement of the mean curvature. *Phys. Rev. D*, **73**, 023503.

KODAMA, H. & SASAKI, M. (1984). Cosmological Perturbation Theory. *Prog. Theor. Phys. Supp.*, **78**, 1.

KOESTER, B.P. *et al.* (2007). A MaxBCG Catalog of 13,823 Galaxy Clusters from the Sloan Digital Sky Survey. *ApJ*, **660**, 239–255.

KOGUT, A., FIXSEN, D.J. *et al.* (2011). The Primordial Inflation Explorer (PIXIE): a nulling polarimeter for cosmic microwave background observations. *JCAP*, **7**, 25.

KOLB, E.W. (2011). Backreaction of inhomogeneities can mimic dark energy. *Class. Quant. Grav.*, **28**, 164009.

KOLB, E.W., MATARRESE, S., NOTARI, A. & RIOTTO, A. (2005). The Effect of inhomogeneities on the expansion rate of the universe. *Phys. Rev. D*, **D71**, 023524.

KOLB, E.W., MARRA, V. & MATARRESE, S. (2008). On the description of our cosmological spacetime as a perturbed conformal Newtonian metric and implications for the backreaction proposal for the accelerating universe. *Phys. Rev. D*, **78**, 103002.

KOMATSU, E. & SELJAK, U. (2001). Universal gas density and temperature profile. *Mon. Not. Roy. Astron. Soc.*, **327**, 1353–1366.

KOMATSU, E., SMITH, K.M., DUNKLEY, J. *et al.* (2011). Seven-year Wilkinson microwave anisotropy probe (WMAP) observations: cosmological interpretation. *ApJS*, **192**, 92.

KRISTIAN, J. & SACHS, R.K. (1966). Observations in cosmology. *ApJ*, **143**, 379.

KRYMSKY, A.M., MAROCHNIK, L.S., NASELSKY, P.D. & PELIKHOV, N.V. (1978). Turbulence in cosmology. *Astrophysics and Space Science*, **55**, 325–350.

LAKE, K. (1992). An inhomogeneous slab cosmology. *ApJ*, **401**, L1.

LAMARRE, J.M., PUGET, J.L., ADE, P.A.R. *et al.* (2010). Planck pre-launch status: The hfi instrument, from specification to actual performance. *A&A*, **520**.

LANDRY, S. & DYER, C.C. (1997). Optical properties of the Einstein-de Sitter-Kasner universe. *Phys. Rev. D*, **56**, 3307.

LARSON, D., DUNKLEY, J., HINSHAW, G. *et al.* (2011). Seven-Year Wilkinson Microwave Anisotropy Probe (WMAP) Observations: Power Spectra and WMAP-Derived Parameters. *ApJS*, **192**, 16.

LAVAUX, G., AFSHORDI, N. & HUDSON, M.J. (2012). First measurement of the bulk flow of nearby galaxies using the cosmic microwave background. *ArXiv e-prints*, **1207.1721**.

LEACH, S.M., CARDOSO, J.F., BACCIGALUPI, C. *et al.* (2008). Component separation methods for the Planck mission. *A&A*, **491**, 597–615.

LEMAÎTRE, G. (1931). Expansion of the universe, A homogeneous universe of constant mass and increasing radius accounting for the radial velocity of extra-galactic nebulae. *Mon. Not. Roy. Astron. Soc.*, **91**, 483–490.

LEMAÎTRE, G. (1933). L'univers en expansion. *Ann. Soc. Sci. Brussels*, **A53**, 51.

LEWIS, A. & BRIDLE, S. (2002). Cosmological parameters from CMB and other data: A Monte Carlo approach. *Phys. Rev. D*, **66**, 103511.

LI, N. & SCHWARZ, D.J. (2008). Scale dependence of cosmological backreaction. *Phys. Rev. D*, **78**, 083531.

LIFSHITZ, E.M. (1946). Perturbation Theory. *J. Phys. USSR*, **10**, 116.

LINDE, A., LINDE, D. & MEZHLUMIAN, A. (1995). Do we live in the center of the world? *Phys. Lett. B*, **345**, 203.

Lindquist, R.W. & Wheeler, J.A. (1957). Dynamics of a lattice universe by the Schwarzschild-cell method. *Rev. Mod. Phys.*, **29**, 432, (Erratum: *Rev. Mod. Phys.* **31**, 839 (1959)).

Loken, C., Norman, M.L., Nelson, E., Burns, J., Bryan, G.L. *et al.* (2002). A Universal temperature profile for galaxy clusters. *ApJ*, **579**, 571–576.

Ma, C.P. & Bertschinger, E. (1995). Cosmological perturbation theory in the synchronous and conformal Newtonian gauges. *ApJ*, **455**, 7–25.

Ma, Y.Z., Gordon, C. & Feldman, H.A. (2011). The peculiar velocity field: constraining the tilt of the Universe. *Phys. Rev. D*, **83**, 103002.

Maartens, R. (2011). Is the Universe homogeneous? *Phil. Trans. Roy. Soc. Lond.*, **A369**, 5115–5137.

Maartens, R. & Matravers, D.R. (1999). Isotropic and semi-isotropic observations in cosmology. *Class. Quant. Grav.*, **11**, 2693.

Maartens, R., Ellis, G.F.R. & Stoeger, W.R. (1995a). Improved limits on anisotropy and inhomogeneity from the cosmic background radiation. *Phys. Rev. D*, **51**, 5942–5945.

Maartens, R., Ellis, G.F.R. & Stoeger, W.R. (1995b). Limits on anisotropy and inhomogeneity from the cosmic background radiation. *Phys. Rev. D*, **51**, 1525.

Macaulay, E., Feldman, H.A., Ferreira, P.G., Jaffe, A.H., Agarwal, S. *et al.* (2012). Power Spectrum Estimation from Peculiar Velocity Catalogues. *Mon. Not. Roy. Astron. Soc.*, **425**, 1709–1717.

MacKay, D.J.C. (2003). *Information theory, inference and learning algorithms*. Cambridge University Press.

Mao, Y., Tegmark, M., McQuinn, M., Zaldarriaga, M. & Zahn, O. (2008). How accurately can 21 cm tomography constrain cosmology? *Phys. Rev. D*, **78**, 023529.

Marion, J.B. (1965). *Classical Electromagnetic Radiation*. Academic Press, New York.

Marochnik, L.S., Pelikhov, N.V. & Vereshkov, G.M. (1975). Turbulence in cosmology. *Astrophys. Sp. Sci.*, **34**, 249–263.

Marra, V. & Pääkkönen, M. (2012). Exact spherically-symmetric inhomogeneous model with *n* perfect fluids. *JCAP*, **01**, 025.

Marriage, T.A., Acquaviva, V., Ade, P.A.R. *et al.* (2011). The Atacama Cosmology Telescope: Sunyaev Zel'dovich Selected Galaxy Clusters at 148 GHz in the 2008 Survey. *ApJ*, **737**, 61.

Matarrese, S., Verde, L. & Jimenez, R. (2000). The Abundance of high-redshift objects as a probe of non-Gaussian initial conditions. *ApJ*, **541**, 10.

Mattsson, M. & Mattsson, T. (2010). On the role of shear in cosmological averaging. *JCAP*, **10**, 021.

Mattsson, M. & Mattsson, T. (2011). On the role of shear in cosmological averaging II: large voids, non-empty voids and a network of different voids. *JCAP*, **1105**, 003.

Meures, N. & Bruni, M. (2012). Redshift and distances in a ΛCDM cosmology with nonlinear inhomogeneities. *Mon. Not. Roy. Astron. Soc.*, **419**, 1937.

Milne, E.A. (1935). *Relativity, gravitation and world-structure*. International series of monographs on physics, The Clarendon Press.

Mishra, P., Célérier, M.N. & Singh, T.P. (2013). Redshift-drift as a test for discriminating between decelerating inhomogeneous and accelerating universe models. *ArXiv e-prints*, **1301.4358**.

Moss, A., Zibin, J.P. & Scott, D. (2011). Precision cosmology defeats void models for acceleration. *Phys. Rev. D*, **83**, 103515.

Motl, P.M., Hallman, E.J., Burns, J.O. & Norman, M.L. (2005). The Integrated Sunyaev-Zeldovich effect as the superior method for measuring the mass of clusters of galaxies. *ApJ*, **623**, L63–L66.

Mukhanov, V.F., Feldman, H.A. & Brandenberger, R.H. (1992). Theory of cosmological perturbations. Part 1. Classical perturbations. Part 2. Quantum theory of perturbations. Part 3. Extensions. *Phys. Rep.*, **215**, 203–333.

Mustapha, N., Hellaby, C. & Ellis, G.F.R. (1997). Large Scale Inhomogeneity Versus Source Evolution – Can We Distinguish Them Observationally? *Mon. Not. Roy. Astron. Soc.*, **292**, 817.

Nadathur, S. & Sarkar, S. (2011). Reconciling the local void with the CMB. *Phys. Rev. D*, **83**, 063506.

Nadathur, S., Hotchkiss, S. & Sarkar, S. (2012). The integrated Sachs-Wolfe imprints of cosmic superstructures: a problem for ΛCDM. *JCAP*, **1206**, 042.

Nagai, D. (2006). The impact of galaxy formation on the Sunyaev-Zeldovich effect of galaxy clusters. *ApJ*, **650**, 538–549.

Nagai, D., Kravtsov, A.V. & Vikhlinin, A. (2007). Effects of Galaxy Formation on Thermodynamics of the Intracluster Medium. *ApJ*, **668**, 1–14.

Navarro, J.F., Frenk, C.S. & White, S.D.M. (1997). A universal density profile from hierarchical clustering. *ApJ*, **490**, 493–508.

Nikulin, M.S. (2001). Kolmogorov-Smirnov test. In M. Hazewinkel, ed., *Encyclopedia of Mathematics*, Springer.

Nishikawa, R., Yoo, C.M. & Nakao, K. (2012). Evolution of density perturbations in large void universe. *Phys. Rev. D*, **85**, 103511.

Osborne, S.J., Mak, D.S.Y., Church, S.E. & Pierpaoli, E. (2011). Measuring the Galaxy Cluster Bulk Flow from WMAP data. *ApJ*, **737**, 98.

Ostriker, J.P. & Steinhardt, P.J. (1995). Cosmic concordance. *ArXiv e-prints*, **astro-ph/9505066**.

OSTRIKER, J.P. & VISHNIAC, E.T. (1986). Generation of microwave background fluctuations from nonlinear perturbations at the ERA of galaxy formation. *ApJL*, **306**, L51–L54.

PADMANABHAN, T. (1993). *Structure Formation in the Universe*. Cambridge.

PAPAI, P., SZAPUDI, I. & GRANETT, B.R. (2011). Integrated Sachs-Wolf imprint of superstructures on linear scales. *ApJ*, **732**, 27.

PARANJAPE, A. (2009). *The Averaging Problem in Cosmology*. Ph.D. thesis, TIFR, Mumbai, Dept. Theor. Phys.

PARANJAPE, A. & SINGH, T.P. (2006). The possibility of cosmic acceleration via spatial averaging in Lemaître-Tolman-Bondi models. *Class. Quant. Grav.*, **23**, 6955.

PARKINSON, D. *et al.* (2012). The WiggleZ Dark Energy Survey: Final data release and cosmological results. *Phys. Rev. D*, **86**, 103518.

PEACOCK, J.A., COLE, S., NORBERG, P. *et al.* (2001). A measurement of the cosmological mass density from clustering in the 2dF Galaxy Redshift Survey. *Nature*, **410**, 169–173.

PEEBLES, P.J.E. (1980). *Large-scale structure of the Universe*. Princeton University Press.

PEEBLES, P.J.E. (2002). From precision cosmology to accurate cosmology. *ArXiv e-prints*, **astro-ph/0208037**.

PEEBLES, P.J.E. & NUSSER, A. (2010). Clues from nearby galaxies to a better theory of cosmic evolution. *Nature*, **465**, 565–569.

PEEBLES, P.J.E. & RATRA, B. (2003). The Cosmological constant and dark energy. *Rev. Mod. Phys.*, **75**, 559–606.

PERIVOLAROPOULOS, L. (2011). LCDM: Triumphs, Puzzles and Remedies. *ArXiv e-prints*, **1104.0539**.

PERLICK, V. (2004). Gravitational lensing from a spacetime perspective. *Living Rev. Rel.*, **7**, 9.

PERLMUTTER, S. *et al.* (1999). Measurements of Omega and Lambda from 42 high redshift supernovae. *ApJ*, **517**, 565–586.

PETERSON, J.B., ALEKSAN, R., ANSARI, R. *et al.* (2009). 21-cm Intensity Mapping. In *astro2010: The Astronomy and Astrophysics Decadal Survey*, vol. 2010 of *ArXiv e-prints*, 234.

PIFFARETTI, R., ARNAUD, M., PRATT, G.W., POINTECOUTEAU, E. & MELIN, J.B. (2010). The MCXC: a Meta-Catalogue of X-ray detected Clusters of galaxies. *A&A*, **534**, A109.

PLANCK COLLABORATION (2011a). Planck early results VIII: The all-sky early Sunyaev-Zeldovich cluster sample. *ArXiv e-print*, **1101.2024**.

PLANCK COLLABORATION (2011b). Planck early results. X. Statistical analysis of Sunyaev-Zeldovich scaling relations for X-ray galaxy clusters. *A&A*, **536**, A10.

PLANCK COLLABORATION (2011c). Planck early results. XIII. Statistical properties of extragalactic radio sources in the Planck Early Release Compact Source Catalogue. *A&A*, **536**.

PLANCK COLLABORATION (2012a). Planck Intermediate Results II: Comparison of Sunyaev-Zeldovich measurements from Planck and from the Arcminute Microkelvin Imager for 11 galaxy clusters. *ArXiv e-prints*, **1204.1318**.

PLANCK COLLABORATION (2012b). Planck Intermediate Results. III. The relation between galaxy cluster mass and Sunyaev-Zel'dovich signal. *ArXiv e-prints*, **1204.2743**.

PLANCK COLLABORATION (2013). Planck 2013 results. XVI. Cosmological parameters. *ArXiv e-prints*, **1303.5076**.

PLEBAŃSKI, J. & KRASIŃSKI, A. (2006). *An Introduction to General Relativity and Cosmology*. Cambridge University Press.

PONTZEN, A. & CHALLINOR, A. (2007). Bianchi Model CMB Polarization and its Implications for CMB Anomalies. *Mon. Not. Roy. Astron. Soc.*.

QUERCELLINI, C., AMENDOLA, L., BALBI, A., CABELLA, P. & QUARTIN, M. (2012). Real-time cosmology. *Phys. Rep.*, **521**, 95–134.

RAIFEARTAIGH, C.O. (2012). The contribution of VM Slipher to the discovery of the expanding universe. *ArXiv e-prints*, **1212.5499**.

RÄSÄNEN, S. (2004a). Backreaction in the LTB model. *JCAP*, **11**, 010.

RÄSÄNEN, S. (2004b). Dark energy from backreaction. *JCAP*, **0402**, 003.

RÄSÄNEN, S. (2006a). Accelerated expansion from structure formation. *JCAP*, **11**, 003.

RÄSÄNEN, S. (2006b). Cosmological acceleration from structure formation. *Int. J. Mod. Phys. D*, **15**, 2141.

RÄSÄNEN, S. (2009a). Light propagation in statistically homogeneous and isotropic dust universes. *JCAP*, **02**, 011.

RÄSÄNEN, S. (2009b). Relation between the isotropy of the CMB and the geometry of the universe. *Phys. Rev. D*, **79**, 123522.

RÄSÄNEN, S. (2009c). Structure formation as an alternative to dark energy and modified gravity. *EAS Publications Series*, **36**, 63–74.

RÄSÄNEN, S. (2010). Applicability of the linearly perturbed FRW metric and Newtonian cosmology. *Phys. Rev. D*, **81**, 103512.

RÄSÄNEN, S. (2010a). Applicability of the linearly perturbed FRW metric and Newtonian cosmology. *Phys. Rev. D*, **81**, 103512.

Räsänen, S. (2010b). Backreaction as an alternative to dark energy and modified gravity. In *Proceedings of the "Beyond the Concordance Model" workshop*, Stellenbosch Institute for Advanced Study, arXiv:1012.0784.

Räsänen, S. (2010c). Light propagation in statistically homogeneous and isotropic universes with general matter content. *JCAP*, **03**, 018.

Räsänen, S. (2011). Backreaction: directions of progress. *Class. Quant. Grav.*, **28**, 164008.

Rees, M.J. & Sciama, D.W. (1968). Large scale Density Inhomogeneities in the Universe. *Nature*, **217**, 511–516.

Reese, E.D., Carlstrom, J.E., Joy, M. *et al.* (2002). Determining the cosmic distance scale from interferometric measurements of the Sunyaev-Zel'dovich effect. *ApJ*, **581**, 53–85.

Reichardt, C.L., Shaw, L., Zahn, O. *et al.* (2012). A Measurement of Secondary Cosmic Microwave Background Anisotropies with Two Years of South Pole Telescope Observations. *ApJ*, **755**, 70.

Reichardt, C.L. *et al.* (2013). Galaxy Clusters Discovered via the SZ Effect in the First 720 Square Degrees of the South Pole Telescope Survey. *ApJ*, **763**, 127.

Reid, B.A. & Spergel, D.N. (2006). Sze signals in cluster models. *ApJ*, **651**, 643.

Rephaeli, Y. (1995). Comptonization of the Cosmic Microwave Background: the Sunyaev-Zeldovich effect. *Ann. Rev. A&A*, **33**, 541–579.

Riess, A.G., Macri, L., Casertano, S. *et al.* (2011). A 3% solution: determination of the Hubble constant with the Hubble space telescope and wide field camera 3. *ApJ*, **730**, 119.

Riess, A.G. *et al.* (1998). Observational evidence from supernovae for an accelerating universe and a cosmological constant. *Astron.J.*, **116**, 1009–1038.

Rigopoulos, G. & Valkenburg, W. (2012). Nonlinear approximation for perturbations in ΛCDM. *Phys. Rev. D*, **86**, 043523.

Rodriguez-Gonzalvez, C., Shimwell, T.W., Davies, M.L. *et al.* (2012). Detailed Sunyaev-Zel'dovich study with AMI of 19 LoCuSS galaxy clusters: masses and temperatures out to the virial radius. *Mon. Not. Roy. Astron. Soc.*, **425**, 162–203.

Romano, A.E. (2007). Lemaître-Tolman-Bondi universes as alternatives to dark energy: Does positive averaged acceleration imply positive cosmic acceleration? *Phys. Rev. D*, **75**, 043509.

Romano, A.E. (2010). Can the cosmological constant be mimicked by smooth large-scale inhomogeneities for more than one observable? *JCAP*, **05**, 020.

Sachs, R.K. (1961). Gravitational waves in general relativity. 6. The outgoing radiation condition. *Proc. Roy. Soc. Lond.*, **A264**, 309–338.

Sachs, R.K. & Wolfe, A.M. (1967). Perturbations of a cosmological model and angular variations of the microwave background. *ApJ*, **147**, 73–90.

SANTOS, M.G., COORAY, A., HAIMAN, Z., KNOX, L. & MA, C.P. (2003). Small-scale CMB Temperature and Polarization Anisotropies due to Patchy Reionization. *ApJ*, **598**, 756.

SARKAR, S. (2008). Is the evidence for dark energy secure? *Gen. Rel. Grav.*, **40**, 269.

SCHÄFER, B.M., PFROMMER, C., HELL, R.M. & BARTELMANN, M. (2006). Detecting Sunyaev-Zel'dovich clusters with Planck- II. Foreground components and optimized filtering schemes. *Mon. Not. Roy. Astron. Soc.*, **370**, 1713–1736.

SCHWARZ, D.J. (2002). Accelerated expansion without dark energy. *ArXiv e-prints*, **astro-ph/0209584**.

SEHGAL, N., KOSOWSKY, A. & HOLDER, G. (2005). Constrained Cluster Parameters from Sunyaev-Zel'dovich Observations. *ApJ*, **635**, 22–34.

SEHGAL, N., TRAC, H., ACQUAVIVA, V. *et al.* (2011). The Atacama Cosmology Telescope: Cosmology from Galaxy Clusters Detected via the Sunyaev-Zel'dovich Effect. *ApJ*, **732**, 44.

SEITZ, S., SCHNEIDER, P. & EHLERS, J. (1994). Light propagation in arbitrary spacetimes and the gravitational lens approximation. *Class. Quant. Grav.*, **11**, 2345–2374.

SELLWOOD, J.A. & KOSOWSKY, A. (2000). Does dark matter exist? *ArXiv*, **astro-ph/0009074**.

SHAO, J., ZHANG, P., LIN, W., JING, Y. & PAN, J. (2011). Kinetic SZ tomography with spectroscopic redshift surveys. *Mon. Not. Roy. Astron. Soc.*, **413**, 628–642.

SHIROKOFF, E., REICHARDT, C.L., SHAW, L. *et al.* (2011). Improved constraints on cosmic microwave background secondary anisotropies from the complete 2008 South Pole Telescope data. *ApJ*, **736**, 61.

SHIROKOV, M.F. & FISHER, I.Z. (1963). Isotropic space with discrete gravitational-field sources. On the theory of a nonhomogeneous isotropic Universe. *Soviet Astronomy*, **6**, 699.

SIEVERS, J.L., HLOZEK, R.A., NOLTA, M.R. *et al.* (2013). The Atacama Cosmology Telescope: Cosmological parameters from three seasons of data. *ArXiv e-prints*, **1301.0824**.

SILK, J. (1977). Large-scale inhomogeneity of the Universe-Spherically symmetric models. *A&A*, **59**, 53.

SINCLAIR, B., DAVIS, T.M. & HAUGBØLLE, T. (2010). Residual Hubble-bubble effects on supernova cosmology. *ApJ*, **718**, 1445.

SONG, Y.S., SABIU, C.G., NICHOL, R.C. & MILLER, C.J. (2010). Statistical Determination of Bulk Flow Motions. *JCAP*, **1001**, 025.

STEBBINS, A. (2007). CMB Spectral Distortions from the Scattering of Temperature Anisotropies. *ArXiv e-prints*, **astro-ph/0703541**.

STEPHANI, H., KRAMER, D., MACCALLUM, M., HOENSELAERS, C. & HERLT, E. (2003). *Exact Solutions of Einstein's Field Equations*. Cambridge University Press.

Stoeger, W.R., Maartens, R. & Ellis, G.F.R. (1995). Proving almost-homogeneity of the universe: an almost EGS theorem. *ApJ*, **443**, 1.

Strauss, M.A. & Willick, J.A. (1995). The Density and peculiar velocity fields of nearby galaxies. *Phys. Rept.*, **261**, 271–431.

Sullivan, M., Guy, J., Conley, A. *et al.* (2011). SNLS3: Constraints on Dark Energy Combining the Supernova Legacy Survey Three Year Data with Other Probes. *ApJ*, **737**, 102.

Sunyaev, R.A. & Zel'dovich, Y.B. (1970). The Interaction of matter and radiation in the hot model of the universe. *Astrophys. Sp. Sci.*, **7**, 20.

Sunyaev, R.A. & Zel'dovich, Y.B. (1980). The velocity of clusters of galaxies relative to the microwave background. The possibility of its measurement. *Mon. Not. Roy. Astron. Soc.*, **190**, 413.

Sussman, R.A. (2010). Evolution of radial profiles in regular Lemaître-Tolman-Bondi dust models. *Class. Quant. Grav.*, **27**, 175001.

Sussman, R.A. (2011). Back-reaction and effective acceleration in generic LTB dust models. *Class. Quant. Grav.*, **28**, 35002.

Szybka, S.J. (2011). Light propagation in Swiss-cheese cosmologies. *Phys. Rev. D*, **84**, 044011.

Tegmark, M. & de Oliveira-Costa, A. (1998). Removing point sources from CMB maps. *ApJ*, **500**, L83–L86.

Tolman, R.C. (1934). Effect of inhomogeneity on cosmological models. *Proc. Nat. Acad. Sci. USA*, **20**, 169, reprinted in *Gen. Rel. Grav.*, 29:935 (1997).

van den Hoogen, R.J. (2011). Averaging Spacetime: Where do we go from here? In T. Damour, R.T. Jantzen & R. Ruffini, eds., *Proceedings of the Twelfth Marcel Grossmann Meeting on General Relativity*, World Scientific, Singapore.

van der Waerden, B.L. (1987). The Heliocentric System in Greek, Persian and Hindu Astronomy. *Annals of the New York Academy of Sciences*, **500**, 525–545.

Vanderlinde, K., Crawford, T.M., de Haan, T. *et al.* (2010). Galaxy Clusters Selected with the Sunyaev-Zel'dovich Effect from 2008 South Pole Telescope Observations. *ApJ*, **722**, 1180–1196.

Vanderveld, R.A., Flanagan, E.E. & Wasserman, I. (2008). Luminosity distance in "Swiss cheese" cosmology with randomized voids. I. Single void size. *Phys. Rev. D*, **78**, 083511.

Visser, M. (2004). Jerk, snap and the cosmological equation of state. *Class. Quant. Grav.*, **21**, 2603.

Vonlanthen, M., Räsänen, S. & Durrer, R. (2010). Model-independent cosmological constraints from the CMB. *JCAP*, **08**, 023.

Wald, R.M. (1984). *General Relativity*. University of Chicago Press.

Wandelt, B.D., Larson, D.L. & Lakshminarayanan, A. (2004). Global, exact cosmic microwave background data analysis using Gibbs sampling. *Phys. Rev. D*, **70**, 083511.

Wang, Y. & Mukherjee, P. (2007). Observational constraints on dark energy and cosmic curvature. *Phys. Rev. D*, **76**, 103533.

Watkins, R. (1997). The RMS peculiar velocity of clusters. *Mon. Not. Roy. Astron. Soc.*, **292**, L59–L63.

Watkins, R., Feldman, H.A. & Hudson, M.J. (2008). Consistently large cosmic flows on scales of $100h^{-1}$ Mpc: a challenge for the standard ΛCDM cosmology. *Mon. Not. Roy. Astron. Soc.*, **392**, 743–756.

Wehus, I.K. & Eriksen, H.K. (2011). A search for concentric circles in the 7-year WMAP temperature sky maps. *ApJ*, **733**, L29.

Weinberg, S. (1976). Apparent luminosities in a locally inhomogeneous universe. *ApJ*, **208**, L1.

Weinberg, S. (1989). The Cosmological Constant Problem. *Rev.Mod.Phys.*, **61**, 1–23.

Weinberg, S. (2008). *Cosmology*. Oxford University Press.

White, M. & Majumdar, S. (2008). Point sources in the context of future SZ surveys. *ApJ*, **602**, 565.

Wiltshire, D.L. (2011). What is dust? – Physical foundations of the averaging problem in cosmology. *Class. Quant. Grav.*, **28**, 164006.

WMAP Collaboration (2013). WMAP Data Products. `http://lambda.gsfc.nasa.gov/product/map/dr4/m_products.cfm`, [Accessed 20-February-2013].

Yoo, C.M., Nakao, K. & Sasaki, M. (2010a). CMB observations in LTB universes: Part I. Matching peak positions in the CMB spectrum. *JCAP*, **07**, 012.

Yoo, C.M., Nakao, K. & Sasaki, M. (2010b). CMB observations in LTB universes. Part II: the kSZ effect in an LTB universe. *JCAP*, **10**, 011.

Zalaletdinov, R.M. (1992). Averaging out the Einstein equations and macroscopic space-time geometry. *Gen. Rel. Grav.*, **24**, 1015–1031.

Zecca, A. (1991). On the Tolman-Bondi model with cosmological term. *Il Nuovo Cimento*, **B106**, 413.

Zhang, P. & Stebbins, A. (2011). Confirmation of the Copernican Principle at Gpc Radial Scale and above from the Kinetic Sunyaev-Zel'dovich Effect Power Spectrum. *Phys. Rev. Lett.*, **107**, 041301.

Zibin, J.P. (2008). Scalar Perturbations on LTB Spacetimes. *Phys. Rev. D*, **78**, 043504.

Zibin, J.P. (2011). Can decaying modes save void models for acceleration? *Phys. Rev. D*, **84**, 123508.

ZIBIN, J.P. & MOSS, A. (2011). Linear kinetic Sunyaev-Zel'dovich effect and void models for acceleration. *Class. Quant. Grav.*, **28**, 164005.

ZIBIN, J.P., MOSS, A. & SCOTT, D. (2008). Can we avoid dark energy? *Phys. Rev. Lett.*, **101**, 251303.

ZUMALACARREGUI, M., GARCÍA-BELLIDO, J. & RUIZ-LAPUENTE, P. (2012). Tension in the Void: Cosmic Rulers Strain Inhomogeneous Cosmologies. *JCAP*, **1210**, 009.